

# Estuarine Circulation in well-mixed tidal inlets

---

Dissertation

zur Erlangung des akademischen Grades

doctor rerum naturalium (Dr. rer. nat.)

der Mathematisch-Naturwissenschaftlichen Fakultät

der Universität Rostock

vorgelegt von

Johannes Becherer

geb. am 11. August 1983 in Rostock

Rostock, 19. Dezember 2013



---

## Abstract

Estuarine dynamics in well-mixed tidal inlets is studied based on data of two measurement campaigns, carried out in the German Wadden Sea. We present the first direct observations of *tidal straining* in the Wadden Sea, a process that is supposed to be a major driver of estuarine circulation in this system. In contradiction to this theory, we also observe strong late flood stratification. This late flood stratification is found to be due to asymmetric lateral circulation, which is generated by a systematic interplay of horizontal density gradients and centrifugal forcing. By applying a consistent theoretical framework this newly discovered process is found to be also responsible for a large fraction of the residual estuarine exchange flow. Finally, an idealized model is developed to study the relevance of this process for other systems.

## Zusammenfassung

Die ästuarine Dynamik von gut durchmischten Gezeitenkanälen wird an Hand der Daten zweier Messkampagnen untersucht, die im deutschen Wattenmeer unternommen wurden. Wir präsentieren die ersten direkten Beobachtungen von *tidal straining* im Wattenmeer, einem Prozess von dem man vermutet, dass er hauptverantwortlich für die ästuarine Zirkulation in diesem System ist. Im Widerspruch zu dieser Theorie stehend, beobachten wir allerdings auch starke Flutschichtung. Diese Flutschichtung wird durch asymmetrische Lateralzirkulation hervorgerufen, die wiederum durch ein systematisches Zusammenspiel von horizontalem Dichtegradient und Zentrifugalkraft verursacht wird. Durch den Gebrauch eines konsistenten theoretischen Modells wird gezeigt, dass dieser neu entdeckte Prozess ebenfalls für einen Großteil der residualen ästuarinen Austauschströmung verantwortlich ist. Abschließend wird ein idealisiertes Modell entwickelt, um die Relevanz dieses Mechanismus für andere Systeme zu untersuchen.



# Contents

<b>1. Structure of this thesis</b>	<b>1</b>
<b>2. Basic equations</b>	<b>3</b>
2.1. Momentum equations . . . . .	3
2.2. Density equations . . . . .	3
2.3. Turbulence in the boundary layer . . . . .	4
2.3.1. Law-of-the-wall . . . . .	4
2.3.2. Turbulent fluxes . . . . .	4
<b>3. Introduction: Circulating Estuaries</b>	<b>7</b>
3.1. What is estuarine circulation? . . . . .	7
3.2. Why is estuarine circulation important? . . . . .	9
3.3. How does estuarine circulation work? . . . . .	10
3.3.1. Direct drivers of estuarine circulation . . . . .	10
3.3.2. Indirect drivers of estuarine circulation . . . . .	11
<b>4. Sylt inlet: Tidal straining and flood tide stratification</b>	<b>19</b>
4.1. Introduction . . . . .	19
4.2. Field observations . . . . .	20
4.2.1. Study site . . . . .	20
4.2.2. Instrumentation and data analysis . . . . .	20
4.2.3. Field work . . . . .	22
4.3. Results . . . . .	24
4.4. Discussion and conclusions . . . . .	26
<b>5. Spiekeroog inlet: Asymmetric lateral circulation</b>	<b>29</b>
5.1. Introduction . . . . .	29
5.2. Field campaign . . . . .	31
5.2.1. Study site . . . . .	31
5.2.2. Instrumentation . . . . .	31
5.2.3. Measurements . . . . .	33
5.2.4. Basic data-processing . . . . .	33
5.3. Theoretical framework . . . . .	35
5.3.1. Potential energy anomaly $\Phi$ . . . . .	35
5.3.2. Framework for along- and across-channel circulation . . . . .	37
5.4. Observations . . . . .	41
5.4.1. General conditions . . . . .	41
5.4.2. Tidal variation of stratification . . . . .	41

5.4.3. Tidal velocities . . . . .	45
5.5. Mechanisms (Discussion) . . . . .	48
5.5.1. Generation of vertical stratification . . . . .	48
5.5.2. Generation of lateral circulation . . . . .	52
5.5.3. Implications for estuarine circulation . . . . .	56
5.6. Conclusions . . . . .	59
<b>6. Vorticity-Model: Jump and circulate</b>	<b>61</b>
6.1. Introduction . . . . .	61
6.2. Model description . . . . .	61
6.2.1. Model assumptions . . . . .	62
6.2.2. Vertical gradients . . . . .	63
6.2.3. Lateral gradients . . . . .	64
6.2.4. Turbulence closure . . . . .	65
6.2.5. Model parameters . . . . .	66
6.2.6. Non-dimensional numbers . . . . .	67
6.3. Model Validation . . . . .	69
6.3.1. Model setup . . . . .	69
6.3.2. Results . . . . .	70
6.3.3. Discussion . . . . .	74
6.4. Influence of channel shapes . . . . .	76
6.4.1. Model setups . . . . .	76
6.4.2. Results . . . . .	76
6.4.3. Discussion . . . . .	81
6.5. Parameter study . . . . .	84
6.5.1. Model setup . . . . .	84
6.5.2. Results . . . . .	85
6.5.3. Discussion . . . . .	89
6.6. Conclusions . . . . .	95
<b>7. Summary and Conclusions</b>	<b>97</b>
<b>8. Future perspectives</b>	<b>99</b>
<b>A. Vorticity-Model</b>	<b>101</b>
A.1. Basic relations . . . . .	101
A.1.1. Along-channel vorticity . . . . .	101
A.1.2. Across-channel vorticity . . . . .	101
A.1.3. Continuity equation . . . . .	102
A.2. Derivation of model equations . . . . .	102
A.2.1. $[\omega_x]$ . . . . .	102
A.2.2. $[\omega_y]$ . . . . .	103
A.2.3. $[N^2]$ . . . . .	103
A.2.4. $[\partial_y b]$ . . . . .	103
A.2.5. $[\partial_y u]$ . . . . .	104
A.3. $[\Phi]$ . . . . .	105

A.4. Turbulence closure . . . . . 106  
A.5. Periodicity of a signal . . . . . 106





# 1. Structure of this thesis

The studies for this thesis have been carried out in the framework of the ECOWS<sup>1</sup> project of the German Research Foundation (DFG). The major aim of this thesis is to study estuarine circulation in a highly energetic tidal environment with small horizontal density gradients. Examples for such environments are for instance the tidal inlets of the German Wadden Sea, where two measurement campaigns have been conducted.

The results of the first campaign carried out in the *Lister Deep* have been published in Becherer et al. (2011). Chapter 4 is based on that publication and studies indications for mixing asymmetries like tidal straining and their implication for vertical stratification and sediment transport.

A second substantially refined measurement campaign was carried out in the tidal inlet between the islands of *Langeoog* and *Spiekeroog*, a similar study site as *Lister Deep*. The obtained data set is more comprehensive in terms of instrumentation and data coverage than the first campaign and provides a whole new perspective on the estuarine dynamics in the Wadden Sea. The analysis of those results are the core of another publication (Becherer et al., submitted), which is the basis of chapter 5. In this chapter we identify a whole new mechanism that is able to explain a large fraction of the estuarine dynamics in the tidal inlet.

In order to test the general relevance of the newly discovered process for other systems and to connect the findings of chapter 4 and chapter 5, we provide an idealized modelling study in chapter 6. Despite its simplicity, the self-developed vorticity model is able to capture most of the dynamics that appear in the observations and allows at the same time projections of the investigated processes on other systems. Chapter 6 is written in such a way that it can be used with small modification as a third independent article, which will be submitted to a peer-review journal in the near future.

Chapter 4, 5, and 6, which are the core of this thesis, are in the form of independent manuscripts, which is why each of them have their own introduction and conclusion. Nevertheless, all three chapters are strongly related to each other, and are surrounded by a thematic introduction in chapter 3 and final conclusions in chapter 7. This thesis closes with some future perspectives in chapter 8.

As mentioned above, parts of this thesis have already been published in two articles:

- Becherer, J., H. Burchard, G. Flöser, V. Mohrholz, and L. Umlauf, 2011: Evidence of tidal straining in well-mixed channel flow from micro-structure observations. *Geophys. Res. Lett.*, **38**
- Becherer, J., M. T. Stacey, L. Umlauf, and H. Burchard, submitted: Asymmetric lateral circulation in a well-mixed tidal inlet: Mechanisms and implications. *J. Phys.*

---

<sup>1</sup>Exploring the role of estuarine circulation for transport of suspended particulate matter (SPM) in the Wadden Sea by means of field observations and numerical modelling

*Oceanogr.*

These articles would not have been possible in this form without the help of the co-authors, whose contributions are listed below :

**Hans Burchard** Leibniz-Institute for Baltic Sea Research, Warnemünde, Germany, department of Physical Oceanography. Principal investigator of the ECOWS project. Support and supervision of this thesis and of the publications.

**Lars Umlauf** Leibniz-Institute for Baltic Sea Research, Warnemünde, Germany, department of Physical Oceanography. Support of data analysis, measurements and manuscript revision.

**Mark T. Stacey** Civil and Environmental Engineering Department, University of California, Berkeley, California, USA. Support of data analysis, theoretical framework, article concept and manuscript revision.

**Volker Mohrholz** Leibniz-Institute for Baltic Sea Research, Warnemünde, Germany, department of Physical Oceanography. Support of data analysis and measurements.

**Götz Flöser** Institute for Coastal Research, Helmholtz Centre Geesthacht, Geesthacht, Germany. Support of data analysis and measurements.

## 2. Basic equations

In this chapter we present the most important equations used throughout the entire thesis. More specific equations related to the different topics will be introduced in the corresponding chapters.

### 2.1. Momentum equations

The basis of almost any geophysical flow analysis are the the Reynolds averaged Navier Stokes (RANS) equations. Applying the Boussinesq and hydrostatic assumptions, the two horizontal components in a curved coordinate system are (Huijts et al., 2009)

$$\begin{aligned} \partial_t u &= -u\partial_x u - v\partial_y u - w\partial_z u + fv - \frac{1}{R}uv \\ &\quad -g\partial_x \eta + \int_z^\eta \partial_x b dz' - \partial_z \langle u'w' \rangle , \end{aligned} \quad (2.1)$$

$$\begin{aligned} \partial_t v &= -u\partial_x v - v\partial_y v - w\partial_z v - fu + \frac{1}{R}v^2 \\ &\quad -g\partial_y \eta + \int_z^\eta \partial_y b dz' - \partial_z \langle v'w' \rangle , \end{aligned} \quad (2.2)$$

where here and after  $\partial_t$ ,  $\partial_x$ ,  $\partial_y$ , and  $\partial_z$  denote partial derivative with respect to time and space,  $R$  is the radius of curvature,  $f$  the Coriolis parameter,  $\eta$  the surface elevation, and  $b$  the buoyancy. The underlying coordinate system is aligned with the curved channel, where  $y$  is parallel and  $x$  perpendicular to the radius of curvature, and  $z$  points vertically upwards. Correspondingly,  $u$  and  $v$  are the horizontal and  $w$  the vertical velocity components.  $\langle \cdot \rangle$  denotes a Reynolds average.<sup>1</sup>  $u'$ ,  $v'$  and  $w'$  label velocity fluctuations, which are defined as deviations from the Reynolds average. Note that all other quantities not associated with a prime are Reynolds averaged quantities.

For incompressible fluids the velocity components are related via the continuity equation,

$$\partial_x u + \partial_y v + \partial_z w = 0 . \quad (2.3)$$

### 2.2. Density equations

In this thesis we are only interested in the dynamical impact of density. Therefore, we introduce the buoyancy,

$$b = -g \frac{\rho - \rho_0}{\rho_0} \quad (2.4)$$

---

<sup>1</sup>Mathematically a Reynolds average corresponds to an ensemble average, but in most situations it is approximated by a temporal or spatial average.

which corresponds to a normalized acceleration associated with density differences. In (2.4)  $g$  denotes gravity acceleration,  $\rho$  the density, and  $\rho_0 = 1000 \text{ kg m}^{-3}$  an arbitrary reference density.

The transport equation for the buoyancy reads as

$$\partial_t b = -u\partial_x b - v\partial_y b - w\partial_z b - \partial_z \langle b'w' \rangle, \quad (2.5)$$

where  $b'$  denotes the deviation of the buoyancy from the Reynolds average.

Vertical stratification can be measured in terms of the buoyancy frequency,

$$N^2 = \partial_z b. \quad (2.6)$$

A way to quantify vertical stratification from an energetic point of view was first introduced by Simpson (1981), who defined the potential energy anomaly as *the work per unit volume required to bring about vertical redistribution of mass in complete mixing*,

$$\Phi = \frac{g}{D} \int_{-H}^{\eta} (\langle \rho \rangle_z - \rho) z \, dz = \frac{\rho_0}{D} \int_{-H}^{\eta} (b - \langle b \rangle_z) z \, dz, \quad (2.7)$$

where  $H$  is the average and  $D = \eta + H$  the total water depth.  $\langle \cdot \rangle_z$  denotes here and after a depth average.

## 2.3. Turbulence in the boundary layer

### 2.3.1. Law-of-the-wall

In the well-mixed bottom region the velocity is sheared towards the bottom, often describing a characteristic logarithmic profile,

$$u(z) = \frac{u_*}{\kappa} \ln \left( \frac{z + H + z_0}{z_0} \right), \quad (2.8)$$

where  $u_*$  is the bottom friction velocity,  $\kappa = 0.41$  the von Karman-constant, and  $z_0$  the roughness length. Taking the derivative of (2.8) with respect to  $z$  yields an expression for the vertical shear,

$$\frac{\partial}{\partial z} u(z) = \frac{u_*}{\kappa} \frac{1}{z + H + z_0}. \quad (2.9)$$

### 2.3.2. Turbulent fluxes

It is a useful approach to model the turbulent fluxes appearing in (2.1), (2.2), and (2.5) with a down-gradient assumption (Umlauf and Burchard, 2005),

$$\langle u'w' \rangle = -\nu_t \partial_z u, \quad (2.10)$$

$$\langle v'w' \rangle = -\nu_t \partial_z v, \quad (2.11)$$

$$\langle w'b' \rangle = -\nu_t^b N^2, \quad (2.12)$$

where we have used (2.6).  $\nu_t$  and  $\nu_t^b$  denote the turbulent viscosity and diffusivity, respectively, which are related to each other by the turbulent Prandtl number,

$$\text{Pr}_t = \frac{\nu_t^b}{\nu_t} . \quad (2.13)$$

An easy way to model the turbulent viscosity is to express it as a product of a turbulent velocity scale,  $U_T$ , and a turbulent length scale,  $L_T$ , yielding

$$\nu_t(z) = U_T L_T . \quad (2.14)$$

In the near bottom region the size of eddies is limited by the distance to the bed, providing a turbulent length scale of  $L_T = \kappa(z + H + z_0)$ , and  $u_*$  as a typical turbulent velocity scale, which yields

$$\nu_t(z) = u_* \kappa(z + H + z_0) . \quad (2.15)$$

Combining (2.9), (2.10), and (2.15) leads to an expression for the bottom stress,

$$\langle u'w' \rangle \Big|_{z=-H} = -\nu_t \partial_z u \Big|_{z=-H} = -u_*^2 . \quad (2.16)$$

Making use of (2.16) the shear production of turbulent kinetic energy close to the bottom can be written as

$$P = -\langle u'w' \rangle \partial_z u = \frac{u_*^3}{\kappa(z + H + z_0)} . \quad (2.17)$$

If we further consider a equilibrium between shear production and dissipation of turbulent kinetic energy,  $P = \varepsilon$ , we obtain a relation between the friction velocity and the dissipation of turbulent kinetic energy,

$$u_* = [\kappa \varepsilon (z + H + z_0)]^{\frac{1}{3}} , \quad (2.18)$$

which we are going to use in order to estimate the friction velocity based on turbulence measurements.



### 3. Introduction: Circulating Estuaries

Since the major subject of this thesis is estuarine circulation, we begin with some conceptual ideas about estuarine circulation in general. The first question that arises is: *what exactly is estuarine circulation?* Since the term estuarine circulation is not precisely defined and often differently used in different publications, we start with a general concept of how estuarine circulation can be understood in the context of this thesis. Afterwards, we briefly mention *why estuarine circulation is important?*, in order to motivate our investigations in a larger context. Finally, we will give some overview over the known mechanisms that can drive estuarine circulation, by making an attempt to answer the question *how does estuarine circulation work?*

#### 3.1. What is estuarine circulation?

Traditionally, estuaries are defined as the transition zone between the fresh water of a river and the salty water of the open sea. Thus the river run-off of fresh water provides a longitudinal (along-channel) density gradient. In a wider sense it is possible to think of all kind of semi-enclosed water bodies with horizontal density gradients as estuaries. Such a system could be for instance the Wadden Sea, which is the major study-site of this thesis, where the horizontal density gradients are less generated by river run-off, but rather by differential rain-fall and heating.<sup>1</sup>

<sup>1</sup>Differential heating denotes a mechanism, where the meteorological heat-flux leads for shallower waters to higher temperature than for deeper waters, simply due to the fact that the water volume, which is effected by the surface heat flux is smaller. Differential rain-fall is a similar effect, where the rain-fall over a shallow area yields a stronger freshening than over deeper waters.

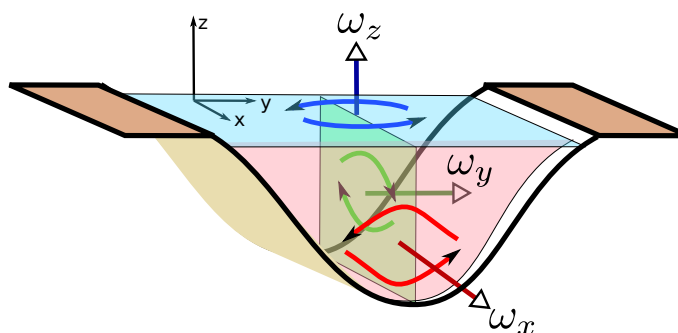


Figure 3.1.: Sketch of the three vorticity components in a tidal channel. The channel is aligned with the  $x$ -axis, thus  $\omega_x$  corresponds to lateral,  $\omega_y$  to longitudinal, and  $\omega_z$  to horizontal circulation.

Often found in association with the typical horizontal density or buoyancy gradient<sup>2</sup>, is a characteristic residual exchange flow in longitudinal (along-estuary) direction, with a net in-flow into the estuary close to the bottom and an out-flow close to the surface.<sup>3</sup> This exchange flow is often referred to as estuarine circulation.

When studying an estuarine channel it seems straight forward to distinguish three different directions of circulation, corresponding to the three different vorticity components (see figure 3.1),

$$\begin{aligned}\omega_x &= \partial_y w - \partial_z v, \\ \omega_y &= \partial_z u - \partial_x w, \\ \omega_z &= \partial_x v - \partial_y u,\end{aligned}\tag{3.1}$$

where  $\partial_x$ ,  $\partial_y$ , and  $\partial_z$  denote partial derivatives with respect to  $x$ ,  $y$ , and  $z$ , respectively. If we consider  $\partial_y w \ll \partial_z v$  (Collignon and Stacey, 2012) and further assume that the estuary is homogenous in  $x$  we obtain,

$$\begin{aligned}\omega_x &= -\partial_z v, \\ \omega_y &= \partial_z u, \\ \omega_z &= -\partial_y u.\end{aligned}\tag{3.2}$$

$\omega_x$  can be understood as lateral circulation<sup>4</sup>,  $\omega_y$  corresponds to longitudinal circulation, and  $\omega_z$  to horizontal circulation. In this context the classical residual estuarine exchange flow corresponds to the tidal mean of the  $y$ -component of the vorticity,  $\langle \omega_y \rangle_{M_2}$ , or in other words the average of the vertical shear of the along-channel velocity component.

Based on the momentum equations (2.1) and (2.2) we can derive transport equations for the different vorticity components (3.2). We obtain for the lateral circulation

$$\begin{aligned}\partial_t \omega_x &= -\omega_x \partial_y v - v \partial_y \omega_x - \omega_x \partial_z w - w \partial_z \omega_x + f \omega_y \\ &\quad - \frac{2}{R} u \omega_y + \partial_y b + \partial_z (\partial_z \langle v'w' \rangle)\end{aligned},\tag{3.3}$$

for the longitudinal circulation

$$\begin{aligned}\partial_t \omega_y &= -\omega_x \omega_z - v \partial_y \omega_y - \omega_y \partial_z w - w \partial_z \omega_y - f \omega_x \\ &\quad - \frac{1}{R} (v \omega_y - u \omega_x) - \partial_x b - \partial_z (\partial_z \langle u'w' \rangle)\end{aligned},\tag{3.4}$$

and for the horizontal circulation

$$\begin{aligned}\partial_t \omega_z &= -\omega_z \partial_y v - v \partial_y \omega_z + \omega_y \partial_y w + w \partial_y \omega_y - f \partial_y v \\ &\quad - \frac{1}{R} (v \omega_z - u \partial_y v) - \partial_y \int_z^\eta \partial_x b \, dz' + \partial_y (\partial_z \langle u'w' \rangle)\end{aligned},\tag{3.5}$$

---

<sup>2</sup>The buoyancy,  $b$ , accounts for the dynamical influence of the density (see equation (2.4)). Thus buoyancy-gradients can be thought as inverse density gradients.

<sup>3</sup>The term *residual exchange flow* denotes here and after a tidally averaged velocity profile. Sometimes we also talk about *net exchange flow* or *estuarine exchange flow*. All these terms are used as synonyms.

<sup>4</sup>There are a number of synonyms for lateral circulation used in the literature and partly also in this thesis, like for instance stream-normal circulation, secondary circulation, transverse circulation and along-channel vorticity.



where for consistency we ignored the along-channel advection term.<sup>5</sup>

Early studies dealing with estuarine circulation (Pritchard, 1952, 1954, 1956; Hansen and Rattray, 1965) mainly focused on longitudinal circulation, generated by a balance of the longitudinal baroclinic pressure gradient and vertical mixing. More recently, people start to look beyond the classical one-dimensional picture of estuaries and begin to concentrate also on the other circulation components. It is found that horizontal circulation ( $\omega_z$ ) plays an important role in the generation of residual currents especially in wide estuaries, suggesting that rather the horizontal than the vertical variation of the longitudinal velocity component determines the estuarine exchange (Fischer, 1972; Valle-Levinson et al., 2000, 2003). Nunes and Simpson (1985) emphasized the importance of lateral circulation ( $\omega_x$ ) for estuarine dynamics, recently followed by a number of studies that pointed out the relation between lateral circulation and longitudinal estuarine exchange flow (Lacy et al., 2003; Lerczak and Geyer, 2004; Scully et al., 2009; Burchard et al., 2011).

Valle-Levinson et al. (2003) used an equation for  $\omega_z$  in order to analyze the horizontal circulation in Chesapeake Bay. In Analogy to that Collignon and Stacey (2012) analyzed a transport equation for  $\omega_x$  to study lateral circulation, but to our knowledge the association of longitudinal circulation with the across-channel vorticity component,  $\omega_y$ , has not been extensively used in the analysis of estuarine circulation so far. Since all three vorticity components strongly interact with each other and thus determine the estuarine exchange flow, we focus on a vorticity analysis in this study and use it to construct a framework containing all three vorticity components, and thus associating lateral, horizontal and longitudinal circulation to each other in a consistent way.

## 3.2. Why is estuarine circulation important?

Nowadays, every physical investigation needs to be motivated by its economical, sociological, or at least biological relevance. Therefore, we use this section to briefly address the question: *Why is estuarine circulation important?*

Besides the horizontal dispersion of salt, nutrients, pollutants, and biological films, a major motivation for studying estuarine circulation is its impact on sediment transport and trapping. Burchard and Baumert (1998) for instance studied the role of estuarine circulation in the generation of a so-called estuarine turbidity maximum (ETM), which is a zone of high sediment concentration at the upper end of the horizontal density gradient. The fact that the classical estuarine exchange flow is directed into the estuary at the bottom, where we usually find the largest sediment concentration, explains its importance in terms of sediment transport. Burchard et al. (2008) suggested based on a modeling study that estuarine circulation is a major driver of suspended sediment into the Wadden Sea, which is our focal area.

Since many estuaries contain important economical infrastructure like harbours or shipping routes, which have to be maintained by expensive sediment dredging, understanding the underlying mechanisms that accumulate sediment in those areas is of large economical interest.

---

<sup>5</sup>We already assumed for (3.2) vanishing along-channel derivatives, with the exception of the along-channel buoyancy gradient,  $\partial_x b$ .

### 3.3. How does estuarine circulation work?

Traditionally, along-channel estuarine circulation is believed to be generated by an along-channel baroclinic pressure gradient, which is in balance with vertical mixing, this process is referred to as gravitational exchange flow (Pritchard, 1952, 1954, 1956; Hansen and Rattray, 1965). Since then a large number of different processes have been discovered that are as well contributing to the residual estuarine exchange flow, with tidally averaged velocities close to the bottom that are directed up-estuary and in the opposite direction at the surface. Fifty years of estuarine research since Hansen and Rattray (1965), discovered a whole zoo of different drivers for residual estuarine circulation. In this section we make the attempt to give an overview over all those processes that are potentially relevant for weakly stratified estuaries.

Different authors often use different terms for the same or at least similar processes, which can easily yield confusion. Here we try to use a consistent terminology to explain the underlying mechanisms in order to allow the reader to follow the argumentation of the upcoming chapters.

Generally, one could classify the different drivers of estuarine circulation<sup>6</sup> into two major categories, direct (permanent) and indirect (secondary) drivers for estuarine circulation. Direct drivers are forces that basically act the entire tidal cycle in the same direction, like the longitudinal buoyancy gradient for instance, and furthermore directly contribute to the vorticity balance (3.4). An indirect or secondary driver on the other hand, denotes a mechanism that is able to break the symmetry<sup>7</sup> of an otherwise symmetric term of the vorticity balance (3.4). Such a process would be for instance classical tidal straining, which causes an asymmetry in the friction term of the vorticity balance (last term of equation(3.4)). In principle all processes generating residual estuarine circulation need to be tidally asymmetric, like for instance the along-channel buoyancy gradient, which is pointing in the same direction at flood as at ebb tide, thus being asymmetric in our definition. Therefore, the major criterion to distinguish direct from indirect mechanisms is if they are directly represented in the across-channel vorticity balance (3.4) or just modulating one or several of its terms.

#### 3.3.1. Direct drivers of estuarine circulation

As mentioned above the classical mechanism made responsible for estuarine circulation is gravitational circulation (Hansen and Rattray, 1965; MacCready and Geyer, 2010; Geyer and MacCready, 2013). The along-channel buoyancy gradient,  $\partial_x b$ , causes a baroclinic pressure gradient, which generates estuarine circulation (residual along-channel estuarine exchange flow). In well-mixed estuaries, the effect of  $\partial_x b$  on the across-channel vorticity,  $\omega_y$ , is compensated by vertical mixing most of the tidal cycle, only around slack tide mixing is small enough in order to allow for a substantial gravitational exchange. However,

---

<sup>6</sup>Without additional prefixes *estuarine circulation* denotes here and after the longitudinal residual exchange flow, which we identify with the tidal mean of the across-channel vorticity,  $\langle \omega_y \rangle_{M_2}$ .

<sup>7</sup>In the context of this study symmetry denotes a symmetrical behavior of certain terms between and ebb and flood. This means that a term, which is changing sign within a tidal cycle is symmetric, if it has a vanishing temporal mean. Thus tidal asymmetries in our sense are always associated with a net-effect, meaning a tidal average different from zero.

gravitational circulation belongs to the direct drivers, since the forcing agent  $\partial_x b$  directly contributes to the  $\omega_y$ -balance (3.4) and is pointing in the same direction with more or less the same strength the entire tidal cycle.

Another important direct driver of net estuarine exchange flow in many estuaries is the river run-off itself. The barotropic pressure gradient generated by the in up-estuary direction increasing surface elevation, drives the run-off, which is sheared towards the bottom due to friction of the bed. From (3.2) we know that the major contribution for the across-channel vorticity comes from the vertical shear of the along-channel velocity, thus the vertically sheared river run-off provides a direct (permanent) contribution to  $\langle \omega_y \rangle_{M_2}$  and thus to estuarine circulation.

A third possible direct driver can be wind-forcing or in other words surface momentum flux. The wind provides a source of surface currents that in association with a compensating barotropic pressure gradient drive a vertical exchange flow (Hansen and Rattray, 1965). Since this force is tide-independent we call wind-forcing a direct driver for estuarine exchange flow. In contrast to the other direct drivers of estuarine circulation, wind forcing does not necessarily contribute to estuarine circulation in a positive (classical) sense. Depending on the wind direction it could also yield a compensation of the classical residual exchange flow.

Both river run-off and wind forcing appear in the vorticity balance (3.4) as additional contributions of the friction term, river run-off as additional residual bottom friction and wind forcing as a surface momentum flux.

### 3.3.2. Indirect drivers of estuarine circulation

There are a large number of indirect drivers for residual along-channel exchange flow. This is due to the fact that one could make up all kind of secondary or even high order processes occurring under certain circumstances that are principally able to drive estuarine circulation. Here we would like to concentrate on two major categories of indirect drivers, mixing asymmetries and momentum rectification due to lateral circulation.

#### Mixing Asymmetry: Tidal Straining

Jay and Musiak (1994) pointed out that mixing asymmetries can yield residual estuarine exchange flow. A difference in vertical momentum flux between ebb and flood leads to a difference in the average vertical distribution of along-channel momentum between ebb and flood, respectively. Enhanced turbulent momentum flux during flood for instance, yields an average velocity profile that is more homogeneous in the vertical, which in association with a vertically more sheared ebb-profile, due to reduced turbulent momentum flux, causes a residual longitudinal exchange flow (see left column figure 3.2). This configuration of enhanced vertical mixing during flood and reduced vertical mixing during ebb leads to estuarine circulation with the same orientation as classical gravitational circulation.

Based on the reason of the asymmetric vertical momentum flux, tidal mixing asymmetries can be separated into two major subcategories, external and internal mixing asymmetries. As external tidal mixing asymmetries, we denote those processes, which cause a tidally asymmetric generation of turbulence. In contrast, internal mixing asymmetries

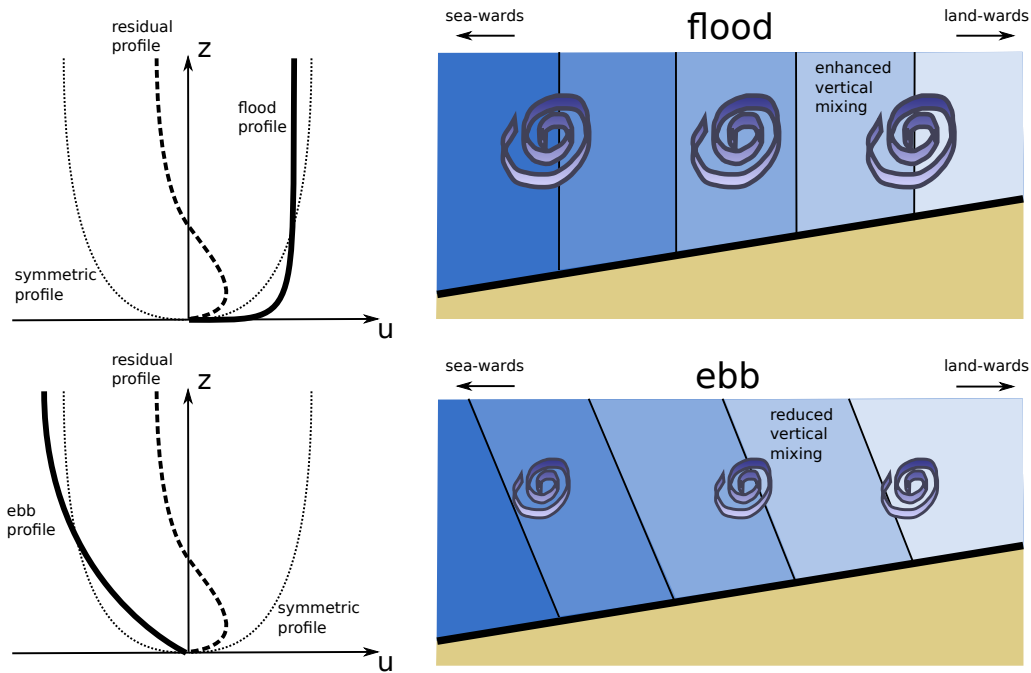


Figure 3.2.: Sketch of tidal straining. The upper row represents flood tide and the lower row ebb tide, respectively. The velocity profiles at the left-hand-side correspond to the longitudinal (along-channel) velocity, where the thick solid line illustrates the effective flood and ebb current profile respectively. The dotted lines illustrates velocity profiles corresponding to a perfectly symmetric tide, and the dashed lines show the residual (tidal mean) velocity (this part of the sketch is inspired by Jay and Musiak (1994)). The right-hand-side illustrates the corresponding longitudinal cross-section of the estuary, with the sea to the left and the river-source to the right (this part of the sketch is inspired by Simpson et al. (1990)). The colored contours represent different densities, where dark blue is denser than light blue. The spirals are supposed to illustrate vertical turbulent mixing, where larger spiral correspond to enhanced mixing and vice versa.

are usually associated with vertical stratification and its inhibiting effect on the vertical momentum flux.

In well-mixed estuaries a major fraction of turbulence is generated by tidal currents that are vertically sheared due to bottom friction. It is a well-known phenomenon that periodic tides from the open Sea interact with geometrical features of estuaries (or tidal basins), generating higher harmonics, so called over-tides. For the  $M_2$ -tide for instance the most important over-tide is the  $M_4$ -tide. The amplitude-ratio as well as the phase shift between the different tidal components can cause an asymmetry in the strength of the tidal currents (e.g. Aubrey and Speer (1985); Speer and Aubrey (1985); Friedrichs and Aubrey (1988)). The asymmetric magnitude of ebb and flood currents leads to an asymmetric turbulence production, which can ultimately yield a residual exchange flow. The direction of this residual force is depending on the relation of the certain tidal components within a particular estuary. Thus it is not necessary that this process contributes in a positive sense to the classical estuarine exchange flow.

Another important category of estuarine circulation drivers are the internal mixing asymmetries (Jay and Musiak, 1994). Any process, generating asymmetric vertical stratification within an estuary, falls in this category, since vertical stratification is known to limit the turbulent mixing length scale and thus inhibits the vertical momentum flux (see e.g. Umlauf and Burchard (2005)). One of the most prominent of these processes is tidal straining or strain induced periodic stratification (SIPS) (Simpson et al., 1990).

First van Aken (1986) and then Simpson et al. (1990) described a process that systematically generates an asymmetry of stratification between ebb and flood. Due to bottom friction the tidal currents are sheared towards the bottom, which yields differential advection of the horizontal buoyancy gradient (see figure 3.2). During flood the denser water from the open sea is transported faster at the surface, yielding reduced or even unstable vertical stratification (see upper right panel figure 3.2). The ebb-currents on the other hand advect the less dens water from inside the estuary faster at the surface, which yields the opposite situation with enhanced vertical stratification during ebb (see lower right panel figure 3.2). As a result of this process, we find enhanced vertical stratification during ebb and reduced or even unstable stratification during flood, which is why the process is referred to as strain induced periodic stratification (SIPS).<sup>8</sup>

Jay and Musiak (1994) pointed out that this systematic stratification asymmetry yields an asymmetry in the vertical profile of the along-channel tidal currents. The enhanced vertical stratification during ebb suppresses vertical flux of momentum, which leads to a rather strongly sheared vertical profile of the stream-wise velocity (see lower left panel figure 3.2). During flood on the other hand, stratification is weak or even inverse, which allows for a strong vertical momentum exchange, yielding a fairly homogeneous flood profile of the along-channel velocity (see upper left panel figure 3.2). As a net (tidally averaged) profile we obtain a distribution that appears similar like a residual profile associated with classical gravitational exchange, directed inside the estuary at the bottom and outside at

---

<sup>8</sup>A similar process, called shear induced convection (ShIC), is observed in the bottom boundary layer of stratified basins, where differential advection due to internal seiches generate asymmetric stratification (Becherer and Umlauf, 2011; Lorrai et al., 2011). Here the asymmetry is not between ebb and flood tides, but between periods of up- and down-welling of a particular seiche (standing internal wave), yielding like tidal straining to an asymmetrical mixing situation.

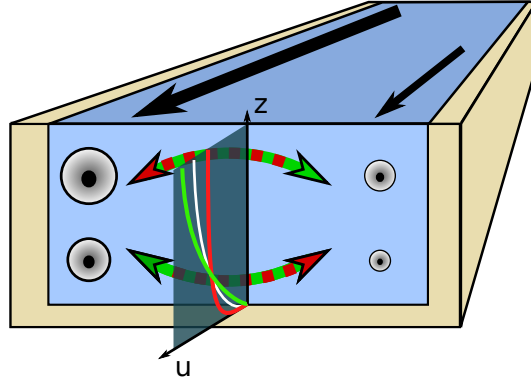


Figure 3.3.: Lateral momentum rectification. The laterally sheared along-channel momentum is redistributed by lateral circulation, which leads depending on the orientation of the lateral circulation to an increase (green) or a decrease (red) of vertical shear of the stream wise velocity. The white circles symbolize the stream-wise velocity, where the size of the circle indicates its strength. The white line at the graph in the middle of the sketch shows an undisturbed vertical profile of the along-channel velocity. Depending on the relative sense of lateral rectification this profile is modified to less or more vertical shear, illustrated by the red and green lines, respectively.

the surface(see dashed line left panels figure 3.2). Following Burchard and Hetland (2010) we call this particular driver of estuarine circulation *tidal straining circulation*.

Based on observations (Geyer et al., 2000; Stacey et al., 2001) and idealized models (Burchard and Baumert, 1998; Stacey et al., 2008; Burchard and Hetland, 2010; Burchard et al., 2011), several studies showed that the effect of tidal straining might be of great importance, often even more important than classical gravitational circulation in terms of generating residual estuarine exchange flow.

### Lateral circulation

Another important secondary driver of estuarine circulation is lateral circulation. There are basically three ways in which lateral circulation can generate longitudinal circulation. The first way is the direct transformation of  $\omega_x$  in  $\omega_y$  via Coriolis deflection and the second way is curvature deflection (5<sup>th</sup> and 6<sup>th</sup> term of (3.4)). Usually more important than these two mechanisms is the redistribution of along-channel momentum due to lateral circulation, a processes at which  $\omega_z$  is transformed into  $\omega_y$  by lateral circulation,  $\omega_x$  (1<sup>st</sup> term of (3.4)).

Figure 3.3 illustrates a sketch of the latter mechanism. A major condition for the occurrence of the effect is a lateral shear in the along-channel momentum,  $\partial_y u$ , which correspond according to (3.2) to the vertical vorticity component,  $\omega_z$ . If there is in addition substantial lateral circulation,  $\omega_x$ , the along-channel momentum,  $u$ , will be redistributed in such a way that its vertical profile changes.

In well mixed estuaries, where the bottom boundary layer principally effects the entire water column, we can approximate the along-channel velocity by a characteristic logarithmic profile, which is determined by the strength of the tidal currents and a particular

bottom drag-coefficient (see equation 2.8). Such an idealized profile is illustrated by the white line in figure 3.3. Due to the transformation of lateral into vertical shear this profile changes. Depending on the relative orientation of  $\omega_z$  and  $\omega_x$  we obtain an increase or a decrease of  $\omega_y$ , which can be identify with the vertical shear of the along-channel momentum (see equation (3.2)). If  $\omega_z$  and  $\omega_x$  have the same orientation they tend to decrease  $\omega_y$ , corresponding to a positive contribution to classical estuarine circulation, which we identify with a negative residual of the along-channel circulation,  $\langle \omega_y \rangle_{M_2}$ . On the other hand, for opposing signs of  $\omega_z$  and  $\omega_x$ , we expect a negative contribution to estuarine circulation. Similar as for the tidal straining circulation a positive contribution to classical estuarine circulation corresponds to a vertically more homogeneous flood profile and a in terms of shear increased ebb-profile.<sup>9</sup>

This process is referred to as momentum rectification (e.g. Huijts et al. (2009); Scully et al. (2009))) and got lots of attention in the literature published during the last decade. Lacy et al. (2003) found that lateral circulation has a large influence on the along-channel momentum balance. Based on an idealized modelling study Lerczak and Geyer (2004) emphasized the overall importance of this process. They found it to often generate more residual exchange flow than classical gravitational circulation. Furthermore, Lerczak and Geyer (2004) pointed out the phenomenological analogy of lateral momentum rectification to the mixing asymmetries associated with the tidal straining circulation described by Jay and Musiak (1994), where the vertical profile of the along-channel velocity is more homogeneous during flood and stronger sheared during ebb. Nevertheless, Lerczak and Geyer (2004) did not include the effect of mixing asymmetries in their model, since they assumed a constant eddy viscosity. A more recent idealized modelling study by Burchard et al. (2011) taking mixing asymmetries into account, shows that both lateral momentum rectification<sup>10</sup> and tidal straining circulation are of greater importance in terms of the generation of residual exchange flow than classical gravitational circulation in highly energetic environments.<sup>11</sup>

As pointed out above, how and if lateral circulation is able to generate residual along-channel estuarine exchange flow is primarily depending on its relation to the lateral shear. Nunes and Simpson (1985) described a process where due to lateral depth differences the tidal currents in the deeper part of the channel, are less effected by bottom friction and thus faster than those in the shallower part of the channel. As a consequence the horizontal density gradient is advected further in the deeper than in the shallower part of the channel, which yields a situation where the density in the deep channel is larger during flood than on

---

<sup>9</sup>The along-channel currents in figure 3.3 correspond to a flood situation, with positive along-channel velocities. The illustrated lateral shear is associated with a positive vertical vorticity component,  $\omega_z$ . If we consider the lateral circulation,  $\omega_x$ , to be positive as well, which corresponds to the red arrows, we obtain a vertically more homogeneous velocity profile (red line). For lateral circulation in the opposite sense (green arrows), we obtain a vertically stronger sheared along-channel velocity profile (green line), which in case of a flood-profile results in a negative contribution to the residual estuarine exchange flow.

<sup>10</sup>The process of momentum rectification is denoted by Burchard et al. (2011) as *advectively-driven circulation*.

<sup>11</sup>An even more recent analysis by Burchard and Schuttelaars (2012) showed that a large fraction of the *tidal straining circulation* by Burchard et al. (2011) is actually associated with lateral momentum rectification, because of its impact on the vertical shear of the along-channel velocity and thus on the viscosity-shear co-variance, which they identified with tidal straining.

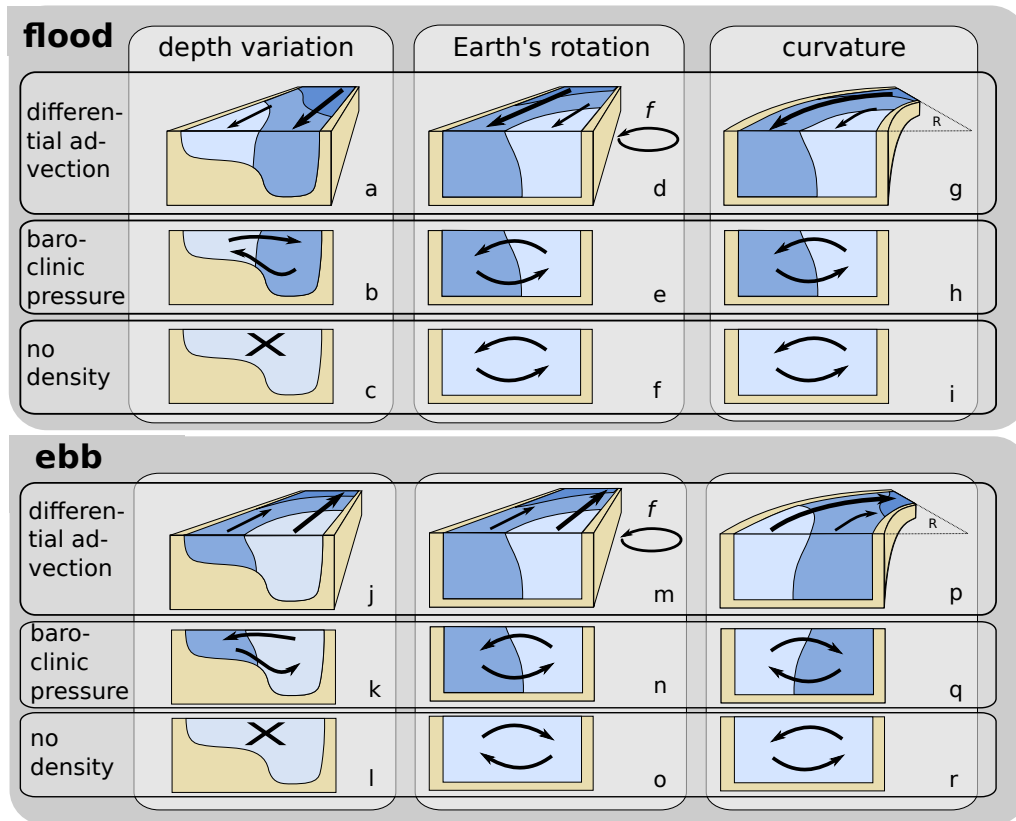


Figure 3.4.: Different drivers of lateral circulation induced by lateral depth variations (left column), Coriolis forcing (middle column), and curvature forcing (right column). The upper half of the figure shows flood and the lower half ebb situations. Each vertical triple of mini-panels illustrates the corresponding differential advection of the along-channel density gradient, the lateral circulation induced by the baroclinic pressure gradient, and the lateral circulation induced without a horizontal density gradient, respectively (density is meant to increase from light to dark blue).

the shallow shoals and vice versa during ebb (see left column figure 3.4). The associated lateral baroclinic pressure-gradient is able to drive lateral circulation (figure 3.4b). As pointed out by Lerczak and Geyer (2004) this circulation is systematically oriented in such a way that it supports classical estuarine circulation, which actually means that  $\omega_y$  and  $\omega_z$  are oriented in the same direction for both flood and ebb. The same lateral circulation process is studied by Burchard et al. (2011), but there are other processes driving lateral circulation that are able to support estuarine circulation in a similar way.

Here we like to concentrate on two other drivers for lateral circulation, namely Coriolis and centrifugal deflection of along-channel momentum. Both the Coriolis force associated with Earth's rotation and the centrifugal force associated with channel curvature tend to redistribute vertical shear of the along-channel velocity into lateral shear. Similar as for the frictional induced lateral shear, we obtain a differential advection of the along-channel buoyancy gradient, yielding a lateral baroclinic pressure gradient. In case of curvature induced differential advection the lateral buoyancy gradient is changing sign from flood



to ebb (compare figure 3.4h and 3.4q).<sup>12</sup> Coriolis deflection on the other hand produces a lateral buoyancy gradient with the same sign for both flood and ebb (compare figure 3.4e and 3.4n).

In contrast to the lateral depth variation both Earth's rotation and channel curvature are able to generate lateral circulation on their own without a density gradient as a forcing medium (Kalkwijk and Booij, 1986). Even in the absence of any density gradients centrifugal forcing and Coriolis forcing are able to deflect across-channel vorticity (vertically sheared tidal currents), into along-channel vorticity (5<sup>th</sup> and 6<sup>th</sup> term of (3.3)). The orientation of the circulation induced without the influence of buoyancy gradients is illustrated in figure 3.4f, o, i, and r for Coriolis and curvature forcing, each process for flood and ebb, respectively.

Interestingly, the lateral circulation induced by pure Coriolis deflection is orientated in such a way that it points in the same direction as the forcing of the associated lateral buoyancy gradient for flood, but in the opposite direction during ebb. Therefore, we expect an enhanced lateral circulation during flood and a reduced lateral circulation during ebb. This characteristic asymmetric lateral circulation associated with the feedback loop between buoyancy and Coriolis forcing during flood is found by Scully et al. (2009) in a numerical modelling study of the Hudson River.

As will be discussed in detail in chapter 5, a similar feedback loop exists for the interplay of curvature and buoyancy forcing. Despite the fact that many studies addressed the interplay of curvature and buoyancy forcing (e.g. Geyer (1993); Dronkers (1996); Chant and Wilson (1997); Lacy and Monismith (2001); Lacy et al. (2003); Kim and Voulgaris (2008); Buijsman and Ridderinkhof (2008); Nidziako et al. (2009)), to our knowledge no study described so far the characteristic asymmetry of lateral circulation generated by the feedback loop between centrifugal forcing and differential advection of the along-channel density gradient. Therefore, one aim of the present study is to close this gap of knowledge.

Note that both curvature and Coriolis forcing without the feedback with the along-channel buoyancy gradient would not be able to generate substantial along-channel estuarine exchange flow. Since without the density feedback  $\omega_y$  and  $\omega_z$  change their relative orientation from flood to ebb, therefore lateral momentum rectification would not provide a source of residual estuarine circulation.<sup>13</sup>

---

<sup>12</sup>The discussion of chapter 5 will show this is only true for an ordinary  $U$ -shaped curve, whereas for a  $S$ -curve  $\partial_y b$  keeps its orientation the entire tidal cycle.

<sup>13</sup>This is only true in terms of a residual exchange in the vertical, since Coriolis forcing is able to generate an residual lateral exchange flow on its own.



# 4. Sylt inlet: Tidal straining and flood tide stratification

## 4.1. Introduction

In tidal flows under the influence of horizontal density gradients in coastal waters three basic dynamic regimes have been observed to occur (Simpson et al., 1990; Verspecht et al., 2009): well-mixed flow during the entire tidal cycle, alternation between stratified and well mixed stages (strain-induced periodic stratification - SIPS) and permanently stratified regimes. The major parameter governing this tidal straining dynamics is the Simpson number

$$\text{Si} = \frac{H^2 \langle \partial_x b \rangle_{M_2}}{U_*^2}, \quad (4.1)$$

with the tidally averaged longitudinal buoyancy gradient,  $\langle \partial_x b \rangle_{M_2}$ , the mean water depth,  $H$ , and a scale for the bottom friction velocity,  $U_* = C_D^{1/2} u_A$  (with the bulk drag coefficient,  $C_D \approx 2.5 \cdot 10^{-3}$  and the tidal velocity amplitude,  $u_A$ ). In their seminal paper, Simpson et al. (1990) estimated threshold values for Si between these stages for Liverpool Bay based on current velocity  $u_A$  instead of  $U_*$ . Cast into Si as defined in (4.1), the threshold between the well-mixed and the SIPS stages was given as  $\text{Si} = 8.8 \cdot 10^{-2}$  and the threshold between SIPS and permanently stratified stages was given as  $\text{Si} = 8.4 \cdot 10^{-1}$ , i.e., of the order of unity, which means that stratifying and mixing forces are balanced (Stacey et al., 2001). The threshold values by Simpson et al. (1990) had been later confirmed for Liverpool Bay (Sharples and Simpson, 1995) but were shown to additionally depend on wind stress (Verspecht et al., 2009) and influences of Earth rotation and relative tidal frequency (Burchard, 2009).

The role of tidal straining on estuarine circulation and consequently on net onshore sediment transport has been first described by Jay and Musiak (1994). When buoyancy increases towards the coast, flood straining destabilises the water column such that mixing as well as downward momentum flux is enhanced. During ebb, mixing and downward momentum transport are reduced due to stabilisation of the water column. The tidal mean effect of this process is a near-bottom residual current directed towards the coast, with a similar effect as classical gravitational circulation (Hansen and Rattray, 1965).

There has been much emphasis in recent years to study in detail the hydrodynamics and small-scale turbulence for the SIPS phenomenon (Rippeth et al., 2001; Simpson et al., 2002, 2005). By analysing long-term current velocity profile data at small Si numbers  $< 8 \cdot 10^{-2}$  (indicating well-mixed conditions), Flöser et al. (2011) could show that flood velocity profiles are vertically more homogeneous than ebb profiles due to tidal straining, with the asymmetry depending on the Si number. Thus, the presence of estuarine circulation can be expected even for such well-mixed flows. Using residual flow profile decomposition for

idealised model simulations of tidal flow, Burchard et al. (2011) concluded for well-mixed flows that tidal straining has a substantially stronger impact on estuarine circulation than gravitational circulation.

The major objective of this chapter is to analyse field observations of current velocity, temperature, salinity, small-scale turbulence and suspended matter profiles to directly confirm for flows with small  $Si$  numbers the presence of the tidal straining mechanism for driving estuarine circulation as sketched by Jay and Musiak (1994). This chapter also aims at offering tidal straining as an explanation for the phenomenon of the estuarine circulation in the Wadden Sea as observed by Flöser et al. (2011) and as a mechanism for driving net sediment fluxes into the Wadden Sea, as hypothesised by Burchard et al. (2008).

## 4.2. Field observations

### 4.2.1. Study site

The measurements were carried out in the *Lister Deep*, a curved tidal channel up to 40 m deep connecting the Sylt-Rømø Bight in the northern part of the Wadden Sea with the North Sea (Figure 4.1). The *Lister Deep* transforms into a distinct ebb tidal delta in seaward direction and branches into three channels in landward direction. The average freshwater discharge per tidal cycle of two small rivers amounts to about  $10^6 \text{ m}^3$ . During the warming period in spring, horizontal thermal buoyancy gradients emerge due to differential heating of the shallow Wadden Sea water (Burchard et al. (2008)) such that strongest buoyancy gradient forcing is expected during April to June.

### 4.2.2. Instrumentation and data analysis

In order to obtain some insight into the estuarine circulation process and the associated sediment transport, a short ship campaign was carried out in the *Lister Deep* during April 15-17, 2008.

The current velocity was measured by a vessel-mounted Acoustic Doppler Current Profiler (1200 kHz, Workhorse Broadband ADCP, Teledyne-RD Instruments). A bin resolution of 0.25 m and a sampling frequency of 0.5 Hz was used. To reduce the noise level the data were averaged over 180 s. The current vector was rotated into the current direction at the instance of strongest flood (rotated by  $11^\circ$  in clockwise direction with respect to east for April 15).

Furthermore, a multi-probe (Sea & Sun Technology, Trappenkamp, Germany) was utilised, equipped with sensors measuring conductivity, temperature and pressure, as well as some optical quantities as fluorescence, Photosynthetic Photon Flux Fluence Rate, optical back scattering with an 880 nm laser diode and optical transmission of a LED (660 nm) with 3 optical path lengths (1, 4 and 12 cm). The latter, in combination with reference suspended particulate matter (SPM) samples, is used to calculate SPM concentrations. Those samples were taken by pumping water through a tube, fixed next to the turbidity sensor of the multi-probe. The immediate filtration of this water, using filters

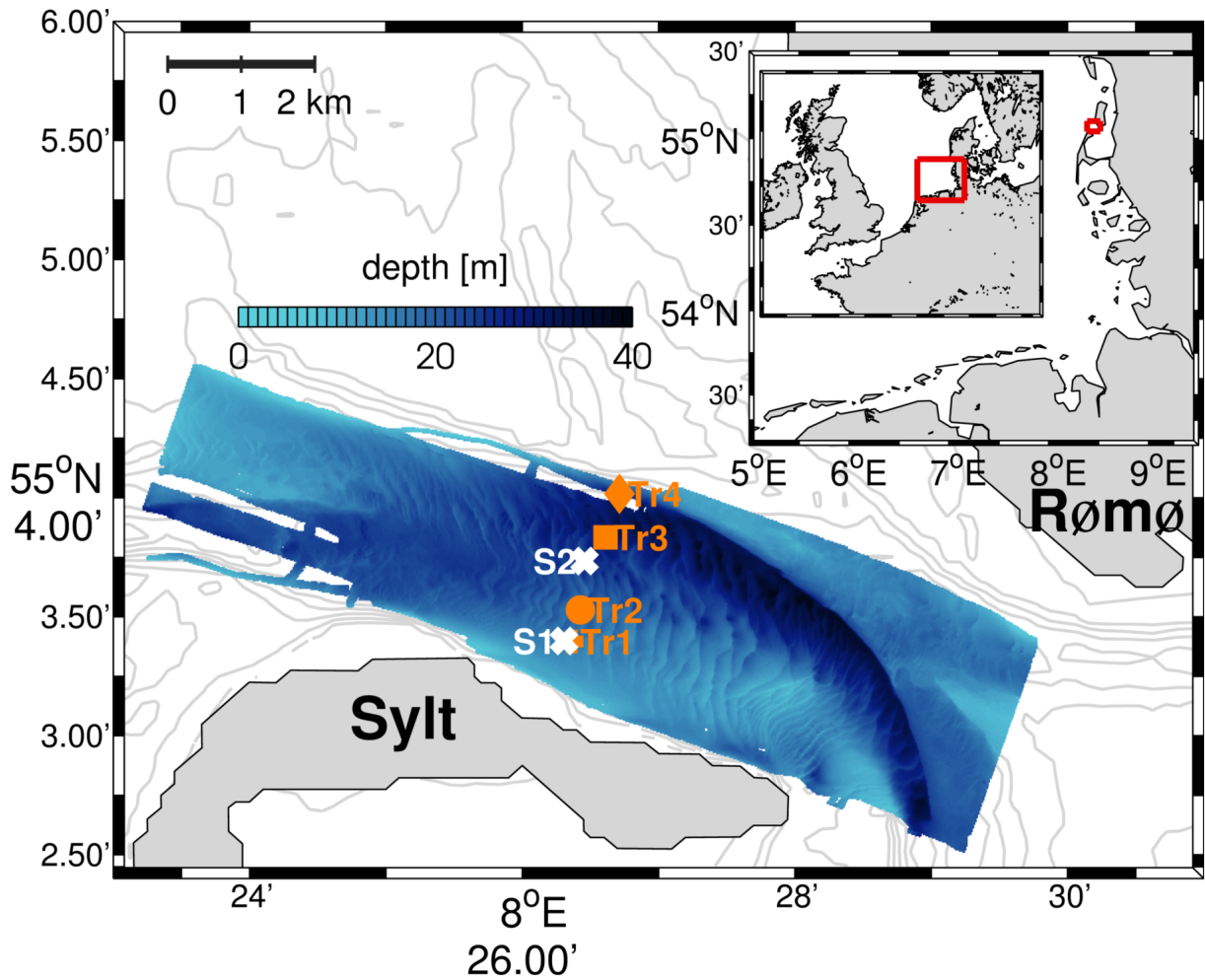


Figure 4.1.: Map of the study-site showing water depth from multi-beam soundings (gray scale) and bathymetric charts (gray lines). S1 and S2 mark the measurement positions on April 15 and 17, respectively, and the transect stations Tr1-Tr4 (symbols) on April 16. The inserted maps show the coastlines of the North Sea (smaller map) and the German Bight areas (larger map). The transect stations are marked from south to north as + (Tr1), ● (Tr2), (Tr3), and ◊ (Tr4).

with a pore size of approximately  $1.2 \mu\text{m}$  (Whatman GF/C), and subsequent conservation of the filters at  $-20 \text{ }^\circ\text{C}$  ensured a proper analysis of the SPM samples in the laboratory.

In addition, a free-falling MSS90 micro-structure profiler (ISW Wassermess-technik, Fünfseen, Germany) was used to obtain information about several turbulent parameters. The MSS90 is equipped with precision CTD sensors (Sea & Sun), a fast-response temperature sensor (FP07), pressure-sensor, as well as two airfoil shear probes (PNS06 from ISW) to analyse micro-scale vertical shear. All sensors were sampling at 1024 Hz with 16 bit resolution, while the profiler was free-falling with a speed of  $0.27\text{--}0.38 \text{ m s}^{-1}$ .

Dissipation rates were obtained by integrating vertical shear spectra, assuming local isotropy in the dissipative subrange (for details, see Moum et al. (1995)). To quantify tidally induced turbulence the friction velocity,  $u_*^b = \sqrt{\tau_b/\rho_0}$ , is calculated by using the law-of-the-wall scaling over the first 1.25 m above the bottom (see equation (2.18)). As a measure for the stability of the water column, the potential energy anomaly  $\Phi$  has been defined by Simpson (1981) as the amount of mechanical energy (per  $\text{m}^3$ ) required to instantaneously homogenise the water column with a given density stratification (see equation (2.7)).

### 4.2.3. Field work

The measurements were made at three subsequent days during April 15-17, 2008. On the first and third day fixed station measurements were carried out at S1 and S2 (Figure 4.1), respectively, with S1 being a shallow station (14.8 m depth) at the southern edge and S2 a deep station (23.2 m depth) near the middle of the channel. During the second day (April 16) measurements were taken along a cross-channel transect consisting of four different stations (see Tr1-Tr4 in Figure 4.1). The vessel was repeating this transect from south to north five times during this day. The weather conditions were stable during the whole campaign, with north-westerly winds of approximately  $5 \text{ m s}^{-1}$  during the first two days. In the night after April 16 the wind changed to north-easterly direction with approximately  $5 \text{ m s}^{-1}$  during the last day (see Figure 4.2a).

Observations were carried out between 7 and 9 hours per day, thus not covering an entire tidal cycle, but day one and three combine to a full cycle between low waters (LW) (see gray-shaded areas in Figure 4.2). The measurements at station S1 contain a complete ebb (negative along-channel velocity) period and at S2 a complete flood (positive along-channel velocity) period. Generally, high water (HW) coincides with slack after flood and low water (LW) with slack after ebb (Figure 4.2b). During flood, salinity increases and temperature decreases and vice versa during ebb (Figure 4.2c), which is a clear sign for the presence of a horizontal density gradient with onshore waters being less dense than offshore waters. The density gradient is dominated by the salinity gradient with some additional contribution from temperature. By reverting the vertically integrated temperature and salinity equations (see Verspecht et al. (2009) for details), average horizontal buoyancy gradients of  $\partial_x b = 1.3 \cdot 10^{-6} \text{ s}^{-2}$  and  $\partial_x b = 0.6 \cdot 10^{-6} \text{ s}^{-2}$  result for April 15 and 17, respectively. Together with the water depths given above and the maximum bottom friction velocity values of  $U_* = 0.04 \text{ m s}^{-1}$  and  $U_* = 0.05 \text{ m s}^{-1}$ , respectively, (4.1) results in Simpson numbers of  $\text{Si} = 0.18$  and  $\text{Si} = 0.13$  for April 15 and 17, respectively. With respect to the estimates by Simpson et al. (1990) both values are in the low end of the

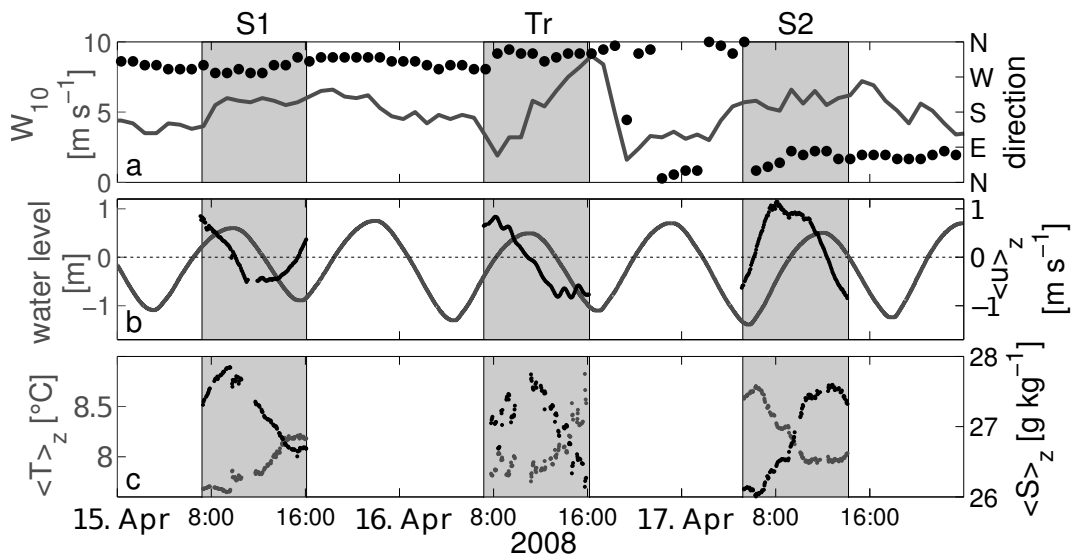


Figure 4.2.: Observations in Lister Deep during April 15-17, 2008. (a) Wind speed (dark-gray) and direction (black dots) in List/Sylt (approximately 10 km south of the study site); (b) sea-level height (gray) in List/Sylt and depth-mean along-channel velocity component (black) from vessel-mounted ADCP; (c) vertical mean of temperature (gray) and salinity (black) from MSS and CTD. The high-lighted boxes indicate the ship-based observational periods, corresponding to the stations illustrated in Figure 4.1.

SIPS range (see section 4.1), such that some dynamical effects such as tidal straining and weak periodic stratification should be expected.

### 4.3. Results

Figure 4.3 shows profiling observations obtained on April 15 at station S1. Positive current velocities in Figure 4.3a indicate flood, which lasts until 9:30 h (slack after flood). As seen before in Figure 4.2c, salinity increases and temperature decreases during flood (see Figure 4.3b,c), and vice versa during ebb. The interpretation of the SPM concentration dynamics is more complicated, because it is determined by lateral advection as well as by the interplay between vertical settling and mixing. A clear signal from horizontal SPM gradients is not visible, although SPM concentrations in the Wadden Sea are expected to be substantially higher than in the North Sea (Burchard et al. (2008)).

During flood (before 9:30 h) vertical stratification basically vanishes with values of  $N^2 < 10^{-5} \text{ s}^{-2}$  and unstable stratification is observed in the lower half of the water column (Figure 4.3d). Salinity, temperature and SPM profiles are vertically almost homogeneous (Figs. 4.3b,c,f) due to strong vertical mixing, as indicated by high values of dissipation rate with typical values of  $10^{-4} \text{ W kg}^{-1}$  in the middle of the water column (Figs. 4.3e). SPM concentrations show the highest concentrations during flood ( $\approx 50 \text{ mg l}^{-1}$ ), which can partially be explained by strong bottom shear stress (resulting in high resuspension rates) and high vertical mixing (resulting in vertical homogenisation). By the end of the flood (around 9:00 h), stratification increases in the upper half of the water column, in connection with decreased vertical mixing (indicated by decreased  $\varepsilon$ ).

At slack after flood (9:30 - 10:30 h), strong salinity and temperature stratification develops over the entire water column, due to exchange flow caused by horizontal buoyancy gradients, leading to peak values of  $N^2 \approx 10^{-3} \text{ s}^{-2}$ . The SPM concentration in the water column decreases since SPM settling is now stronger than vertical SPM mixing. For a short while, the dissipation rate is low over the entire water column ( $\varepsilon < 10^{-6} \text{ W kg}^{-1}$  at 9:30 h), but reaches values of  $\varepsilon \approx 10^{-5} \text{ W kg}^{-1}$  shortly afterwards. The processes driving this generation of turbulence during the phase of strongest stratification are not clear. It could be speculated that breaking of internal waves is one of the reasons.

During the subsequent ebb phase, stratification remains marginally stable, with typical mid water values of  $N^2 \approx 10^{-4} \text{ s}^{-2}$  due to salinity and temperature stratification. Also the SPM concentration remains stratified during the entire ebb period. This is due to reduced vertical mixing since even during full ebb, around 13:00 h, the dissipation rate remains at relatively low values of  $\varepsilon \approx 10^{-5} \text{ W kg}^{-1}$ .

During the subsequent slack tide after ebb, SPM concentrations reach a minimum, which can be explained by the lowest dissipation rate observed during this tidal cycle with values of  $\varepsilon \approx 10^{-7} \text{ W kg}^{-1}$ . The fact that despite these low turbulence levels, stratification is not increasing during slack after ebb (around 15:30 h), is a sign for a small value of the horizontal buoyancy gradient. This can be seen by the small decrease in density (despite prevailing ebb currents) during the last phase of ebb (14:00 h - 15:00 h), see Figure 4.3a-c.

The temporally resolved bottom friction velocity shows good agreement between estimates from the ADCP velocity and the MSS dissipation rate, when both are fitted to law of the wall scaling near the bed, indicating maximum flood values of  $u_*^b = 0.04 \text{ m s}^{-1}$



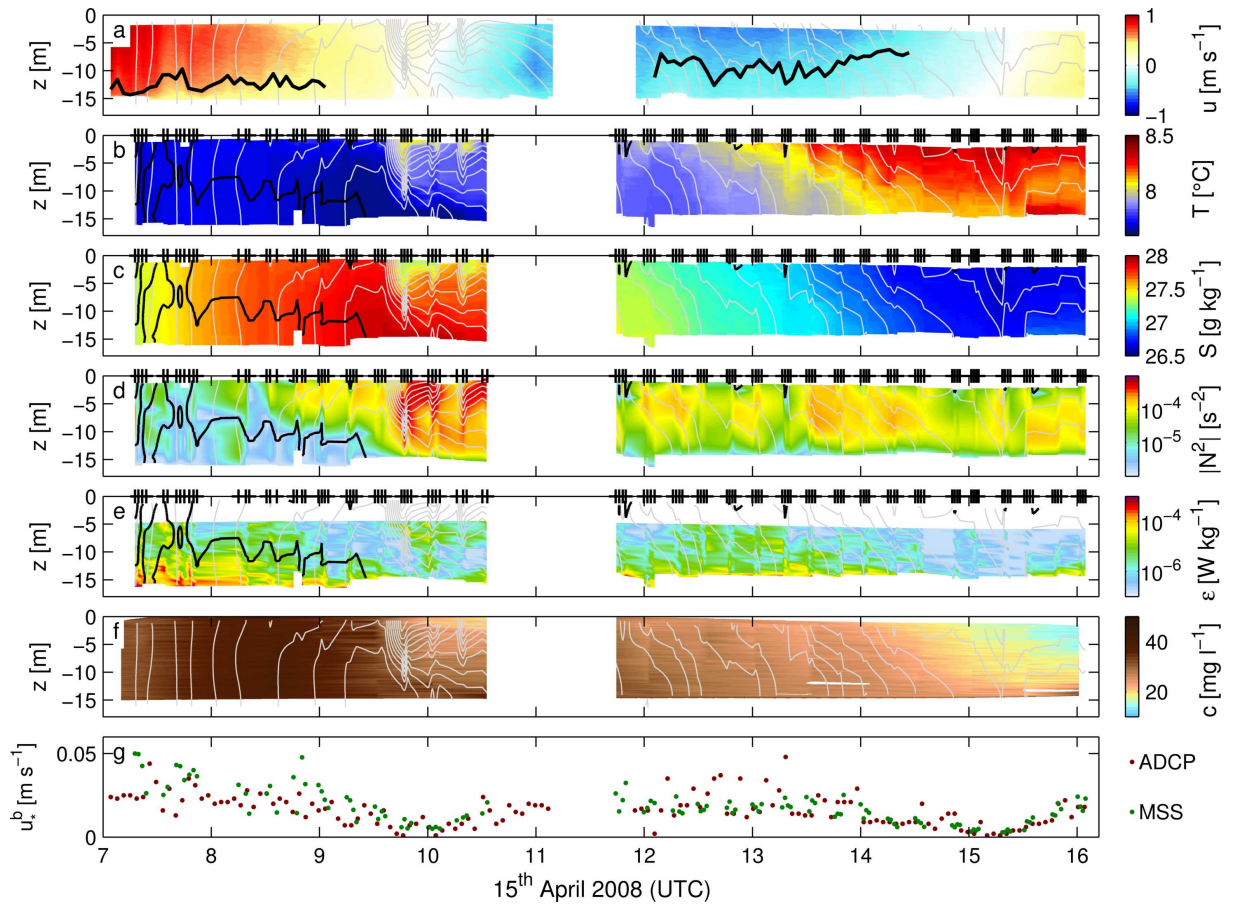


Figure 4.3.: Observed profiles on April 15, 2008 at station S1 (see Figure 4.1), with (a) showing the current velocity. (b) and (c) illustrate the temperature and salinity, respectively, (d) the buoyancy-frequency,  $N^2$ , and (e) the dissipation-rate of TKE. (b)-(e) are based on MSS-profiles, which are marked by black crosses atop the panels. (f) displays the SPM concentration. The light-gray lines, occurring in each panel, are isopycnals and the black line encloses areas of unstable vertical stratification ( $N^2 < 0$ ). (g) shows the temporally resolved bottom friction velocity,  $u_*^b$ , based on ADCP-data (red) and dissipation rates from the MSS (green).

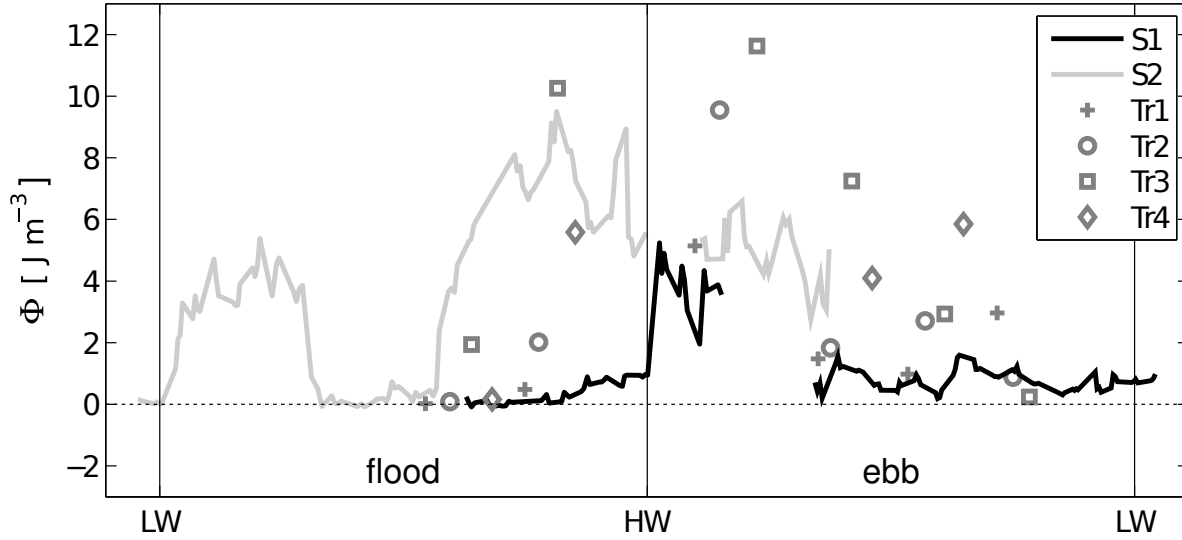


Figure 4.4.: Potential energy anomaly,  $\phi$ , for all profiles observed during April 15-17 in Lister Deep, with time normalised to high water (HW). The different dark gray symbols mark the certain transect stations on April 16 (see 4.1a).

and somewhat smaller maximum ebb values of  $u_*^b = 0.03 \text{ m s}^{-1}$ , with slack tides around 10:00 h and 15:30 h. Based on these data, the friction velocity scale has been estimated as  $U_* = 0.04 \text{ m s}^{-1}$ , see section 4.2.3.

At station S1, the potential energy anomaly  $\phi$  shows the expected tidal cycle, with values around zero (indicating well-mixed conditions) during late flood, strong increase during slack and marginally but significantly stable values during ebb (Figure 4.4). Also the observations from April 16 at the two southern stations Tr1 and Tr2 along the transect show a comparable behaviour. However, the two northern transect stations Tr3 and Tr4 and also the observations at the northern anchoring station S2 taken during April 17 deviate from this classical picture. While during slack after ebb stratification increases significantly and is completely eroded during full flood (supporting the classical picture), stratification increases significantly just after full flood. On April 17, this occurs at a depth-mean flood velocity of about  $0.8 \text{ m s}^{-1}$  and at Tr3 and Tr4 on April 16 comparably high flood velocities are observed during sudden stratification (not shown). At this point, it is not clear where this rather surprising full flood stratification comes from and why it is occurring only at the northern but not on the southern side of the channel. Possible explanations for this unexpected behavior are one of the major subjects of the following chapters, dealing with a similar phenomenon in different but comparable environments.

## 4.4. Discussion and conclusions

At station S1, the dynamic impact of tidal straining is clearly seen from a number of independent profiling observations: temperature and salinity are well mixed during flood and significantly stratified during ebb, with a maximum stratification during the slack

tide in between; the SPM concentration profiles show a similar behaviour with strong homogenisation during flood and stably stratified profiles during ebb, with substantial sedimentation during slack tides; the turbulent dissipation rate is high throughout the water column during flood, but restricted to near-bottom turbulence during ebb, with decreased values during slack. With the data set presented here, the dynamics of tidal straining have been directly shown for the first time in the Wadden Sea, an area for which dynamic effects of density gradients have been neglected in most of the past studies. The long term data studies by Burchard et al. (2008) and Flöser et al. (2011) indicate the generality of this phenomenon in the Wadden Sea.

However, the observations at stations S2 (on April 17) and Tr3 and Tr4 (on April 16) with the increasing stratification just after full flood show that the dynamics may not always be as observed at station S1 (on April 15). It is well known that even for simple channel geometries lateral straining (see Burchard et al. (2011) and references therein) can generate complex flow patterns which significantly modify along-channel straining and residual circulation. It is therefore not surprising that the classical picture is modified in the curved channel considered here in connection to its distinct ebb tidal delta in seawards direction and the branching channel system in landward direction.

A quantification of the net SPM fluxes into the Wadden Sea can thus not be achieved by observations only. Instead, well-calibrated realistic numerical models reproducing all relevant processes in a quantitative sense are the only way to succeed in estimating net SPM fluxes. The observations presented and analysed here show the complexity of such a modelling task. Specifically, processes of baroclinicity and their interaction with topography need to be represented.



# 5. Spiekerroog inlet: Asymmetric lateral circulation

## 5.1. Introduction

Understanding estuarine circulation, i.e. the residual exchange flow with a near-bottom inflow compensated by a near-surface outflow, is crucial when studying estuarine dynamics, since it plays a major role in transporting salt, nutrients and suspended sediment. Traditionally it is thought to be caused by the relaxation of a longitudinal density gradient, which is an immanent feature of all estuaries. This process is usually referred to as gravitational circulation (Pritchard, 1952, 1954, 1956; Hansen and Rattray, 1965; MacCready and Geyer, 2010; Geyer and MacCready, 2013).

During the last two decades a large number of other processes has been discovered that are also able to cause estuarine circulation. Nearly all those processes are caused by asymmetries in the tidal currents between ebb and flood, many of which are induced by density-forcing (Jay and Musiak, 1994, 1996; Stacey et al., 2001, 2008). Differences in the strength of vertical stratification between ebb and flood, e.g. due to tidal straining (Simpson et al., 1990; Stacey, 1996; Becherer et al., 2011), lead to tidal differences in vertical mixing of momentum, yielding asymmetric vertical shear of the along-channel momentum, which ultimately is able to generate residual estuarine circulation. Especially in well-mixed estuaries, such internal asymmetries are found to be of greater importance in terms of the generation of estuarine exchange flow than classical gravitational circulation (Burchard and Baumert, 1998; Burchard and Hetland, 2010; Burchard et al., 2011).

In contrast to many of these previous studies that have focused on just the longitudinal (along-estuary) dimension, it has become clear in recent years that estuarine circulation and estuarine dynamics are influenced to a large extent by lateral exchange flow (e.g. Lerczak and Geyer (2004); Scully et al. (2009); Burchard et al. (2011)).

Beside Coriolis deflection of along-channel momentum (e.g. Alaei et al. (2004); Buijsman and Ridderinkhof (2008); Huijts et al. (2009)), lateral or secondary circulation is mainly due to either density forcing or bathymetric features interacting with tidal currents. Bathymetric curvature alone is able to generate lateral circulation (e.g. Kalkwijk and Booij (1986); Alaei et al. (2004); Buijsman and Ridderinkhof (2008)), but in most estuaries the interaction of bathymetry with horizontal density gradients provides an important driver of secondary circulation (e.g. Nunes and Simpson (1985); Geyer (1993); Dronkers (1996); Lerczak and Geyer (2004); MacCready and Geyer (2010)).

Nunes and Simpson (1985) described for instance how a lateral variation of channel depth leads to differential advection of along-channel density gradients due to differences in bed friction on the along-channel momentum. This differential transport is able to generate strong lateral density gradients, often larger than the along-channel gradients,

which are able to drive lateral circulation. In the deepest part of the channel (or thalweg), this type of bathymetrically controlled secondary circulation leads to surface-convergent flows during flood and surface-divergent flows during ebb (i.e., a two-cell structure of the lateral circulation).

Based on an idealized modelling study, Lerczak and Geyer (2004) pointed out that the bathymetrically controlled lateral circulation first described by Nunes and Simpson (1985), is asymmetric with respect to the tidal cycle, with stronger lateral circulation during flood than during ebb, which makes it an important driver for estuarine circulation. The associated difference in lateral momentum transport yields an asymmetry in the vertical shear of along-channel momentum resulting in a residual estuarine exchange flow in a similar manner as tidal straining (Jay and Musiak, 1994). Lerczak and Geyer (2004) found that this process is often at least as important as classical gravitational circulation.

Another important source of lateral circulation are curved flows, which are due to topographic features like curved tidal channels or headlands. Even in the absence of any density variation flow-curvature is able to yield significant secondary circulation (e.g. Kalkwijk and Booij (1986); Alaei et al. (2004); Buijsman and Ridderinkhof (2008)). The reason is a deflection of the vertically sheared along-channel momentum, due to centrifugal forces, which leads, in association with a compensating barotropic pressure gradient, to a lateral exchange flow.

The interaction of curvature induced lateral circulation and density gradients is a complex field. In strongly stratified systems for instance, vertical stratification is known to reduce lateral circulation due to the associated tilting of isopycnals, which builds up a baroclinic pressure gradient that is able to compensate curvature induced lateral circulation (e.g. Chant and Wilson (1997); Chant (2002); Seim and Gregg (1997); Lacy and Monismith (2001); Kim and Voulgaris (2008)).

On the other hand, in weakly stratified systems vertical stratification has the tendency to increase lateral circulation, due to its inhibiting effect on vertical mixing of momentum (Geyer, 1993; Dronkers, 1996; Buijsman and Ridderinkhof, 2008). In such systems secondary circulation can also generate vertical stratification due to straining of lateral density gradients (Lacy et al., 2003; Cheng et al., 2009; Scully and Geyer, 2012). Both effects might yield a positive feedback loop between lateral circulation and vertical stratification.

So far a number of studies addressed the interplay of lateral buoyancy forcing and curvature forcing (Geyer, 1993; Dronkers, 1996; Lacy and Monismith, 2001; Buijsman and Ridderinkhof, 2008; Nidzieko et al., 2009; Waterhouse and Valle-Levinson, 2010). In this study we develop a consistent framework for investigating the interplay of the different generation mechanisms of lateral and longitudinal circulation, which provides a direct link between secondary circulation and estuarine exchange flow. Applying this framework to observational data, taken in the German Wadden Sea, a well-mixed estuary with strong tidal forcing, will demonstrate how curvature-induced lateral circulation and its interplay with horizontal density gradients is in control of vertical stratification and provides an important contribution to the net estuarine exchange flow.

In section 5.2 we describe the underlying field campaign, the study-site, the instrumentation and experiment, as well as the the basic data processing routines. The following section 5.3 is dedicated to the theoretical framework used to quantify the mechanisms

responsible for the occurrence of lateral and longitudinal circulation as well as vertical stratification. The observational results are presented in section 5.4, followed by an extended discussion of the underlying mechanisms in section 5.5. This section also contains a discussion of the interplay of lateral circulation and horizontal buoyancy gradients, based on a conceptual model. Section 5.5 closes with implications of the described asymmetrical lateral circulation process for the residual along-channel exchange flow. The last section 5.6 is used to conclude the findings of this study.

## 5.2. Field campaign

### 5.2.1. Study site

The measurements were conducted in the tidal inlet between the islands of Langeroog and Spiekeroog, in the German Wadden Sea (see Figure 5.1). The associated back-barrier basin is characterized by large inter-tidal flats, separated by tidal channels and small gullies. The major tidal channel in this basin is up to 15 m deep and has a pronounced *S*-shaped curvature (see Figure 5.1). It is important to note that all measurements discussed in this paper have been taken at the inflection point of this *S*-curve.

Especially in spring the site is mostly characterized by a small but significant horizontal density gradient, where the water in the back-barrier basin is usually less dense than the water from the open North Sea, due to differential heating and rainfall (i.e., the density gradient is due to both temperature and salinity variations). This density gradient is believed to drive estuarine circulation in the Wadden Sea (Burchard et al., 2008).

The tidal currents in the inlets of the Wadden Sea are relatively strong, with peaks between one and two meters per second. The associated turbulent mixing in combination with the weak horizontal density gradients, makes the Wadden Sea a well-mixed estuary, in which only at certain stages of the tidal cycle significant vertical stratification can be observed.

### 5.2.2. Instrumentation

The velocity data discussed in this paper are measured by a moored (bottom mounted) 1.2 MHz ADCP at station *A*, operating in mode 12, and a vessel-mounted Workhorse Broadband ADCP (TeledyneRD Instruments, 1.2 MHz) at station *S*. The data of both ADCPs have been averaged over 60 s intervals and 25 cm vertical bins in case of the bottom mounted and 50 cm bins in case of the vessel mounted ADCP.

Near the mooring, we used a free-falling micro-structure profiler, *MSS90* (ISW Wassermesstechnik), equipped with a fast response temperature sensor (FP07), a precision CTD sensor (Sea & Sun Technology), a pressure sensor, and two airfoil shear probes (PNS06 from ISW Wassermesstechnik) to analyse small-scale vertical shear. All sensors were sampling at 1024 Hz, while the profiler was free-falling with a speed of 0.3-0.5 m s<sup>-1</sup>. The profiler was deployed from a small boat. There was a fast winch attached to that boat that made it possible to release the data cable of the *MSS90* fast enough in order to let it free-fall, even at current speeds of more than 1 m s<sup>-1</sup>, which was necessary to obtain valid turbulence measurements.

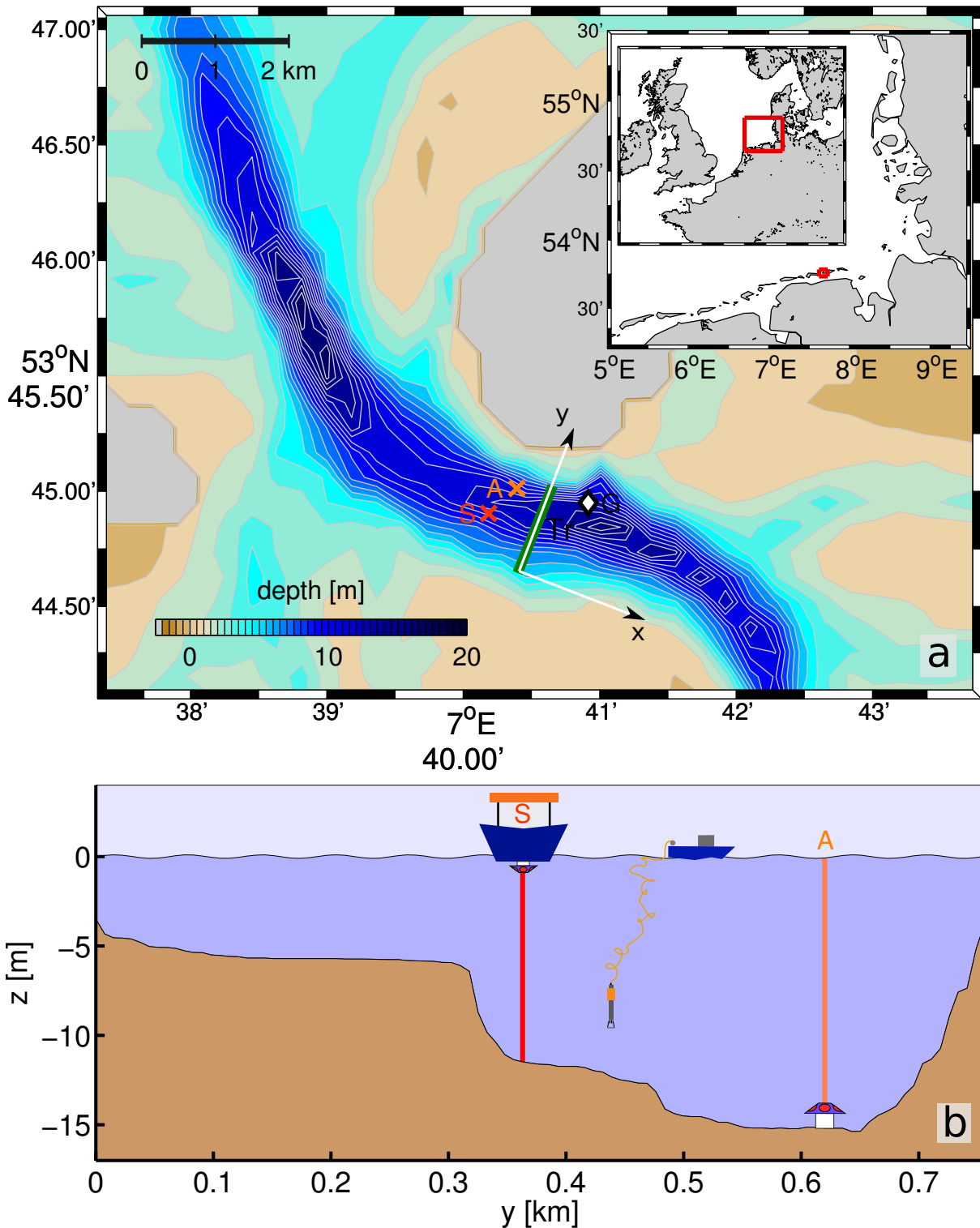


Figure 5.1.: Study Site. Panel (a) shows a map of the study site in the tidal inlet, between the islands of Langeoog in the West and Spiekeroog in the East, in the German Wadden Sea. The colored contours display the average water depth.  $S$  marks the position of the permanently anchored vessel, R/V Ludwig Prandtl,  $A$  the position of the moored ADCP,  $G$  the position of the gauge and the green line labeled with  $Tr$  indicates the cross-channel transect carried out by a small vessel. The cross-section of the transect  $Tr$  is displayed in panel (b), with the projected positions of the moored ( $A$ ) and the vessel mounted ( $S$ ) ADCP, respectively.



Furthermore, during the full duration of the experiment measurements of temperature and conductivity were collected with a Sea Bird MicroCat CTD-sensor (SBE 37) moored close to station *A*, at a depth of 1.5 m. It continuously recorded data at a sampling frequency of 0.05 Hz from 8<sup>th</sup> to 22<sup>nd</sup> May 2011.

### 5.2.3. Measurements

The measurements analysed in this study are part of a longer survey that took place in May 2011 and lasted for about 2 weeks. During this time the moored ADCP and the associated CTD-sensor (see *A* in Figure 5.1) measured continuously.

The ship-based measurements, like the vessel-mounted ADCP and the micro-structure measurements, were separated into two independent periods. During the first period from 10 May until 14 May, R/V *Ludwig Prandtl* was anchored at a position close to the center of the channel indicated by *S* in Figure 5.1. Due to strong winds it was necessary to interrupt the vessel mounted measurements from 14 May until 17 May.

Afterwards, from 17 to 19 May 2011, the *Ludwig Prandtl* continued to collect ADCP-data at station *S*, whereas the micro-structure measurements were conducted from a smaller boat. This boat permanently operated on the cross-channel transect indicated by the dark green line in Figure 5.1. During each channel crossing, 8 to 20 microstructure profiles were obtained within a period of 10 to 25 minutes.

The data analyzed for the present study are exclusively taken during the last transect period.

### 5.2.4. Basic data-processing

#### Transect Projection

All microstructure profiles obtained during the cross-channel observations were projected on an approximately 750 m long standard transect, *Tr*, chosen to be perpendicular to the tidal flow direction in the channel and situated approximately in the center of the cloud of profiles (see Figure 5.1). The average bathymetry of the transect is shown in figure 5.1 with a fairly shallow region of about 5 m depth in the first 300 m and a deeper northern part, with depths up to 15 m. The red and the orange lines show the projection of the vessel-mounted and the moored ADCPs respectively.

For further analysis the profile data were interpolated onto a temporal-spatial grid ( $\Delta t = 5$  min;  $\Delta y = 10$  m).

#### Coordinate-system

Note that our coordinate system is aligned with the transect, setting the origin at the southern end of it (see Figure 5.1), which yields a vanishing tidally averaged cross-channel (*v*) component of the velocity for station *A* and approximately for station *S* as well.

The *z*-axis is pointing positively upwards with its origin at the mean water-level. Correspondingly, *w* denotes the vertical velocity-component. The bottom is therefore located at  $z = -H$ , and the free surface at  $z = \eta$ , such that the total water depth is  $D = H + \eta$ .

### Horizontal buoyancy gradients

The along-channel buoyancy gradient,  $\partial_x \langle b \rangle_z$ , is calculated assuming a balance between the rate of change of the gradient and the along-channel advection term in the transport equation for the buoyancy. We further assume a well-mixed water column to correlate point measurements with a depth-average,

$$\partial_x \langle b \rangle_z \approx \partial_x b \approx \frac{1}{u} \partial_t b, \quad (5.1)$$

where here and in the following  $\partial_x$  and  $\partial_t$  denote partial derivatives with respect to space and time, respectively, and  $\langle \cdot \rangle_z$  the depth-average (Verspecht et al., 2009).  $b$  is the buoyancy and accounts for the dynamical influence of density,

$$b = -g \frac{\rho - \rho_0}{\rho_0}, \quad (5.2)$$

where  $\rho$  is density,  $g$  the acceleration of gravity, and  $\rho_0$  a constant reference density, here chosen to be  $1000 \text{ kg m}^{-3}$ . The long time series of  $\partial_x \langle b \rangle_z$  shown in Figure 5.2 is based on a moored CTD-sensor located close to station *A* approximately 1.5 m underneath the surface and velocity data of the ADCP at station *A*, where for consistency the velocity is averaged over the upper 3 m of the water-column.

To remove the short-term variability in the buoyancy gradient, we smoothed the instantaneous values of  $\partial_x \langle b \rangle_z$  with a moving box filter over one  $M_2$  tidal period (Verspecht et al., 2009). In order to ensure that the approximations (5.1) are valid, only data points with an average velocity of more than  $0.3 \text{ m s}^{-1}$  are considered, accounting still for about 75% of the data, excluding only slack tides.

The lateral buoyancy gradient,  $\partial_y \langle b \rangle_z$ , is calculated based on the gridded transect data, which provide a vertically averaged two-dimensional distribution of the buoyancy,  $\langle b \rangle_z(y, t)$ . In order to obtain a value for  $\partial_y \langle b \rangle_z$  at any point in time and space a linear regression is used. Each depth-averaged profile,  $\langle b \rangle_z$ , within a lateral distance of 50 m is fit with a line, where the slope of the line corresponds to  $\partial_y \langle b \rangle_z$ . The 50 m radius ensures a sufficient number of profiles, but at the same time allows for enough lateral variability of  $\partial_y \langle b \rangle_z$ . There is a large difference in depth between shoal and channel (see Figure 5.1), therefore the lateral buoyancy gradient over the shoal is calculated with the depth-averaged buoyancy over the upper 5 m of the water-column, whereas for the channel the depth mean of the upper 10 m is used, corresponding to the characteristic depth of the shoal and channel region, respectively (see Figure 5.1).

### Dissipation rates and friction velocity

If we assume local isotropy for the dissipative sub-range of the shear spectra, which are obtained from the shear probes of the micro-structure sonde, an integration of those spectra yields the dissipation rates of turbulent kinetic energy,  $\varepsilon$  (for details see Fer (2006); van der Lee and Umlauf (2011)). This procedure provides dissipation rates for each of the two shear probes, which are averaged over 0.5 m bins.

Based on these dissipation rates it is possible to calculate the bottom friction velocity,  $u_*$ , by assuming the law-of-the-wall,

$$u_* = [\kappa \varepsilon (z + H)]^{\frac{1}{3}}. \quad (5.3)$$

Here  $\kappa = 0.41$  denotes the *von Karman*-constant. Since the basis for equation (5.3) is a balance between shear production and dissipation of turbulent kinetic energy, it is only valid in the well mixed near bottom region. Therefore, only the lower three bins of the dissipation rates have been considered, corresponding to the first 1.5 m above the bottom.

## 5.3. Theoretical framework

### 5.3.1. Potential energy anomaly $\Phi$

Simpson (1981) defined the potential energy anomaly as a measure for vertical stratification: *the work per unit volume required to bring about vertical redistribution of the mass in complete mixing*,

$$\Phi = \frac{g}{D} \int_{-H}^{\eta} (\langle \rho \rangle_z - \rho) z \, dz . \quad (5.4)$$

In contrast to former studies (Simpson and Hunter, 1974; Simpson et al., 1990) that treated the evolution of the potential energy in a more empirical way, Burchard and Hofmeister (2008) and De Boer et al. (2008) independently derived an exact transport equation for  $\Phi$ . Here we follow the approach of Burchard and Hofmeister (2008). In contrast to other studies using that balance to study the generation of vertical stratification (Burchard and Hofmeister, 2008; Hofmeister et al., 2009; Cheng et al., 2009), we have to ignore a number of terms since our underlying measurement data are not as complete as the data obtained by three-dimensional models. Therefore, we have to ignore all surface fluxes, internal sources, horizontal mixing, vertical advection, as well as the non-mean straining and the horizontal advection terms depending on the along-channel gradient of  $\Phi$  that cannot be sufficiently well estimated from the available data set. Considering these simplifications, the equation for  $\Phi$  becomes,

$$\begin{aligned} \overbrace{\frac{\Phi_t}{\partial_t \Phi}} &= - \overbrace{\langle v \rangle_z \partial_y \Phi}^{\Phi_{A1y}} - \frac{\Phi}{D} \left[ \overbrace{\frac{\Phi_{A2}}{\partial_t \eta}} + \overbrace{\langle v \rangle_z \partial_y H}^{\Phi_{A3y}} \right] \\ &\quad - \frac{\rho_0}{D} \left[ \overbrace{\partial_x \langle b \rangle_z \int_{-H}^{\eta} z \tilde{u} \, dz}^{\Phi_{Sx}} + \overbrace{\partial_y \langle b \rangle_z \int_{-H}^{\eta} z \tilde{v} \, dz}^{\Phi_{Sy}} \right] \\ &\quad + \overbrace{\frac{\rho_0}{D} \int_{-H}^{\eta} \left( \eta - \frac{D}{2} - z \right) \tilde{v} \partial_y \tilde{b} \, dz}^{\Phi_{nSy}} + \overbrace{\frac{\rho_0}{D} \int_{-H}^{\eta} \langle w' b' \rangle \, dz}^{\Phi_{mix}} , \end{aligned} \quad (5.5)$$

where  $\tilde{\cdot}$  denotes the deviation of a quantity from its depth mean  $\langle \cdot \rangle_z$ .

The terms in (5.5) labeled with  $\Phi_{A1y}$ ,  $\Phi_{A2}$ , and  $\Phi_{A3y}$  are different advection terms, where we ignored all horizontal gradients of the surface elevation,  $\eta$ , as well as the along-channel gradient of  $H$  and  $\Phi$ . The latter assumption might result in the largest errors, since along-channel advection of stratification generated elsewhere could be important in

complex basin geometries like in the Wadden Sea. Nevertheless, with the available data we can not estimate that term.

Following the terminology of Burchard and Hofmeister (2008),  $\Phi_{Sx}$  and  $\Phi_{Sy}$  are the mean-straining terms (straining of the depth-average buoyancy gradient) in along- and across-channel directions, respectively, with  $\partial_x \langle b \rangle_z$  and  $\partial_y \langle b \rangle_z$  being the gradients of the depth averaged buoyancy and  $\tilde{u}$  and  $\tilde{v}$  are the deviation of the along- and across-channel velocity from their vertical means. The lateral non-mean straining term is labeled with  $\Phi_{nSy}$ , where  $\partial_y \tilde{b}$  denotes the lateral gradient of the deviation of the buoyancy from its vertical mean. A theoretical discussion of the behavior of the certain terms appearing in 5.5 can be found in Burchard and Hofmeister (2008).

The final contribution to (5.5) is the vertical mixing term,  $\Phi_{mix}$ , which is proportional to the depth-mean of the turbulent buoyancy flux,  $\langle w'b' \rangle$ . It is difficult to estimate  $\langle w'b' \rangle$ , since turbulent quantities are usually hard to access via field observations. With the eddy-viscosity principle it can be re-expressed as,

$$\langle w'b' \rangle = -\nu_t^b N^2 \quad , \quad (5.6)$$

where we introduced the turbulent diffusivity of buoyancy,  $\nu_t^b$ , and the buoyancy frequency,  $N^2 = \partial_z b$ .  $N^2$  can be calculated from CTD-data, but the problem is to find a proper expression for  $\nu_t^b$ . Here we make use of the length scale approach (see e.g. Umlauf and Burchard (2003, 2005); Scully et al. (2011)),

$$\nu_t^b = \frac{1}{Pr_t} u_* L_t \quad , \quad (5.7)$$

with the turbulent Prandtl number,  $Pr_t$ , and a turbulent length scale,  $L_t$ . The turbulent velocity scale is identified here with the friction velocity,  $u_*$ , assuming that the major source of turbulence is bottom friction. For unstratified flows we consider the well-known parabolic profile for the turbulent length scale,

$$L_p = \kappa \frac{\eta - z}{D} (z + H) \quad , \quad (5.8)$$

where  $\kappa = 0.41$  denotes the Karman constant. In order to take stratification into account Munk and Anderson (1948) suggest a modification of the turbulent length scale proportional to the bulk Richardson number,

$$Ri_b = \frac{D}{2} \frac{\Delta_z b}{(\Delta_z u)^2} \quad , \quad (5.9)$$

where  $\Delta_z b$  and  $\Delta_z u$  are the difference of the upper and lower water column of the buoyancy and the velocity, respectively. Their parametrization yields for the turbulent diffusivity

$$L_{MA} = \kappa \frac{\eta - z}{D} (z + H) \left( 1 + \frac{10}{3} Ri_b \right)^{-\frac{3}{2}} \quad . \quad (5.10)$$

An alternative approach of considering stratification is to limit (5.8) by the Ozmidov length,

$$L_{Oz} = \sqrt{\frac{\varepsilon}{N^3}} \quad , \quad (5.11)$$

which is usually associated with the size of the largest vertical eddies (Dillon, 1982). If we further assume a turbulent Prandtl number of approximately  $Pr_t \approx 1$ , we obtain a turbulent buoyancy flux of

$$\langle w'b' \rangle = -u_* \min(L_p, L_{Oz}) N^2 . \quad (5.12)$$

Scully et al. (2011) recently demonstrated that a mixture of boundary and Ozmidov length scale limiter provides a sufficiently well turbulence model for most estuarine conditions.

### 5.3.2. Framework for along- and across-channel circulation

#### General Concept

In former studies (e.g. Kalkwijk and Booij (1986); Geyer (1993); Lacy and Monismith (2001); Chant (2002); Kim and Voulgaris (2008); Nidzieko et al. (2009)) studying lateral circulation associated with curvature the authors used the lateral momentum balance for curved coordinates based on Kalkwijk and Booij (1986). Kalkwijk and Booij (1986) originally used a simplified balance in order to derive an analytical solution for a curved channel in a stationary equilibrium. Here we follow a slightly different approach, where we use the momentum balance for a curved channel system (see e.g. Huijts et al. (2009)) to derive transport equations for the bulk along- and across-channel vorticity, which provide a more consistent and straight forward measure for lateral and longitudinal circulation, respectively. This approach has the advantage to deliver an easy and consistent framework to study the generation and interplay of lateral and longitudinal circulation simultaneously, where the tidal average of the latter can be interpreted as estuarine circulation. Thus the following framework provides a direct link between lateral circulation and estuarine exchange flow.

To quantify lateral circulation, we use the  $x$ -component of the vorticity,

$$\omega_x = \partial_y w - \partial_z v \approx -\partial_z v , \quad (5.13)$$

where we assume the vertical shear of the lateral velocity to be much larger than the lateral shear of the vertical velocity (see e.g. Collignon and Stacey (2012)). In a similar manner we can identify the  $y$ -component of the vorticity as the along-channel or longitudinal circulation,

$$\omega_y = \partial_z u - \partial_x w \approx \partial_z u . \quad (5.14)$$

#### Transport equations

In order to obtain bulk values for  $\omega_x$  and  $\omega_y$ , we separate each water column in a upper surface- (SL) and a lower bottom-layer (BL), above and below  $z = 0.5(\eta - H)$ , respectively, and average all data on those layers. The Reynolds-averaged hydrostatic momentum equations in curved-coordinates (to take channel curvature into account, see Kalkwijk

and Booij (1986); Huijts et al. (2009)) for such a layer reads as,

$$\begin{aligned} \partial_t \langle u \rangle_L &= -\langle u \partial_x u \rangle_L - \langle v \partial_y u \rangle_L - \langle w \partial_z u \rangle_L + f \langle v \rangle_L - \frac{\langle u \rangle_L \langle v \rangle_L}{R} \\ &\quad - g \partial_x \eta + \frac{1}{a-b} \int_b^a \int_z^\eta \partial_x b \, dz' \, dz - \frac{1}{a-b} \langle u' w' \rangle \Big|_b^a, \end{aligned} \quad (5.15)$$

$$\begin{aligned} \partial_t \langle v \rangle_L &= -\langle u \partial_x v \rangle_L - \langle v \partial_y v \rangle_L - \langle w \partial_z v \rangle_L - f \langle u \rangle_L + \frac{\langle u \rangle_L^2}{R} \\ &\quad - g \partial_y \eta + \frac{1}{a-b} \int_b^a \int_z^\eta \partial_y b \, dz' \, dz - \frac{1}{a-b} \langle v' w' \rangle \Big|_b^a, \end{aligned}$$

where  $R$  denotes the radius of channel curvature,  $a$  and  $b$  the upper and lower limit of the layer, and  $\langle \cdot \rangle_L$  the layer average. In (5.15) molecular and horizontal mixing is ignored.

We define the bulk along-channel vorticity,  $[\omega_x]$ , as the difference in the across-channel velocity component between the upper and lower layer divided by half of the total water depth,  $D$ ,

$$[\omega_x] = -[\partial_z v] = -\frac{2}{D} (\langle v \rangle_{SL} - \langle v \rangle_{BL}), \quad (5.16)$$

and, by analogy, the bulk across-channel vorticity,

$$[\omega_y] = [\partial_z u] = \frac{2}{D} (\langle u \rangle_{SL} - \langle u \rangle_{BL}). \quad (5.17)$$

By combining (5.15), (5.16) and (5.17) it is possible to derive a simplified transport equation for the bulk along-channel vorticity,

$$\begin{aligned} \partial_t [\omega_x] &= \partial_y \langle b \rangle_z + \overbrace{f [\omega_y]}^{\omega_x^f} - \overbrace{\frac{2}{R} \langle u \rangle_z [\omega_y]}^{\omega_x^{curv}} \\ &\quad - \overbrace{\frac{8}{D^2} \langle v' w' \rangle \Big|_{\frac{1}{2}(\eta-H)}}^{\omega_x^{mix_i}} + \overbrace{\frac{4}{D^2} \langle v' w' \rangle \Big|_{-H}}^{\omega_x^{mix_b}}, \end{aligned} \quad (5.18)$$

and the bulk across-channel vorticity,

$$\begin{aligned} \partial_t [\omega_y] &= -\partial_x \langle b \rangle_z - \overbrace{f [\omega_x]}^{\omega_y^f} + \overbrace{\frac{1}{R} \langle u \rangle_z [\omega_x]}^{\omega_y^{curv}} + \overbrace{\partial_y \langle u \rangle_z [\omega_x]}^{\omega_y^{LC}} \\ &\quad + \overbrace{\frac{8}{D^2} \langle u' w' \rangle \Big|_{\frac{1}{2}(\eta-H)}}^{\omega_y^{mix_i}} - \overbrace{\frac{4}{D^2} \langle u' w' \rangle \Big|_{-H}}^{\omega_y^{mix_b}}. \end{aligned} \quad (5.19)$$

The along- and across-channel vorticity have similar forcing terms: baroclinic pressure gradients,  $\partial_x \langle b \rangle_z$  and  $\partial_x \langle b \rangle_z$ , and a transformation (exchange) of the different vorticity

components into each other, controlled by Coriolis forcing,  $\omega_x^f$  and  $\omega_y^f$ , and centrifugal forcing,  $\omega_x^{curv}$  and  $\omega_y^{curv}$ , respectively. Furthermore, equations (5.18) and (5.19) both have similar bottom,  $\omega_x^{mix_b}$  and  $\omega_y^{mix_b}$ , and internal friction terms,  $\omega_x^{mix_i}$  and  $\omega_y^{mix_i}$ . Equation (5.19) additionally contains a term associated with the lateral redistribution of along-channel momentum,  $\omega_y^{LC}$ , which is known to be an important process in terms of the generation of estuarine circulation in many systems (e.g. Lerczak and Geyer (2004); Scully et al. (2009); Burchard et al. (2011)).

In order to derive the equations (5.18) and (5.19) we make several assumptions. For simplicity we assumed  $\partial_y b$  and  $\partial_x b$  to be vertically constant and  $\langle v \rangle_z = 0$ , we neglected the surface momentum flux, the along-channel gradient of  $u$  and  $v$  ( $\partial_x v = \partial_x u = 0$ ), and the vertical advection terms in (5.15). Thus, the only advection term of (5.15) taken into account is the across-channel advection of the  $u$ -component, which for simplicity is assumed to be  $-\langle v \partial_y u \rangle_L \approx -\langle v \rangle_L \partial_y \langle u \rangle_L$ .

### Friction parametrization

To estimate the internal friction terms in (5.18) and (5.19), a down-gradient approach for the turbulent momentum fluxes is applied, similar to (5.6),

$$\langle u'w' \rangle = -\nu_t \partial_z u \quad \langle v'w' \rangle = -\nu_t \partial_z v, \quad (5.20)$$

where  $\nu_t$  is the turbulent viscosity. By making use of (5.16) and (5.17) we obtain

$$\omega_x^{mix_i} = -\frac{8}{D^2} \nu_t^i [\omega_x] \quad \omega_y^{mix_i} = -\frac{8}{D^2} \nu_t^i [\omega_y], \quad (5.21)$$

where  $\nu_t^i$  denotes the characteristic turbulent viscosity at the interface between the upper and lower layers that is calculated by a length scale approach with an Ozmidov-limiter (see also discussion for equation (5.12)),

$$\nu_t^i = u_* \min \left\{ L_p(z) \Big|_{z=-\frac{1}{2}D}; \min_{-\frac{3}{4}D < z < -\frac{1}{4}D} \{L_{Oz}(z)\} \right\}. \quad (5.22)$$

Since  $\nu_t^i$  represents a bulk viscosity for the momentum flux between the upper and lower layers, we take the minimum value of the Ozmidov length found in the middle of the water column ( $z = -\frac{3}{4}D \dots -\frac{1}{4}D$ ) and compare it to the maximum value of  $L_p$  found at the interface between the upper and lower layers ( $z = -D/2$ ). This procedure accounts for the fact that the bulk momentum exchange between the two layers is restricted by the smallest values of  $\nu_t$  in a given spatial range than by an average value.

The bottom friction terms,  $\omega_x^{mix_b}$  and  $\omega_y^{mix_b}$ , are calculated based on the friction velocities measured with the micro-structure profiler (see Section 5.2.4),

$$\omega_x^{mix_b} = -\frac{4}{D^2} u_*^2 \sin(\alpha_{u_{bl}}) \quad \omega_y^{mix_b} = \frac{4}{D^2} u_*^2 \cos(\alpha_{u_{bl}}), \quad (5.23)$$

where we used  $\langle u'w' \rangle \Big|_{-H} = -|u_*|u_*^x$  and  $\langle v'w' \rangle \Big|_{-H} = -|u_*|u_*^y$ , with  $u_*^x = |u_*| \cos(\alpha_{u_{bl}})$  and  $u_*^y = |u_*| \sin(\alpha_{u_{bl}})$  being the  $x$ - and  $y$ -component of the friction velocity, and  $\alpha_{u_{bl}}$  denoting the angle of the velocity vector in the bottom layer with respect to the  $x$ -axis.

### Non-dimensional Numbers

It is useful to define non-dimensional numbers in order to relate the various production terms in (5.18) for the lateral circulation.

Geyer (1993) suggested the curvature Rossby number,

$$Ro_c = \frac{2u_A}{fR}, \quad (5.24)$$

in order to relate Coriolis and centrifugal acceleration, where  $u_A$  denotes the amplitude of the along-channel tidal currents. The curvature Rossby number corresponds to the ratio of  $\omega_x^{curv}$  and  $\omega_x^f$  of equation (5.18).

Another useful number would be the ratio between buoyancy and curvature acceleration. To derive such a number it is necessary to provide a proper scaling for the bulk along-channel vorticity (5.14). In well-mixed conditions we can assume that the bulk across-channel vorticity scales approximately with the vertical shear of the law-of-the-wall, which is proportional to  $u_*$ , in the middle of the water-column,

$$[\omega_y] \approx \partial_z u \Big|_{\frac{1}{2}(\eta-H)} \approx \frac{u_*}{\kappa(z-H)} \Big|_{\frac{1}{2}(\eta-H)} = \frac{2u_*}{\kappa D}. \quad (5.25)$$

Making use of equation (5.25) and (5.18) it is possible to define the curvature Simpson number,

$$Si_r = \left\langle \frac{|\partial_y \langle b \rangle_z|}{|\omega_x^{curv}|} \right\rangle_{M_2} \approx \left\langle \frac{|\partial_y \langle b \rangle_z|}{\left| \frac{2}{R} \langle u \rangle_z \frac{2u_*}{\kappa D} \right|} \right\rangle_{M_2} \approx \frac{\kappa DR}{4\sqrt{C_d}} \frac{\langle |\partial_y \langle b \rangle_z| \rangle_{M_2}}{u_A^2}, \quad (5.26)$$

as the average ratio between the strength of buoyancy and curvature forcing of lateral circulation.  $Si_r$  provides a bulk number to determine the relative influence of buoyancy and curvature forcing on the generation of lateral circulation.

If we assume the mixing terms in equation (5.18) to scale approximately with  $u_*^2/D^2$  it is possible to identify the ratio between mixing and curvature forcing as the non-dimensional radius of curvature,

$$\hat{R} = \frac{u_*^2}{\omega_x^{curv} D^2} = \frac{u_* R \kappa}{4 \langle u \rangle_z D} = \frac{\sqrt{C_d} \kappa R}{4 D}. \quad (5.27)$$

In the last step we made use of the relation  $u_*^2 = C_d \langle u \rangle_z^2$ , with the non-dimensional drag coefficient  $C_d \approx 3 \cdot 10^{-3}$ , and the scaling (5.25). It is interesting to note that the ratio between curvature forcing and mixing, is in the first order simply determined by the ratio between the radius of curvature and the water depth, independent of the velocity. Thus a small  $\hat{R}$  can be interpreted as a rough criterion that curvature induced lateral circulation is able to overcome vertical mixing, in well-mixed systems.

Finally we introduce the instantaneous lateral Simpson number,

$$Si_y = \frac{|\partial_y \langle b \rangle_z| D^2}{u_*^2}, \quad (5.28)$$

in order to relate lateral baroclinic pressure forcing and mixing. Note that in contrast to  $\hat{R}$  and  $Si_r$ , the lateral Simpson number,  $Si_y$ , is defined to be time dependent here.



## 5.4. Observations

### 5.4.1. General conditions

The entire campaign lasted about two weeks and was divided into two separate measurement periods, period  $S$  for station measurements and period  $Tr$  for transect measurements (see gray-shaded background in Figure 5.2).

During the first period  $S$ , there were moderate winds between 3 to 7 m s<sup>-1</sup> with direction varying from southwest to northwest (Figure 5.2a). At day 133 the wind speed increased substantially, which made it necessary to interrupt the measurements. During that storm event, which lasted from day 133 until 136, the average wind speed was larger than 10 m s<sup>-1</sup>, coming from the West. Afterwards during period  $Tr$ , the wind became moderate again with about 5 m s<sup>-1</sup> from south-west.

The water elevation and tidal velocities are dominated by the  $M_2$ -tide, with a slight modification caused by a  $M_4$ -resonance (Stanev et al., 2003). There are no large differences between neap and spring tide. The sea level has an amplitude of about 1.3 m, slightly increasing during the campaign. The depth averaged along-channel velocity at station  $A$  (see map 5.1) varies between 1 m s<sup>-1</sup> during flood and 1.3 m s<sup>-1</sup> during ebb, indicating a slight ebb-dominance at station  $A$  (Figure 5.2b).

During the measurement period  $S$ , a positive along-channel buoyancy gradient between 2 and 4 · 10<sup>-7</sup> s<sup>-2</sup> is observed (see Figure 5.2d), meaning that the Wadden Sea water is less dense than the water of the open North Sea. During that period the density gradient is entirely dominated by temperature (see Figure 5.2c), with the Wadden Sea water being about 4°C warmer than the North Sea. Salinity is slightly compensating, since there is a small opposing salinity gradient (positive into the estuary).

Due to the storm event the situation changed substantially. At station  $A$  the average salinity decreased by approximately 1 g kg<sup>-1</sup>. At the same time the temperature gradient between the Wadden and North Seas vanished (see Figure 5.2c), which yielded the extraordinary situation of an inverse or negative buoyancy gradient (see Figure 5.2c) during that storm event. This rather unusual situation (Burchard et al., 2008) of an inverse salinity gradient (for the spring), was caused by an extraordinary warm and dry period before the campaign, with two months of almost no rain-fall. The associated differential heating and evaporation led to the strong positive temperature gradient as well as the small opposing salinity gradient.

After the storm during the consecutive measurement period  $Tr$ , which is the major subject of this paper, the buoyancy gradient,  $\partial_x \langle b \rangle_z$ , slowly recovered back to usual spring conditions (see Burchard et al. (2008)). In contrast to period  $S$ , density is now controlled by salinity and temperature in comparable magnitudes, both supporting a positive along-channel buoyancy gradient. Note that at the beginning of period  $Tr$ , the density gradients were still weak, which has strong dynamical implications as will be shown below.

### 5.4.2. Tidal variation of stratification

Figure 5.3a shows the cross-transect distribution of the depth-mean density in time,  $\langle \sigma \rangle_z$ . Generally it increases during flood and decreases during ebb indicating a persistent along-channel density gradient,  $\partial_x \rho$ , with North Sea water being generally denser than Wadden

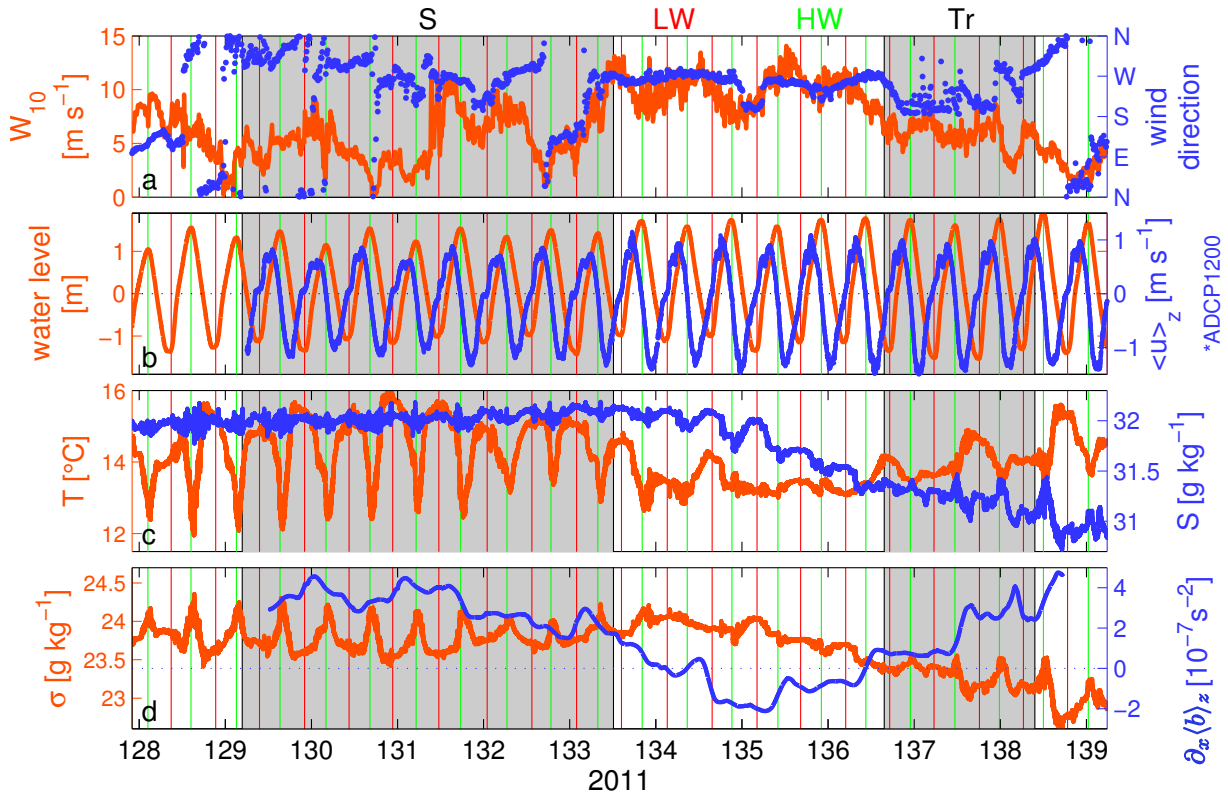


Figure 5.2.: Conditions during the campaign between May 9 (day128) and May 20 (day 139) 2011. Panel (a) shows the wind conditions, with the wind speed in red and the wind direction in blue. The water-level and the depth-mean velocity are displayed in panel (b) in red and blue, respectively. Temperature (blue) and salinity (red) at station *A* are shown in panel (c). The scales for both, temperature and salinity are chosen in such a way that they correspond to a similar change in density in order to make both curves comparable to each other. Panel (d) pictures the resulting density in red and the along-channel buoyancy gradient in blue (see Section 5.2.4 for its calculation). The gray-shaded back ground labeled with *S* and *Tr* marks the two measurement periods and the vertical red and green lines the times of low and high water, respectively.

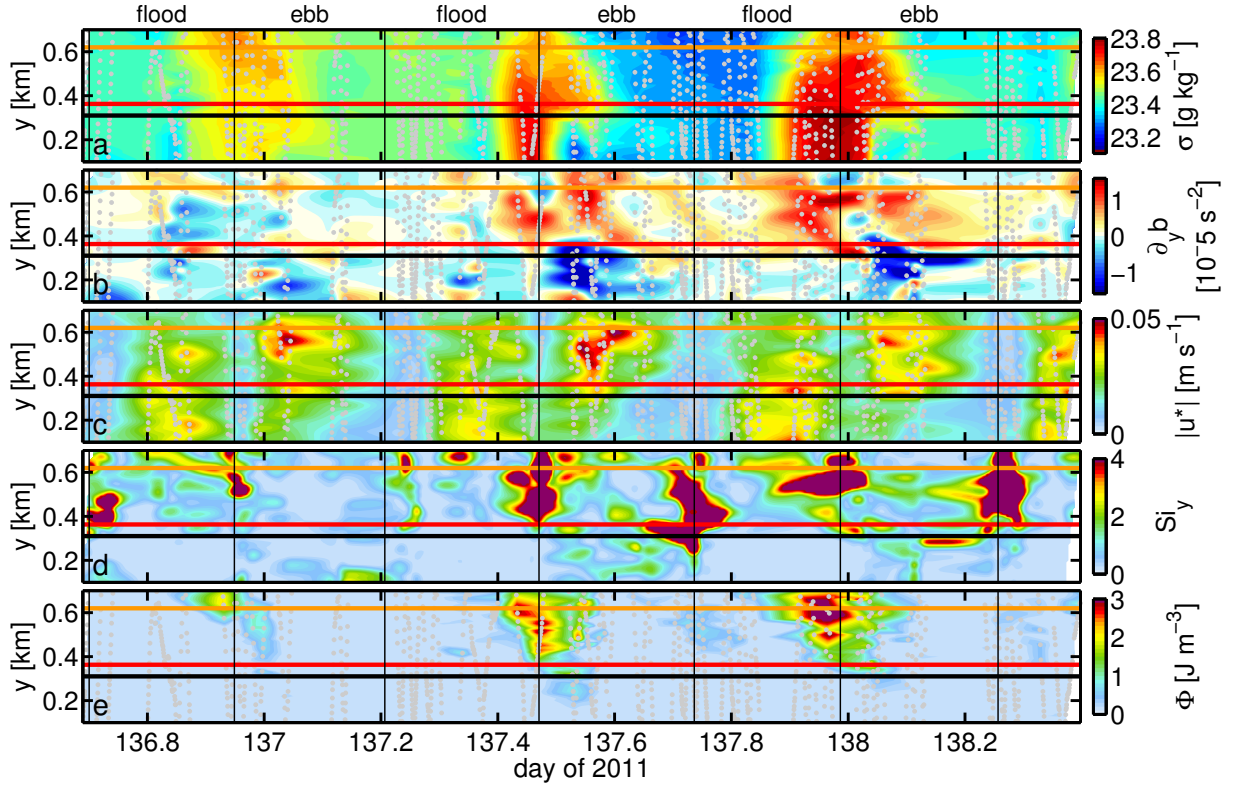


Figure 5.3.: Temporal evolution of the across-channel distribution of (a) the depth-averaged density  $\langle \sigma \rangle_z = \langle \rho \rangle_z - \rho_0$  [ $\text{kg m}^{-3}$ ], (b) the lateral density gradient, (c) the friction velocity, (d) the lateral Simpson number (5.28), and (e) the potential density anomaly, defined in (5.4). The orange and the red line mark the relative positions of the ADCPs, A and S, respectively (see Figure 5.1). The black line marks the edge of the shoal. Below that line the average water depth is relatively shallow with about 6 m whereas the channel above that line is more than 10 m deep in average. The grey dots indicate the position of the MSS profiles used to obtain the gridded field.

Sea water. The difference between high-water (HW) and low-water (LW) increases during the observed period suggesting an associated increase in  $\partial_x \rho$  (see also Figure 5.2d). As discussed before, during the observed period the density difference between East Sea and Wadden Sea is recovering from an inverse situation during the strong wind event (see Figure 5.2a) back to a typical situation with a positive buoyancy gradient towards the coast.

Besides this general temporal behavior a strong cross-channel variability of the density can be seen. It is worth distinguishing between the density evolution in the deep channel above the black line and those of the shoal underneath. Focusing on the deep channel first, we find that during the second and third flood the density in the southern part of the channel increases faster than in the northern part, yielding a significant positive across-channel buoyancy gradient (see Figure 5.3b). On the other hand during ebb the decrease is much faster in the northern part than in the southern part leading to an even stronger positive lateral buoyancy gradient. During the first flood of the observed period the picture looks slightly different, most likely due to the fact that the overall horizontal density gradients were much weaker or even reversed.

The density increase on the shoal during flood is laterally more homogeneous with no large gradients evolving, but interestingly it increases faster on the shoal than in the channel although it is more shallow and one would expect the along-channel current to be slower due to bottom friction. Most likely this effect is due to channel curvature, where the flood current is deflected to the southern part of the channel. This effect yields a significantly larger density on the shoal than in the channel during high water (HW). Conversely, during ebb the density on the shoal rapidly decreases so that it becomes much less dense than in the channel already during early ebb phase.

The lateral buoyancy gradient (see Figure 5.3b) is mainly positive in the channel and negative on the shoal at late flood and high ebb, where the strongest gradients can be found. Around HW the pattern is much more complex with  $\partial_y \langle b \rangle_z$  changing sign several times along the transect. At low water no significant lateral buoyancy gradients can be observed. Note that the gradient over the shoal is calculated slightly differently than in the channel, taking into account only the first 6 m of the water column for calculating the vertical means of the density, whereas for the channel calculations the upper 10 m have been used.

Figure 5.3c shows the friction velocity (5.3) mirroring the production of turbulence due to tidal currents and thus the strength of the tidal velocities as well. A clear asymmetry between flood and ebb can be observed. The flood currents are strongest over the shoal on the southern side of the transect, whereas the ebb currents dominate in the northern part of the channel. This phenomenon could be due to channel curvature where the ebb current is deflected to the north and the flood current to the south, due to the *S*-shaped curve of the channel (see Figure 5.1). Hence, the deeper northern part of the channel appears to be dominated by ebb whereas the shallower southern part is dominated by flood.

The evolution of the instantaneous lateral Simpson number,  $Si_y$  (see equation (5.28)), is shown in Figure 5.3d. Most of the time the lateral Simpson number is below unity, indicating that tidal mixing is mostly dominating over the tendency of the lateral buoyancy gradient to vertically stratify the water column. The largest values of  $Si_y$  are found

around slack tide mainly due to the significant drop in  $u_*$  (see Figure 5.3c). However, note that relatively large values can also be found towards the end of flood in the channel, although the friction velocities are still large. Here the Simpson number is controlled by the relatively large lateral buoyancy gradient.

Now we concentrate on the potential energy anomaly as a vertically integrated measure of vertical stratification (see equation (5.4)), which is displayed in Figure 5.3e. Most of the time  $\Phi$  is very small indicating that the water column is well mixed during long periods of the tidal cycle, but there are also times where we find significant stratification with values of  $\Phi$  up to  $3 \text{ J m}^{-3}$  and more. These relatively strong stratification events frequently occur around high water, and are more pronounced towards the northern part of the channel. Each tidal cycle the  $\Phi$ -peak becomes stronger, mirroring the horizontal density gradient increases during the observed period. Interestingly,  $\Phi$  seems to peak far before slack tide, beginning at full flood and reaching its maximum values by the end of the flood. This is particularly true for the northern part of the channel, where we find large values of the potential energy anomaly at times that are still characterized by relatively large values of  $u_*$  (compare Figure 5.3c). Also the lateral Simpson number,  $Si_y$ , is large here due to a strong lateral buoyancy gradient, indicating that the internal cross-channel pressure gradient is stronger than vertical mixing and thus able to generate significant stratification. On the other hand at slack around low water no significant stratification can be found although the lateral Simpson numbers are far above one here. It seems as if large lateral Simpson numbers only occur together with significant stratification if they are associated with large lateral buoyancy gradients as well (see Figure 5.3e).

### 5.4.3. Tidal velocities

#### Along-channel velocity $u$ and its lateral shear

Figure 5.4a,b shows the along-channel velocity,  $u$ , for the northern station  $A$  and the southern station  $S$ , respectively. Both have in common that the transition from flood to ebb (high water slack) is significantly shorter than low-water slack. This is a well known phenomenon, associated with the characteristic phase and amplitude relation of the  $M_2$  and  $M_4$  tide for basins as in the Wadden Sea with large tidal flats and narrow channels in between (Stanev et al., 2003; Boon and Byrne, 1981; Friedrichs and Aubrey, 1988).

When concentrating on the northern station (Figure 5.4a) it is interesting to note that the flood currents (red) are smaller than the ebb currents (blue), where as in the southern station (Figure 5.4b) the opposite is true. This asymmetric difference is also mirrored in the across-channel shear of the along-channel velocity, shown in Figure 5.5. It is calculated by taking the difference between the depth-averaged along-channel velocity of both stations and dividing it by their effective distance when projected on the channel normal transect  $Tr$  (see Figure 5.1). Except for low water slack  $\partial_y \langle u \rangle_z$  is below zero at all times with values around  $-10^{-3} \text{ s}^{-1}$  during flood and even smaller values during ebb down to  $-2 \cdot 10^{-3} \text{ s}^{-1}$ , corresponding to larger ebb-currents towards the north of the channel and larger flood-currents towards the south. This phenomenon is most likely due to the curvature of the channel, which has an  $S$ -shape at the measurement location (see Figure 5.1), meaning that the flood currents experience a negative (counter-clockwise) and the ebb currents a positive (clockwise) radius of curvature,  $R$ . The centrifugal force

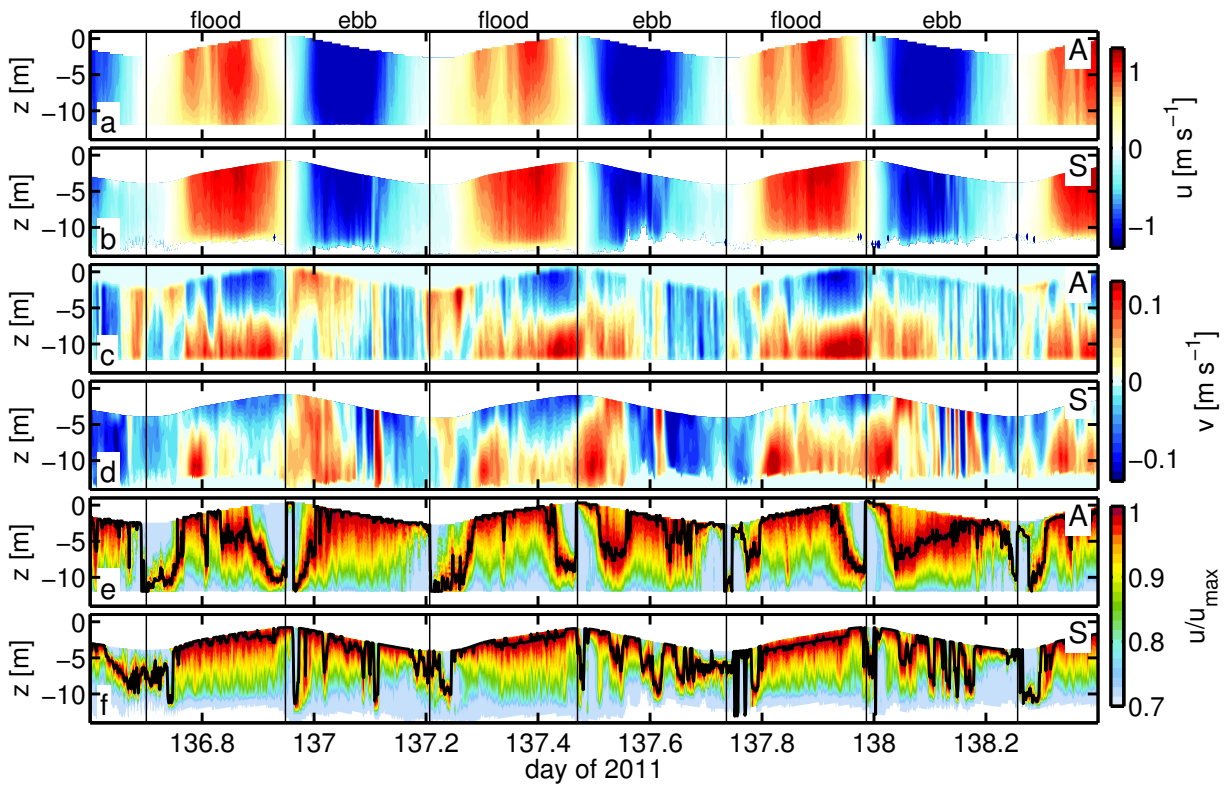


Figure 5.4.: Data of the two moored ADCPs (see Figure 5.1). The label in the upper right corner of each panel indicates whether the data belong to **A** the up-ward looking bottom mounted or **S** the vessel mounted down-ward looking ADCP. Panels a and b show the along-channel component of the velocity  $u$  and c and d show the across-channel component  $v$ . Panels e and f display the longitudinal velocity normalized with the maximum speed of each water column, respectively. The black line in panel e and f illustrates the height of the velocity maximum.

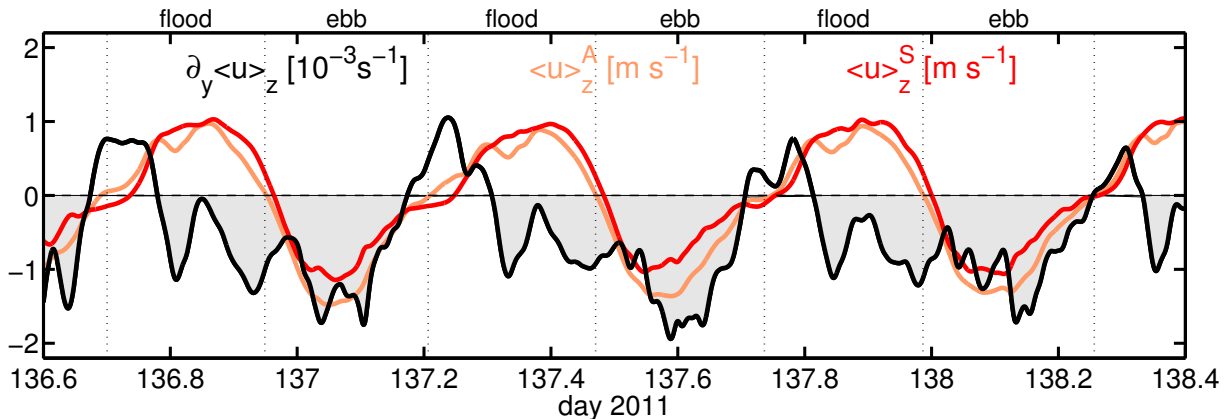


Figure 5.5.: The lateral (across-channel) shear of the along-channel velocity in black, calculated as the difference between the depth mean velocity in along-channel direction of station *A* (orange) and *S* (red) divided by their relative distance on the transect projection.

deflects the larger flood velocities to the south and the ebb velocities to the north of the channel, respectively.

### Lateral Circulation

When looking at the across-channel velocity component,  $v$ , (Figure 5.4c,d) we find a strong exchange circulation. At the northern station (Figure 5.4c) this secondary circulation is strongest during flood, peaking towards the end of flood. Note that this peak coincides with the occurrence of the peak in vertical stratification at the northern side of the channel (Figure 5.3e). At the first observed flood period  $\partial_z v$  is negative, meaning that the water close to the surface moves to the south whereas the water close to bottom is moving to the north. During the beginning of the consecutive ebb the circulation is slightly reversed and breaks down completely towards low water slack.

In the subsequent two tidal cycles the strong lateral circulation during flood is more pronounced and keeps its sign even during high water and the beginning of ebb, but most of ebb no significant lateral exchange flow can be found. The fact that the lateral circulation during flood becomes stronger with proceeding time during the observed period and is later not changing sign anymore during ebb might be associated with the increase of the horizontal density gradients during that period (see Figure 5.2d).

If we compare the northern station *A* (Figure 5.4c) to the southern station *S* (Figure 5.4d) we find a similar behavior at both stations. Although slightly weaker at *S* the secondary circulation has the same orientation at both stations most of the time. This implies that there is a one-cell lateral circulation in the channel, usually known to be associated with curvature or Coriolis force, rather than a two-cell circulation induced by differential transport due to friction. The latter leads to the well-known convergence zones at the surface in the middle of the channel during flood (Nunes and Simpson, 1985), which do not occur for the one-cell circulation.

### Vertical shear of the along-channel velocity

Figure 5.4e,f shows the along-channel velocity normalized for each water column by its maximum value,  $|u|(|u|_{max})^{-1}$  for both stations respectively. This quantity provides an indicator how well momentum is mixed vertically in the water-column.

At the southern station we find the velocity maxima (black line in Figure 5.4f) close to the surface most of the time. During flood relatively large velocities ( $> 90\%$ ) occur even close to the bottom, indicating that momentum is vertically well mixed, in contrast to ebb where relatively large velocities are found just close to the velocity-maxima. The resulting asymmetry of flood- and ebb-velocity profiles are a well-known phenomenon and usually associated with *tidal straining* (Jay and Musiak, 1994; Flöser et al., 2011; Becherer et al., 2011).

The situation at the northern station *A* appears to be more complicated than the picture of classical tidal straining. During maximum flood currents we find a surface maximum with a relatively well-mixed water column similar to station *S*, but towards the end of flood the maximum flood velocities are found close to the bottom, indicating that the surface layer is de-accelerated much faster than the bottom. Most of the time during ebb tide we find a clear sub-surface velocity maximum, yielding significantly less vertically stratified velocity profiles than at the southern station. This sub-surface velocity maximum might be related to the deceleration of surface water due to low-momentum water from the shoal advected laterally into the channel. To predict the impact of that rather complicated velocity structure on along-channel estuarine circulation is not as straight forward as for the classical situation. Never the less an attempt to do so will be made in section 5.5.3

## 5.5. Mechanisms (Discussion)

In this section we relate the strong lateral circulation during flood to the occurrence of late flood stratification especially in the northern part of the channel. Furthermore the processes yielding lateral circulation in the channel will be discussed with a special focus on the asymmetry between flood and ebb. In addition the impact of the secondary circulation on along-channel estuarine exchange flow is investigated, to finally draw a general picture of the relation of all those processes and a brief discussion on the importance for similar sites.

### 5.5.1. Generation of vertical stratification

Although the occurrence of large values of the potential energy anomaly,  $\Phi$ , during full flood (Figure 5.3e) associated with strong lateral buoyancy gradients (Figure 5.3b) and thus large lateral Simpson numbers,  $Si_y$  (Figure 5.3d), suggests that lateral exchange might be causing this stratification it also shows that a simple analysis of  $Si_y$ -thresholds can not be sufficient since no significant stratification is found around LW despite large lateral Simpson numbers. Therefore it seems necessary to provide a more sophisticated analysis of the balance of  $\Phi$ , to clarify its generation.



### Late flood stratification at station A

We focus our investigation on the northern station A, where strong stratification appears during flood (see Figure 5.3e). The occurrence of such late flood stratification is surprising at first glance, since former studies suggested that classical tidal straining might be in control of vertical stratification in the Wadden Sea (Becherer et al., 2011; Burchard et al., 2011; Flöser et al., 2011). If that were the case, we would expect well mixed conditions during flood and stratified conditions during ebb currents (Simpson et al., 1990), but since we find strongest stratification during strong flood current, another mechanism must be responsible for its generation. Lacy et al. (2003) found under comparable conditions in San Francisco Bay lateral circulation causing significant flood stratification. (see also Scully and Geyer (2012)).

To analyse the terms in equation (5.5) we use the gridded density and turbulence data partly shown in Figure 5.3 and the corresponding velocity data from the ADCP moored at station A (see Figure 5.1) both interpolated on the same time basis.

Figure 5.6 shows the evolution of each of the terms of equation (5.5) at station A. It becomes obvious from Figure 5.6a that the advection terms,  $\Phi_A$  (orange line), are of minor importance, since they are much smaller than the rate of change (black line). It might be that the along-channel advection term is more important than those we calculated, but it can not be estimated with the available data set.

The along-channel straining,  $\Phi_{Sx}$ , (light blue line in Figure 5.6b) shows the characteristic behavior associated with *classical* tidal straining. It de-stratifies (negative values) the water column during flood and stratifies (positive values) it during ebb. Nevertheless, it appears to be much smaller than lateral straining,  $\Phi_{Sy}$ , (blue line in Figure 5.6b) which often is more than one order of magnitude larger. Since the top to bottom differences of the along- and across-channel velocity are of comparable magnitudes this large difference is predominantly due to the lateral buoyancy gradient which is found to be much larger than the longitudinal gradient (compare Figure 5.2d and Figure 5.3b). The lateral non-mean straining term,  $\Phi_{nSy}$  (dark blue line in Figure 5.6b), is found to be smaller than the mean across-channel straining,  $\Phi_{Sy}$ , but can not be ignored in contrast to the advection,  $\Phi_A$ , and along-channel straining,  $\Phi_{Sx}$ .

In the highly energetic environment of the Wadden Sea, the mixing term,  $\Phi_{mix}$ , is found to be very large (see Figure 5.6c). With the simplest modeling approach (5.8), assuming a parabolic diffusivity profile and thus just valid for well mixed conditions,  $\Phi_{mix}$  is highly over-estimated, being much larger than all other terms. This fact demonstrates, that even under those weakly stratified conditions, stratification needs to be taken into account when modeling turbulent transport. The length scale limitation with the Ozmidov length (5.11) as well as the correction with the bulk Richardson No according to Munk and Anderson (1948) (5.10) both yield significantly less mixing. Although both approaches provide comparable magnitudes for the mixing term  $\Phi_{mix}$ , they show considerable differences in their time evolution. Therefore, we decide to use the more sophisticated method of the Ozmidov-length scale limitation,  $\Phi_{mixOz}$  (Figure 5.6c) for further analysis.

$\Phi_{Sy}$  and  $\Phi_{mix}$  are by far the largest terms in equation (5.5), suggesting that the evolution of  $\Phi$  is mainly controlled by a balance between lateral straining and vertical mixing. To test that hypothesis we integrate the sum of the lateral straining terms  $\Phi_{Sy}$  and  $\Phi_{nSy}$  and the vertical mixing term  $\Phi_{mix}$  over time and compare it to the directly measured values of

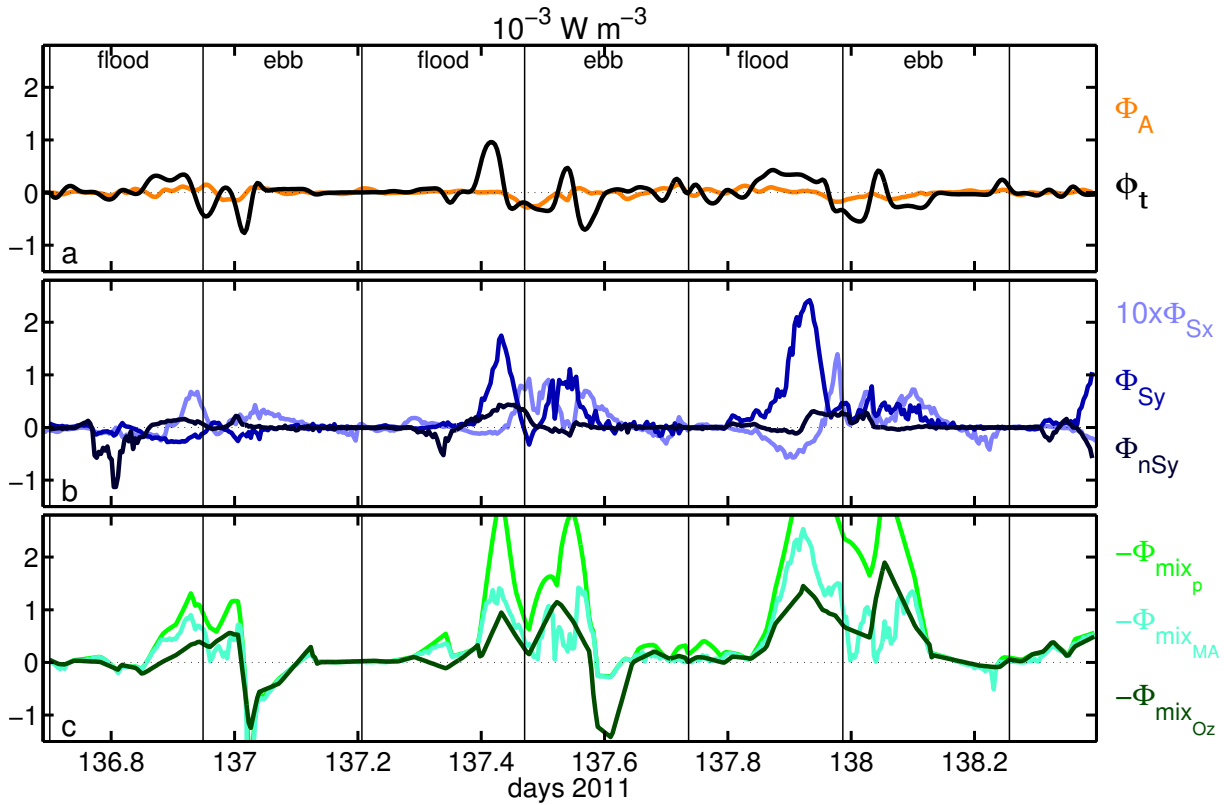


Figure 5.6.: Time evolution of the different terms of the potential energy anomaly equation (5.5). (a) shows the sum of the different advection terms in orange and the rate of change,  $\partial_t \Phi$ , in black. Panel (b) displays all straining terms that could be calculated. Note that the along-channel straining term,  $\Phi_{Sx}$  is multiplied by a factor of ten to make it visible in this scale. Finally (c) shows the vertical mixing term  $\Phi_{mix}$ , modeled with different approaches, in light green according to equation (5.8), in cyan with the Munk and Anderson (1948) parametrization (5.10), and in dark green with the Ozmidov-length limitation (5.12).

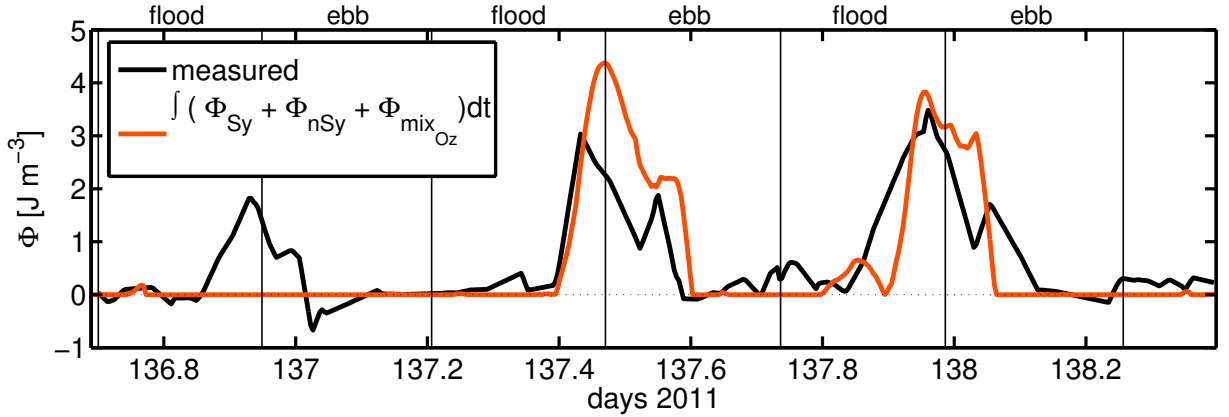


Figure 5.7.: The black line shows  $\Phi$  at station  $A$  obtained by interpolation of the data measured by the micro-structure sonde. The orange curve shows the time integral of the sum of the lateral straining terms and vertical mixing from equation (5.5) calculated for the same station.

$\Phi$  (see Figure 5.7). Note that all negative values of the integral are set to zero in the process in order to ensure that large values of  $\Phi_{mix}$  do not lead to a negative runaway stratification, which would be an artificial effect since mixing can not yield a permanently unstable stratified water column. Thus we assume an instantaneous convective adjustment, where the water column is well-mixed as soon as we obtain negative values of  $\Phi$ . This procedure is necessary, since our simple turbulence model (5.12) does not sufficiently reproduce convective mixing.

Despite all the uncertainties in the calculation of the terms in (5.5), we find a surprisingly good agreement of the integral and the measured values of  $\Phi$  (see Figure 5.7). This is especially true for the two major peaks occurring from late flood to early ebb in the second and third tidal cycle of the observation period. Both agree well in magnitude and timing with the measured  $\Phi$ , indicating that the late flood stratification is generated by lateral circulation. The fact that we are not able to capture the peak occurring during the first tidal cycle might be due to the more complicated situation with very small horizontal density gradients (compare Figure 5.2d and Figure 5.3b), with the whole inlet recovering from an inverse situation back to normal. It is likely that under those conditions other terms can become important as well like the along-channel advection of  $\Phi$  or longitudinal non-mean straining, which we were not able to estimate.

In summary we find lateral straining to be in control of vertical stratification at station  $A$ . It is well known that vertical stratification is able to enhance secondary circulation in weakly-stratified estuaries (Dyer, 1989; Geyer, 1993; Dronkers, 1996), due to the suppression of turbulent momentum flux. This yields a positive feedback loop, where strong lateral circulation leads to more vertical stratification leading to stronger lateral circulation and so forth. The analysis of the instantaneous lateral Simpson number (5.28) (see Figure 5.3d), which is basically the ratio of lateral baroclinic forcing and vertical mixing, shows that the across-channel baroclinic pressure gradient alone can not be responsible for the relaxation of the lateral buoyancy gradient  $\partial_y \langle b \rangle_z$  towards vertical stratification  $N^2$ . There must be an additional mechanism driving the lateral exchange flow. Therefore,

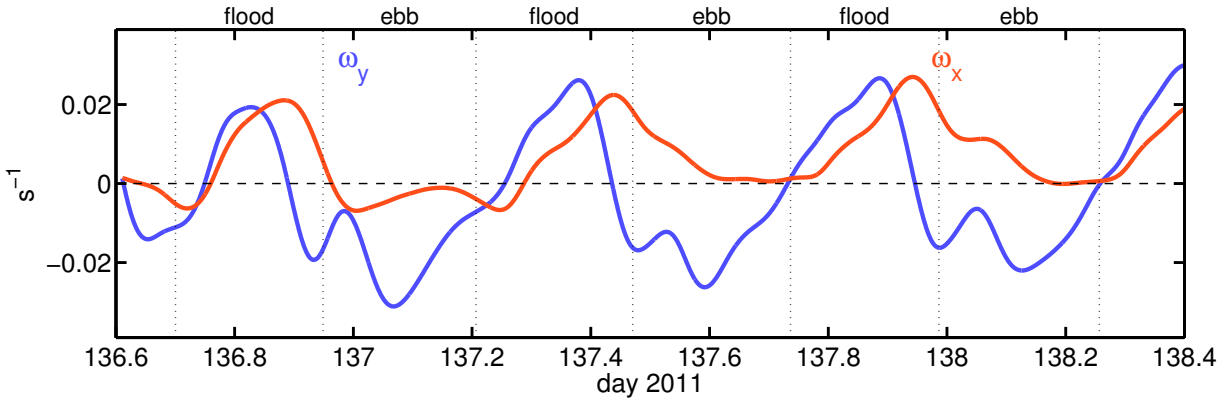


Figure 5.8.: The bulk along- and across-channel vorticity at station *A*, calculated according to equation (5.16) and (5.17), respectively.

it seems necessary to have a closer look at the generation of secondary circulation, which will be done in the next section.

## 5.5.2. Generation of lateral circulation

### Asymmetrical lateral circulation

The red curve in figure 5.8 displays the bulk lateral circulation at station *A*, based on equation (5.16). In an idealized symmetrical estuary one would expect comparable magnitudes with a change in sign of the secondary circulation between ebb- and flood-phases (Lerczak and Geyer, 2004; Burchard et al., 2011), which is obviously not the case here. With exception of the first ebb phase,  $[\omega_x]$  is always positive during the observation period, corresponding to northward velocities in the lower layer and southward velocities in the surface layer. Most of each flood period is characterized by strong lateral circulation with the largest values occurring towards the end of flood, but also during the beginning of the last two observed ebb phases positive values of the stream-wise vorticity (lateral circulation) are found. Thus the observed secondary circulation is highly asymmetrical. The reason for this asymmetry must be based on one or more asymmetries in the generation processes of  $[\omega_x]$ .

### Balance of lateral circulation

Figure 5.9 shows the different terms of equation (5.18) changing the bulk stream-wise vorticity.  $\omega_x^{mix_i}$  denotes the interfacial mixing term (light green line in Figure 5.9), that is proportional to the turbulent momentum flux in the interior. It always has the opposite sign of  $[\omega_x]$ , indicating its tendency to homogenize the water column and to destroy vertical shear. Interior mixing peaks at maximum currents, with slightly larger magnitudes during flood than ebb, associated with larger values of  $[\omega_x]$ . At high water slack  $\omega_x^{mix_i}$  rapidly decreases towards very small values, although lateral circulation is strongest here (compare Figure 5.4). This is simply due to the fact that the turbulent viscosities are very small, mainly caused by the smaller production of turbulence from the decreasing

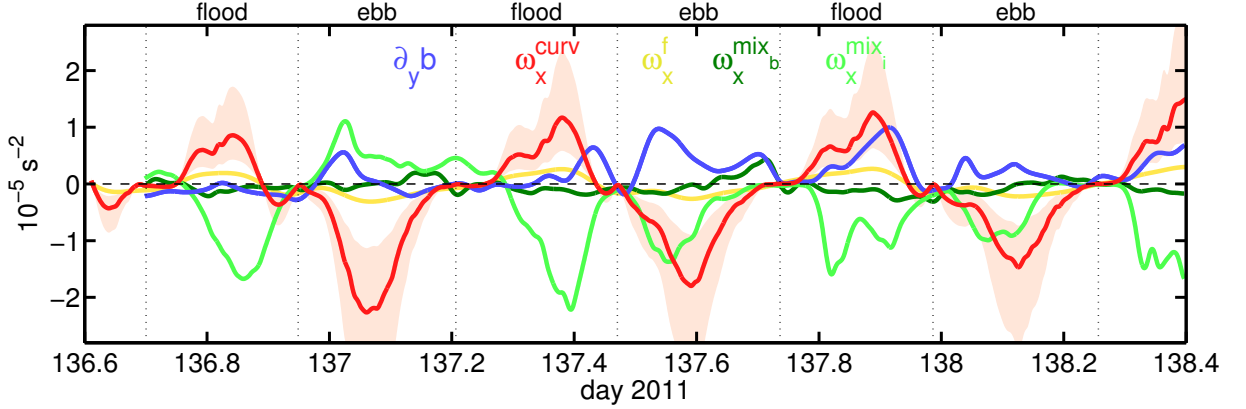


Figure 5.9.: The different terms of equation (5.18) changing lateral circulation at the northern station *A*. Light and dark green show the interfacial and bottom mixing term,  $\omega_x^{mix_i}$  and  $\omega_x^{mix_b}$ , respectively, the blue line displays the baroclinic forcing (corresponding to  $\partial_y \langle b \rangle_z$ ), and the yellow line the forcing induced by earth's rotation. The curvature deflection is shown in red, where the red line corresponds to a radius of curvature of 4 km and the pink shaded background displays a range from 2 to 8 km of curvature.

mean current and supported by the developing vertical stratification and its tendency to suppress turbulent fluxes.

Compared to interior mixing the contribution of the bottom friction term  $\omega_x^{mix_b}$  is relatively small (dark green line in Figure 5.9). Since it is proportional to the velocity in the lower water column, it usually has a tendency to decrease secondary circulation as well, given the fact that the depth averaged across-channel velocity is close to zero most of the time.

Besides those two sinks for lateral circulation three potential production terms can be identified in equation (5.18). The lateral baroclinic pressure gradient forcing,  $\partial_y \langle b \rangle_z$  (blue line in Figure 5.9), and the deflection of the vertically sheared along-channel momentum due to Coriolis force,  $\omega_x^f$  (yellow line), and due to centrifugal force,  $\omega_x^{curv}$  (red line), respectively, the latter associated with the curvature of the channel.

The buoyancy forcing (blue line in Figure 5.9) is predominantly positive. As discussed previously this is due to the fact that the lateral buoyancy gradient is mainly caused by differential advection of the along-channel gradient. The *S*-shaped curve of the channel yields negative lateral shear of the along-channel momentum most of the time (see Figure 5.5) combined with a positive along-channel buoyancy gradient this leads to a situation with decreasing density towards the northern side of the channel. At slack tide the buoyancy forcing is small. During high water this is likely caused by the relaxation of the across-channel density gradient towards vertical stratification, associated with the large values of lateral circulation (compare Figures 5.7, 5.8 and 5.9). Around low water the lateral buoyancy gradient seems to be small due to both the smaller along-channel density gradient and the decreased or even reversed lateral shear (see Figure 5.5). During late flood and early ebb values of  $\partial_y \langle b \rangle_z$  of up to  $10^{-5} \text{ s}^{-2}$  are found, which are of the same order of magnitude as interior mixing indicating that buoyancy forcing is a major

contributor to the generation of secondary circulation.

Another important player according to its magnitude is the curvature term,  $\omega_x^{curv}$  (red line Figure 5.9). It represents the deflection of along-channel momentum towards the outer bend, which affects the high momentum water near the surface stronger than the low momentum water near the bottom. The depth averaged volume transport towards the outer curve is balanced by a barotropic pressure gradient yielding a vertical exchange profile in the across-channel direction. This mechanism does not require any buoyancy forcing and thus acts in completely unstratified environments like river bends as well (Kalkwijk and Booij, 1986). In the case of station *A*,  $\omega_x^{curv}$  changes sign from positive values during flood to negative values during ebb. The product  $\langle u \rangle_z [\omega_y]_b$  (see equation (5.18)) is usually positive since both variables change sign simultaneously, hence the sign of  $\omega_x^{curv}$  is related to the sign of  $R$ , the curvature radius, which changes from a negative (counter-clockwise) radius during flood to a positive (clockwise) radius during ebb due to the *s*-shape curvature at the transect. The magnitude of  $R$  is difficult to calculate. For flood curvature we estimate a radius of approximately 4 km based on the change of flow direction between the ADCP at station *A* and another one situated further up-stream between the two barrier islands. Since we do not have any information about the change of the velocity field in the landward curve, we are forced to make a rough estimate based on the bathymetry, yielding a value of about 4 km as well. The uncertainty associated with the rough estimation of the radius of curvature is displayed in Figure 5.9, by the pink shaded area giving a range from 2 to 8 km of radius. Even though it is not possible to exactly calculate the effect of curvature, it is obvious that it plays an important role in the generation of lateral circulation.

The contribution induced by Coriolis force (yellow line in Figure 5.9) changes sign as well from positive flood to negative ebb values. Compared to buoyancy forcing and curvature the effect of earth's rotation is found to be rather small.

The earlier described asymmetry in lateral circulation must thus be due to the interplay of curvature and buoyancy forcing. During flood both terms,  $\omega_x^{curv}$  and  $\partial_y \langle b \rangle_z$ , have the same sign reinforcing one another to generate strong positive lateral circulation. On the other hand during ebb, both terms have opposite signs with comparable magnitudes and thus offset each other (Figure 5.9), which yields decreasing lateral circulation and a complete shut-down around full ebb tide (Figure 5.8). A similar asymmetry, associated with Earth's rotation, is described by Scully et al. (2009).

In section 5.3.2 we introduced some non-dimensional numbers that allow us to quantify the relative importance of the different terms displayed in figure 5.9. The relative importance of mixing and curvature forcing can be expressed by the non-dimensional radius of curvature,  $\hat{R}$ . Using typical parameters for our measurement site, like  $H = 15$  m and  $C_d = 3 \cdot 10^{-3}$ , we find  $\hat{R} = 0.75 \dots 3.0$  for curvature radii,  $R$ , between 2 km to 8 km, respectively.  $\hat{R}$  is of the order of unity or maybe even larger here, which might indicate a slight dominance of tidal mixing over curvature-induced lateral circulation (at least at peak tidal currents). This supports the hypothesis that curvature forcing alone is not able to produce the pronounced lateral circulation during flood.

The curvature Simpson number,  $Si_r$  (see equation (5.26)), provides a bulk quantity to measure the relative importance of lateral buoyancy forcing and curvature forcing. Depending on the radius of curvature, we find  $Si_r = 0.2 \dots 0.7$ , which suggests that,

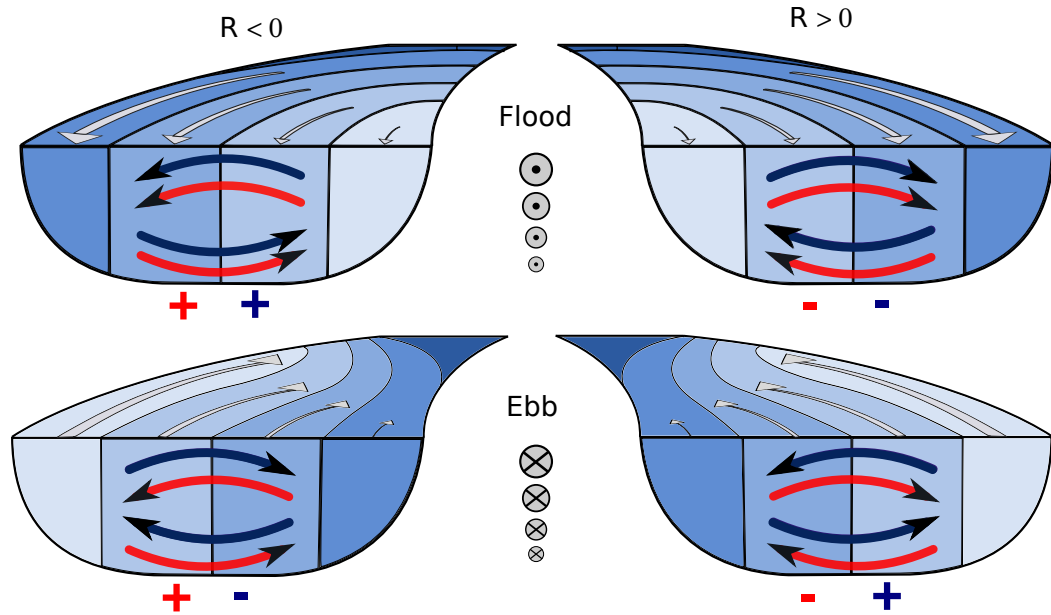


Figure 5.10.: Sketch of the lateral circulation in a curved channel induced by the baroclinic pressure gradient (blue) and curvature alone (red), for a positive (right) and negative radius of curvature (left), respectively. It is distinguished between flood (upper row) and ebb currents (lower row). Note that the along-channel buoyancy gradient is considered to be positive, corresponding to decreasing density in up-estuary direction.

although curvature forcing is slightly stronger than the lateral buoyancy gradient, both terms are of comparable importance in terms of the generation of lateral circulation. Thus the interplay of both terms determines the lateral dynamics at station *A*.

### Conceptual interplay of curvature and buoyancy

Since the interplay of curvature forcing,  $\omega_x^{curv}$ , and lateral buoyancy gradient,  $\partial_y \langle b \rangle_z$ , is responsible for the strong asymmetric lateral circulation at our particular site, we now consider their general relation in a conceptual context, in order to check whether the findings discussed above have some general implications for other systems as well.

Imagine a horizontally stratified channel, such that there is a homogeneous positive along-channel buoyancy gradient,  $\partial_x \langle b \rangle_z > 0$ , (the *x*-axes is pointing along the channel into the estuary). Lateral buoyancy gradients,  $\partial_y \langle b \rangle_z$ , are assumed to be only generated due to differential advection, associated with lateral shear. This lateral shear is considered to be only caused by curvature, in the sense that the centrifugal force acting on the mean along-channel current leads to larger along-channel velocities at the outer curve than in the inner.

Figure 5.10 shows a sketch of such a system, with different orientations of the curvature, in the left column with a negative (counter-clockwise) and in the right column with a positive (clockwise) radius of curvature. During flood (see upper row Figure 5.10) the denser water is transported faster on the outer bend, yielding an across-channel buoyancy gradient,  $\partial_y b$ , which is positive for a counter-clockwise (left column) and negative (right

column) for a clockwise orientation of the curve (note that the  $y$ -axis is pointing from left to right). The associated forcing in terms of lateral circulation has the same sign as  $\partial_y b$  (see equation (5.18)) and is indicated by the dark blue arrows in Figure 5.10. As discussed before the curved channel itself without any buoyancy gradients is able to generate secondary circulation via  $\omega_x^{curv}$  in equation (5.18). Interestingly, during flood this forcing term (red arrows in Figure 5.10) has always the same orientation as the buoyancy forcing, such that both terms reinforce each other.

Conversely, during ebb lighter water from inside the estuary is transported faster on the outer bend to yield a lateral buoyancy gradient in the opposite direction (increasing density from the outer to the inner bend). Since the curvature forcing,  $\omega_x^{curv}$ , retains its orientation but  $\partial_y b$  is reversed, both forcing mechanisms tend to offset each other, leading to reduced lateral circulation.

The general relation that lateral buoyancy forcing and curvature forcing reinforce each other during flood and compete with each other during ebb is true for any orientation of the curve. The particular study site discussed above with its  $S$ -shape curve corresponds to a combination of a counter-clockwise flood curve (upper left panel Figure 5.10) and a clockwise ebb curve (lower right panel Figure 5.10), which is the reason that  $\partial_y b$  is not changing sign between flood and ebb, but the curvature forcing,  $\omega_x^{curv}$  (see Figure 5.9).

Nevertheless, our general conceptual discussion shows that for any curved channel, where it does not matter if it has a  $S$ - or  $U$ -shape, we would expect a similar behavior with an enforced lateral circulation during flood and a reduced circulation during ebb, as long as curvature and buoyancy forcing are of comparable orders of magnitude, or in other words the curvature Simpson number (5.26) is of the order of unity.

Depending on the circumstances of the particular study-site it should be possible to find similar asymmetries in lateral circulation caused by other predominant balances in equation (5.18). Scully et al. (2009) for instance showed for the Hudson River estuary a comparable asymmetrical interplay of Coriolis forcing,  $\omega_x^f$ , and the lateral buoyancy gradient. Also a balance between curvature and Coriolis forcing could be able to yield asymmetrical secondary circulation under certain circumstances (see e.g. Geyer (1993); Alaei et al. (2004); Buijsman and Ridderinkhof (2008)), even in the absence of any buoyancy gradients.

Therefore, asymmetrical lateral circulation is likely to be a characteristic feature of a broad range of estuaries and curved channels.

### 5.5.3. Implications for estuarine circulation

There are a number of ways in which lateral circulation is able to generate or modify estuarine (along-channel) circulation. Directly (a) via the lateral transport of along-channel momentum (see  $\omega_y^{LC}$  in equation (5.19)), which was found to be of greater importance than classical gravitational circulation in many systems (Lerczak and Geyer, 2004), (b) in combination with curvature, represented by the term  $\omega_y^{curv}$  in equation (5.19), and (c) via the Coriolis deflection of lateral circulation towards along-channel circulation ( $\omega_y^f$  in equation (5.19)).

In addition, secondary circulation can also indirectly influence estuarine circulation by increasing the along-channel shear which contributes to the viscosity-shear correlation



(Burchard and Schuttelaars, 2012) that originally was identified with tidal straining (Burchard et al., 2011). Another indirect influence on estuarine circulation is the secondary circulation's effect on vertical stratification. As shown above, lateral circulation generates or modifies vertical stratification. Stratification yields a reduction of turbulence and thus a reduction of vertical turbulent viscosities, which influences the viscosity-shear correlation as well, or in terms of the framework developed in section 5.3.2, it effects  $\omega_y^{mix_i}$  in equation (5.19).

Independent of the relative importance of the different processes, a strong asymmetry in lateral circulation is likely to introduce an asymmetry in the along-channel circulation that ultimately results in a tidally-averaged exchange flow.

### Along-channel circulation, $[\omega_y]$

The along-channel circulation,  $[\omega_y]$ , is mainly positive during flood and negative during ebb (see blue line Figure 5.8). This general behavior is due to the fact that a major part of vertical shear of along-channel momentum is caused by bottom friction in well-mixed estuaries. In terms of the framework presented in section 5.3.2, it is generated via  $\omega_y^{mix_b}$  and then destroyed to a large fraction via internal mixing,  $\omega_y^{mix_i}$ . Thus the balance between bottom friction and internal mixing is responsible for most of the variation of  $[\omega_y]$  in well-mixed conditions.

Estuarine circulation can be interpreted as the tidal average of the along-channel circulation,  $\langle[\omega_y]\rangle_{M2}$ , where negative values correspond to the classical estuarine circulation with flood directed residual currents near the bottom and seaward velocities near the surface.

In a perfectly symmetric unstratified estuary the friction terms could not contribute to estuarine circulation, because they would have similar magnitudes with opposing signs during ebbs and floods. Hence, net estuarine exchange flow, other than the directly-forced baroclinic exchange, needs to be always associated with some kind of tidal asymmetry. This could be barotropic asymmetries (see e.g. Speer and Aubrey (1985); Friedrichs and Aubrey (1988)) yielding different magnitudes of  $\omega_y^{mix_b}$  at ebb and flood, respectively, or a baroclinic mixing asymmetries, like tidal straining (Jay and Musiak, 1994). Such an internal mixing asymmetry acts on  $\omega_y^{mix_i}$ , for instance via stratification that yields a suppression of the vertical momentum flux, which leads to a relatively smaller internal mixing term in equation (5.19) that is thus not able to balance bottom friction as well as under well-mixed conditions.

Based on the underlying measurements it is difficult to correctly quantify the contribution of the internal mixing-asymmetry due to vertical stratification. The difference between  $\omega_y^{mix_b}$  and  $\omega_y^{mix_i}$  compared to their magnitudes is very small and thus hard to resolve, given the fact that we depend on rather rough estimations of the mixing terms. Hence, we concentrate on the other tidal asymmetries in the balance (5.19).

Although much of the variation of  $[\omega_y]$  seems to be due to bottom friction, it is possible to identify significant deviations. The most obvious asymmetry is found at the end of each flood, where  $[\omega_y]$  is changing sign long before slack-tide (see Figure 5.8). Since negative values of the  $y$ -component of the vorticity correspond to the orientation of classical estuarine circulation, this particular asymmetry seems crucial in generating net estuarine exchange flow.

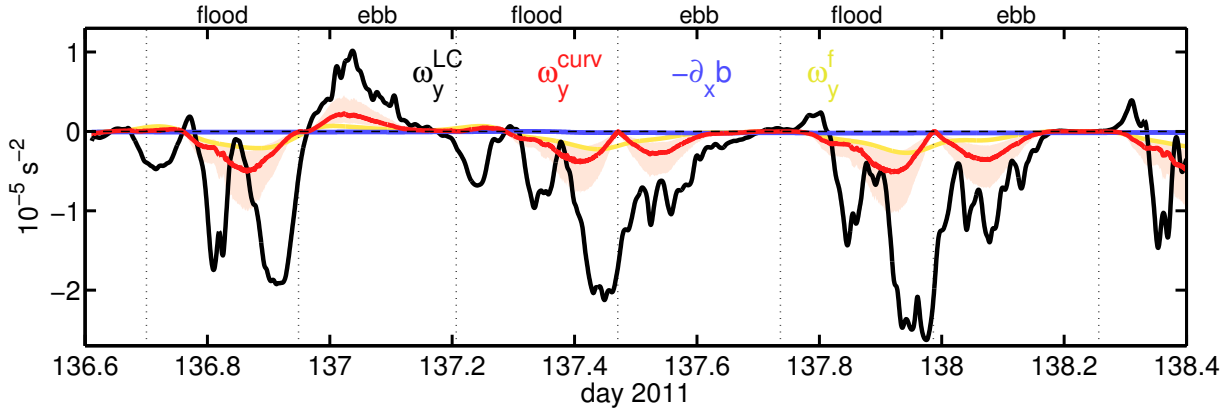


Figure 5.11.: Different terms of equation (5.19) changing longitudinal circulation at station A. Displayed are in blue the contribution of the direct baroclinic pressure forcing (gravitational circulation),  $\partial_x \langle b \rangle_z$ , in yellow the Coriolis deflection of lateral circulation,  $\omega_y^f$ , and in red the direct curvature forcing, where the red line corresponds to a radius of curvature of 4 km and the pink shaded background displays a range from 2 to 8 km of curvature (compare Figure 5.9). The black line shows the direct contribution of lateral circulation,  $\omega_y^{LC}$ , which is due to the differential lateral transport of along-channel momentum.

Figure 5.11 shows the different contributions of (5.19), generating along-channel circulation, excluding the mixing terms, which are difficult to estimate as discussed above. Except for  $\partial_x \langle b \rangle_z$ , all those terms are related directly or indirectly to lateral circulation, they are highly asymmetrical, and negative most of the time indicating that they all contribute to the generation of net estuarine exchange flow. Nevertheless, they have different magnitudes.

The direct buoyancy forcing (blue line in Figure 5.11),  $-\partial_x \langle b \rangle_z$ , is by far the smallest term, most of the time at least one order of magnitude smaller than the others, indicating that classical gravitational circulation can be neglected here.

The Coriolis deflection of lateral circulation (yellow line in Figure 5.11), is directly proportional to the  $x$ -component of the vorticity (compare red line in Figure 5.8), but relatively small as well.

The red line in Figure 5.11 displays the contribution due to curvature. As discussed above it is associated with an uncertainty which is due to the missing knowledge of the correct radius of curvature. Nevertheless, it seems to significantly contribute to estuarine circulation, although it is not the most important term.

$\omega_y^{LC}$  is found to be by far the most important term of those displayed in Figure 5.11. Interestingly, it peaks towards the end of flood, where we identified the most striking asymmetry in  $[\omega_y]$  (see Figure 5.8). This link strongly supports the idea that a major part of net estuarine circulation is due to lateral transport of along-channel momentum, associated with asymmetric lateral circulation induced by the interplay of curvature and buoyancy forcing.

## 5.6. Conclusions

Based on measurement data taken in a tidal inlet of the German Wadden Sea, this study presents a consistent picture of the interplay between lateral dynamics, estuarine circulation, and stratification in a weakly-stratified estuary. In order to do so, a framework is developed that allows the study of generation mechanisms of across- and along-channel circulation and their interdependencies in a consistent way.

The observations show the occurrence of late flood stratification that is predominantly due to lateral circulation, and the associated lateral straining of the across-channel density gradient, which is found to be at least one order of magnitude larger than the along-channel gradient most of the time.

A strong clockwise lateral circulation, coherent over the entire channel, is found during flood, keeping its orientation at the beginning of ebb before breaking down completely during ebb. This asymmetric lateral circulation is shown to be due to the interplay of curvature-induced secondary circulation and the horizontal buoyancy gradient. Differential advection of the along-channel density gradient, caused by centrifugal forces acting on the tidal currents, yields a strong across-channel baroclinic pressure gradient that enhances curvature-induced lateral circulation during flood and counteracts it during ebb.

This systematic asymmetry in the generation of lateral circulation is likely to be a characteristic feature of a broad range of well-mixed curved estuaries, as long as the non-dimensional radius of curvature,  $\hat{R}$  (defined in (5.27)), is small and the curvature Simpson number,  $Si_r$  (see (5.26)), which is the ratio of buoyancy and curvature forcing, is of the order of unity.

Finally this study shows that asymmetric lateral circulation induces a strong asymmetry in the generation of along-channel circulation. The asymmetric along-channel circulation results in estuarine circulation, which is identified as the tidal average of the across-channel vorticity. Thus curvature-induced asymmetric lateral circulation is likely to be a major source of estuarine exchange flow in well-mixed estuaries.



# 6. Vorticity-Model: Jump and circulate

## 6.1. Introduction

In the previous chapters we investigated the dynamical condition of two tidal inlets based on measurement data. Since measurements are usually very limited in terms of spatial and/or temporal resolution, and often only cover short periods they are a very limited tool in order to determine the dynamical state of a system. Nevertheless, we were able to identify a number of interesting processes that are likely to have large influence on the dynamics of the particular inlets. In order to test if those processes are really able to explain a major fraction of the observed dynamics and to check if they are possibly relevant for other systems as well, we provide an idealized modelling study in this chapter.

As pointed out in chapter 3, we use the vorticity equations in order to study the circulation dynamics of estuaries in this thesis. Pushing this idea further, we develop an idealized model in this chapter, which is based on the vorticity balances. To focus on the processes described above and to guarantee a high-resolution parameter study, we use an idealized zero-dimensional model. The model is especially designed in order to study the interaction of horizontal buoyancy gradients and centrifugal forcing, which we identified in the previous chapter as one of the key mechanisms, determining the estuarine dynamics in the studied tidal inlets.

In section 6.2 we provide a detailed model description, together with non-dimensional numbers that are useful for further investigations. In the following section 6.3, we validate the model with the Spiekeroog observations, analyzed in the previous chapter. Since our process study in chapter 5 was based on data taken at the inflection of an *S*-shape channel, we use section 6.4 to investigate if our findings can be generalized to all kinds of curved channels. Section 6.5 is dedicated to an exploration of the parameter space of well-mixed to weakly-stratified estuaries, to find out how relevant our findings might be for other systems. A summary of the findings as well as some open questions that arised during our investigations can be found in section 6.6.

## 6.2. Model description

As mentioned above, our model is based on the calculation of the three bulk vorticity components for an idealized transect (see Figure 6.1) together with the corresponding buoyancy gradients. Thus, it consists of a set of five coupled differential equations plus a prescribed forcing equation,  $\{\partial_x b\}$ . It is important to note that the model is not meant to laterally resolve the dynamics, but provides bulk values valid for an entire cross-section. The model domain corresponds to a curved rectangular channel of width  $B$  and depth  $H$ , which is uniform in the  $x$ -direction (along-channel direction). In the implementation

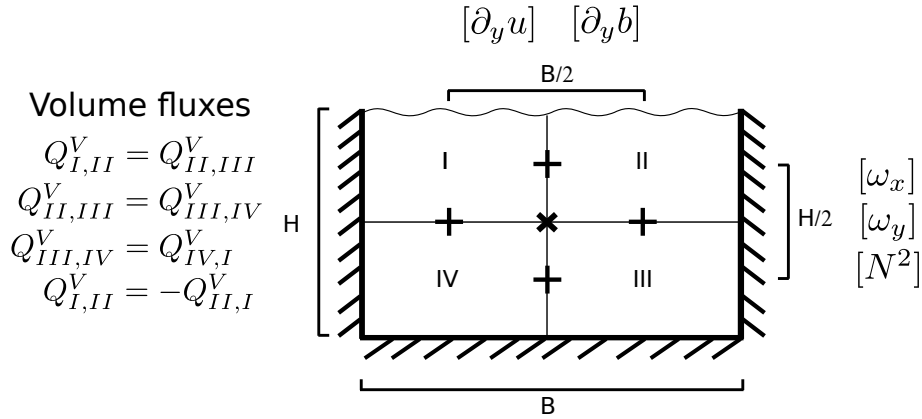


Figure 6.1.: Sketch of the model domain: A rectangular channel cross-section of the width  $B$  and the depth  $H$ . All equations are solved for the center point marked with an  $x$ . Due to the rigid lid surface condition, there is a distinct relation of the volume fluxes between the certain quadrants. Here  $Q_{I,II}^V$  denotes the volume flux from quadrant I to II,  $Q_{II,III}^V$  the flux from II to III and so fourth.

presented here lateral depth-variation are ignored.

### 6.2.1. Model assumptions

Since the model is uniform in  $x$ , all along channel gradients are ignored, except the along-channel buoyancy gradient  $\{\partial_x b\}$ , which is assumed to be vertically constant. Note that the  $x$ -coordinate points along the curved channel in up-estuary direction, such that  $\{\partial_x b\}$  is positive for usual estuarine conditions. A consequence of the vanishing along-channel gradient of the along-channel velocity,  $\partial_x u = 0$ , is a two-dimensional version of the continuity equation (2.3),

$$\partial_y v = -\partial_z w . \quad (6.1)$$

For the surface of the channel cross-section a rigid lid condition is prescribed, which leads to a vanishing vertical mean across-channel velocity component,  $\langle v \rangle_z = 0$ . The interface between upper and lower water column (see figure 6.1) is assumed to be located at the zero crossing of the across-channel velocity component,

$$v|_{-H/2} = 0 . \quad (6.2)$$

Because of that the lateral gradient  $\partial_y v$  is zero at the interface too, which in combination with continuity equation (6.1) yields

$$\partial_y v|_{-H/2} = \partial_z w|_{-H/2} = 0 . \quad (6.3)$$

The vertical gradients of the velocity  $\partial_z u$  and  $\partial_z v$ , and of the buoyancy frequency,  $N^2 = \partial_z b$ , are considered to be vertically constant,

$$\partial_{zz}^2 u = \partial_{zz}^2 v = \partial_{zz}^2 b = 0 . \quad (6.4)$$

In addition we assume that the lateral buoyancy gradient,  $[\partial_y b]$ , is constant in space,

$$\partial_x[\partial_y b] = \partial_y[\partial_y b] = \partial_z[\partial_y b] = 0 . \quad (6.5)$$

Furthermore, we neglect all surface buoyancy and momentum fluxes,

$$\langle u'w' \rangle|_0 = \langle v'w' \rangle|_0 = \langle w'b' \rangle|_0 = 0 . \quad (6.6)$$

Finally, we ignore lateral depth-variation,

$$\partial_y H = 0 , \quad (6.7)$$

which might be a major constraint, since it is known to be a major source of lateral circulation (Nunes and Simpson, 1985; Lerczak and Geyer, 2004; Burchard et al., 2011). However, since we are especially interested in the interplay of curvature and buoyancy forcing we ignore lateral depth variation on purpose, to investigate how much of the secondary dynamics are not associated with lateral differences in bottom friction.

### 6.2.2. Vertical gradients

Analog to section 5.3.2 it is possible to derive transport equations for the along- and the across-channel vorticity.<sup>1</sup> The model equations for the horizontal vorticity components read as (for details of the derivation see appendix A.2),

$$\begin{aligned} \partial_t [\omega_x] = & \overbrace{[\partial_y b]}^{[\omega_x]^b} + \overbrace{f [\omega_y]}^{[\omega_x]^f} - \overbrace{\frac{2}{R} \{u\} [\omega_y]}^{[\omega_x]^r} \\ & - \overbrace{\frac{8}{H^2} \langle v'w' \rangle|_{-\frac{1}{2}H}}^{[\omega_x]^{m_i}} + \overbrace{\frac{4}{H^2} \langle v'w' \rangle|_{-H}}^{[\omega_x]^{m_b}} , \end{aligned} \quad (6.8)$$

and

$$\begin{aligned} \partial_t [\omega_y] = & -\overbrace{\{\partial_x b\}}^{[\omega_y]^b} - \overbrace{f [\omega_x]}^{[\omega_y]^f} + \overbrace{\frac{1}{R} \{u\} [\omega_x]}^{[\omega_y]^r} + \overbrace{[\partial_y u] [\omega_x]}^{[\omega_y]^{lc}} \\ & + \overbrace{\frac{8}{H^2} \langle u'w' \rangle|_{-\frac{1}{2}H}}^{[\omega_y]^{m_i}} - \overbrace{\frac{4}{H^2} \langle u'w' \rangle|_{-H}}^{[\omega_y]^{m_b}} , \end{aligned} \quad (6.9)$$

where squared brackets,  $[\cdot]$ , denote quantities calculated within the model and curly brackets,  $\{\cdot\}$ , label time dependent forcing parameters, used as diagnostic variables.<sup>2</sup> The

<sup>1</sup>Recall that the  $x$ -component of the vorticity corresponds to the vertical shear of the lateral velocity-component,  $\omega_x = -\partial_z v$ , and the  $y$ -component to the vertical shear of the along-channel velocity component,  $\omega_y = \partial_z u$ , respectively.

<sup>2</sup>Note that  $H$  could be also time-dependent, if changing water levels are considered, but in the following we use a constant water depth neglecting all surface elevation.

equations (6.8) and (6.9) are very similar to (5.18) and (5.19), but in order to distinguish the terms of (5.18) and (5.19) that are based on estimates from measurement data, from the terms of (6.8) and (6.9) that represent model calculations we use a slightly different notation here.

The terms in equation (6.8) and (6.9) labeled with  $[\cdot]^b$  are due to direct buoyancy forcing,  $[\cdot]^f$  Coriolis deflection,  $[\cdot]^r$  curvature induced deflection,  $[\cdot]^{mi}$  inter-facial friction, and  $[\cdot]^{mb}$  bottom friction. In (6.9) there additionally appears a term,  $[\omega_y]^{lc}$ , that is due to the lateral transport of along-channel momentum, which can be understood as the direct influence of lateral circulation on longitudinal exchange flow (see also discussion chapter 3).

Analog to the vertical gradients of the velocity, (6.9) and (6.8), it is possible to derive a transport equation for the vertical gradient of the buoyancy, the so called buoyancy frequency  $[N^2]$ , for a two layer fluid (for details see Appendix A.2.3),

$$\partial_t [N^2] = \underbrace{-\{\partial_x b\}[\omega_y]}_{[N^2]^{S_x}} + \underbrace{[\partial_y b][\omega_x]}_{[N^2]^{S_y}} + \underbrace{\frac{8}{H^2} \langle w'b' \rangle}_{[N^2]^{m_i}} \Big|_{-\frac{1}{2}H} . \quad (6.10)$$

Here,  $[N^2]^{S_x}$  and  $[N^2]^{S_y}$  denote the longitudinal and lateral straining terms, respectively. The mixing term,  $[N^2]^{m_i}$ , is just an internal mixing term, since surface and bottom fluxes of buoyancy are ignored. It corresponds to twice the normalized turbulent buoyancy flux at the interface between upper and lower layer.

Note that there is a straight forward relation between the bulk-buoyancy frequency and the potential energy anomaly for a two-layer fluid (see Appendix A.3),

$$[\Phi] = \frac{\rho_0 H^2}{16} [N^2] . \quad (6.11)$$

By making use of (6.11) it is easy to show that (6.10) corresponds to the transport equation of the potential energy anomaly (5.5) (Burchard and Hofmeister, 2008) for a two layer fluid, neglecting all advection and non-mean straining terms.

### 6.2.3. Lateral gradients

Taking the derivative of (2.5) with respect to  $y$  yields a transport equation for the lateral buoyancy gradient (for details see Appendix A.2)

$$\partial_t [\partial_y b] = \underbrace{-[\partial_y u]\{\partial_x b\}}_{[\partial_y b]^{da}} - \underbrace{\frac{H^2}{B^2} [\omega_x][N^2]}_{[\partial_y b]^{N^2}} . \quad (6.12)$$

In (6.12)  $[\partial_y b]^{da}$  denotes the change of  $[\partial_y b]$  due to differential advection of the along channel buoyancy gradient, and  $[\partial_y b]^{N^2}$  the change due to tilting of horizontal isopycnals. Note that  $[\partial_y b]^{N^2}$  has generally the tendency to suppress lateral circulation due to a build up of a compensating lateral buoyancy gradient (Chant and Wilson, 1997; Lacy and Monismith, 2001; Nidzieko et al., 2009). However, in weakly stratified estuaries with sufficient curvature or lateral bathymetric gradients, yielding lateral shear,  $[\partial_y b]^{da}$  is likely



to be of greater importance, allowing for both positive and negative feedbacks between  $[\partial_y b]$  and  $[\omega_x]$ . The relative importance of  $[\partial_y b]^{N^2}$  and  $[\partial_y b]^{da}$  might be crucial in describing the difference between well-mixed and stratified estuaries.

Analog to (6.12) it is possible to derive a transport equation for the lateral shear, based on the  $y$ -derivative of (2.1) (for details see Appendix A.2),

$$\partial_t[\partial_y u] = \underbrace{-\frac{H^2}{B^2}[\omega_x][\omega_y]}_{[\partial_y u]^{lc}} - \underbrace{\frac{2\sqrt{C_d}}{H}[u_*][\partial_y u]}_{[\partial_y u]^{mb}}. \quad (6.13)$$

$[\partial_y u]^{lc}$  denotes the contribution of rectification of vertical shear of the along channel momentum due to lateral circulation, which is proportional to the square of the aspect ration,  $H/B$ .  $[\partial_y u]^{mb}$  on the other hand represents the reduction of lateral shear due to bottom friction. Thus, in our model the transport equation for the lateral shear (6.13), is just a balance between lateral circulation  $[\partial_y u]^{lc}$  and bottom friction  $[\partial_y u]^{mb}$ . Note that the lateral shear directly corresponds to the vertical vorticity component,  $\omega_z = -\partial_y u$ , which is why (6.13) can be also read as an equation for the bulk vertical vorticity,  $[\omega_z]$ , or in other words for the horizontal circulation.

#### 6.2.4. Turbulence closure

In the model framework described here bottom friction is assumed to be the only source of turbulence. A convenient variable to quantify bottom friction is the so called friction velocity, which is calculated according to

$$u_* = \sqrt{C_d(u_b^2 + v_b^2)} = \left[ C_d \left( \{u\} - \frac{H}{4}[\omega_y] \right)^2 + C_d \left( \frac{H}{4}[\omega_x] \right)^2 \right]^{\frac{1}{2}}, \quad (6.14)$$

where  $u_b$  and  $v_b$  denote the along- and across-channel component of the velocity in the bottom layer, respectively (for details see appendix (A.1)). Based on the friction velocity it is possible to calculate the turbulent fluxes occurring in the model equations (6.8), (6.9), (6.10), and (6.13), in order to close the set of equations.

The bottom friction term in equation (6.8) is calculated by,

$$[\omega_x]^{mb} = \frac{4}{H^2} \langle v'w' \rangle \Big|_{-H} = -\frac{4}{H^2} |u_*| u_*^y = -\frac{\sqrt{C_d}}{H} |u_*| [\omega_x], \quad (6.15)$$

where  $u_*^y = \frac{1}{4}H\sqrt{C_d}[\omega_x]$  denotes the  $y$ -component of the friction velocity. Analogously, the friction term in equation (6.9) is calculated according to

$$[\omega_y]^{mb} = -\frac{4}{H^2} \langle u'w' \rangle \Big|_{-H} = \frac{4}{H^2} |u_*| u_*^x = \frac{4\sqrt{C_d}}{H^2} |u_*| \left( \{u\} - \frac{H}{4}[\omega_y] \right), \quad (6.16)$$

where  $u_*^x = \sqrt{C_d}(\{u\} - 1/4H[\omega_y])$  denotes the  $x$ -component of the friction velocity.

The inter-facial turbulent fluxes are modeled based on the down-gradient assumption, which yields

$$[\omega_x]^{mi} = -\frac{8}{H^2} \langle v'w' \rangle \Big|_{-\frac{1}{2}H} = -\frac{8}{H^2} [\nu_t][\omega_x], \quad (6.17)$$

for the along-channel vorticity equation (6.8),

$$[\omega_y]^{m_i} = \frac{8}{H^2} \langle u'w' \rangle \Big|_{-\frac{1}{2}H} = -\frac{8}{H^2} [\nu_t][\omega_y] , \quad (6.18)$$

for the across-channel vorticity equation (6.9), and

$$[N^2]^{m_i} = \frac{8}{H^2} \langle w'b' \rangle \Big|_{-\frac{1}{2}H} = -\frac{8}{H^2} [\nu_t^b][N^2] , \quad (6.19)$$

for the turbulent buoyancy flux occurring in (6.10).

In (6.17), (6.18), and (6.19) we introduced the turbulent viscosity,  $[\nu_t]$ , and the turbulent diffusivity of buoyancy,  $[\nu_t^b]$ . Both quantities are calculated by assuming a parabolic viscosity profile, which is modified following the approach of Munk and Anderson (1948), in order to take the inhibiting effect of vertical stratification on turbulent mixing into account (for details see appendix A.4). This yields for the the turbulent viscosity,

$$[\nu_t] = \frac{1}{4} u_* \kappa H (1 + 10[\text{Ri}_g])^{-\frac{1}{2}} , \quad (6.20)$$

and for the turbulent diffusivity of buoyancy

$$[\nu_t^b] = \frac{1}{4} u_* \kappa H \left( 1 + \frac{10}{3} [\text{Ri}_g] \right)^{-\frac{3}{2}} . \quad (6.21)$$

Here we introduced the gradient Richardson number that is calculated according to,

$$[\text{Ri}_g] = \frac{[N^2]}{([\omega_x]^2 + [\omega_y]^2)} . \quad (6.22)$$

The turbulence parametrization introduced in (6.20) and (6.21), based on Munk and Anderson (1948), is relative simple. Nevertheless, here it provides a consistent way of taking the turbulent length scale limitation of stratification into account, which is crucial in order to model effects of internal mixing asymmetries. In later implementations one could think of a more sophisticated turbulence model, which might be important when studying mixing asymmetries in detail.

### 6.2.5. Model parameters

There are two major forcing agents that are used to drive the model equations (6.8-6.13). The first driver is the depth-mean along-channel velocity,  $\{u\}$ . In the experiments described below it is prescribed with a sin-function,

$$\{u\} = u_A \sin(\omega_{M2}t) , \quad (6.23)$$

where  $u_A$  denotes the tidal velocity amplitude and  $\omega_{M2} = 2\pi 44724^{-1} \text{s}^{-1}$  denotes the tidal frequency, corresponding to a  $M_2$ -tide. For simplicity we use here just an ordinary sin-function to represent the tidal currents. Nevertheless, in future experiments it would be no problem to substitute (6.23) by a more complicated expression to add further tidal

Parameter	Symbol	Value	Unit
water depth	$H_0$	12	[m]
channel width	$B$	300	[m]
along-channel velocity amplitude	$u_A$	1.2	[m s <sup>-1</sup> ]
drag coefficient	$C_d$	$3 \cdot 10^{-3}$	-
velocity frequency (M <sub>2</sub> -tide)	$\omega_{M2}$	$2\pi/44724$	[s <sup>-1</sup> ]

Table 6.1.: List of parameter that are kept constant at all model setups discussed in the following.

components, for instance in order to study the variation in the spring-neap cycle or the effect of barotropic tidal asymmetries.

Within the model framework described above the depth-mean along channel velocity,  $\{u\}$ , plays two major roles. On the one hand it directly effects the curvature terms,  $[\omega_x]^r$  and  $[\omega_y]^r$ , in the vorticity equations (6.8) and (6.9), on the other hand it controls turbulence, which is generated here exclusively due to bottom friction of the tidal currents, quantified by the friction velocity,  $u_*$  (see (6.14)).

The second important driver is the along-channel buoyancy gradient,  $\{\partial_x b\}$ , which appears as a direct driver for along-channel circulation,  $[\omega_y]^b$ , in (6.9), as a part of the along-channel straining,  $[N^2]^{Sx}$ , in (6.10) and finally in the differential advection term,  $[\partial_y b]^{da}$ , in (6.12). In order to keep the model simple, we used a constant  $\{\partial_x b\}$ , but for other purposes it could also vary in time, for instance to simulate the passage of fronts.

Beside the two dynamical drivers the geometrical parameters are of great importance as well. The water depth  $H = H_0$  is kept constant during all the model runs presented in the following, but it can also be chosen to depend on time to study the impact of surface elevation. The channel width  $B$  could also be time dependent, for instance to include drying and flooding in an simplified form into the model. Nevertheless, here we use a constant  $B$  for reasons of simplicity. The last geometrical parameter is the radius of channel curvature,  $R$ , which will be constant in time,  $R = R_0$ , for simulations of a  $U$ -shaped channel. There are two experiments with a  $s$ -shaped channel discussed here. For those setups the radius of curvature is changing sign from flood to ebb,  $R = R_0 \text{sign}\{u\}$ .

Furthermore there are two additional parameters, the Coriolis parameter,  $f$ , to account for earth's rotation, and the drag coefficient,  $C_d$ , which can be used as a tuning parameter for the turbulence model. A list of all the parameters kept constant at all model setups dicussed below can be found at table 6.1.

### 6.2.6. Non-dimensional numbers

In terms of the geometry of the system, there are two non-dimensional numbers of importance, the non-dimensional radius of curvature  $\hat{R}$ , defined in (5.27), and the non-dimensional channel width  $\hat{B} = B/H$ , which corresponds to the inverse of the lateral aspect ratio.

To quantify the stratification characteristics of the model output, we introduce two

non-dimensional measures. The straining anisotropy is defined as,

$$M_{SA} = \frac{|[N^2]^{Sx}| - |[N^2]^{Sy}|}{\sqrt{\langle ([N^2]^{Sx})^2 + ([N^2]^{Sy})^2 \rangle_{T_P}}} \quad (6.24)$$

where  $\langle \cdot \rangle_{T_P}$  denotes the mean value in time with respect to the certain periodicity of the signal,  $P$ , which will be one  $M_2$ -tidal period in most cases (for more information please the Appendix A.5).  $M_{SA}$  is a measure for the relative importance of lateral,  $[N^2]^{Sy}$ , and longitudinal straining,  $[N^2]^{Sx}$ . For positive values along channel straining is dominant and vice versa for negative values of  $M_{SA}$ . The tidal mean of (6.24),  $\langle M_{SA} \rangle_{T_P}$ , provides a decent measure whether vertical stratification is in average rather dominated by along-channel or across-channel circulation.

To quantify if a particular system is well-mixed, weakly- or partially stratified, we introduce the *well-mixed parameter*,

$$P_{wm} = \frac{\int_{T_P} [1 - \theta(\text{Ri}_g - \frac{1}{4})] dt}{T_P} \quad (6.25)$$

with  $\theta(\text{Ri}_g - \frac{1}{4})$  being a step function that is equal to one for all values greater than a quarter and zero else. Thus  $P_{wm}$  provides a measure, which percentage of the tidal cycle is characterized by bulk gradient Richardson numbers below a quarter, widely accepted to be the *magical* threshold for positive turbulence production, usually associated with well mixed conditions.

In order to quantify the strength of the residual circulation, we follow Burchard et al. (2011), who proposed a measure for the net estuarine exchange flow for a two-dimensional channel cross-section (see their equation (15)). Adapting their formulation to our box-model formulation yields,

$$M_{ec} = -\frac{H}{2} \langle [\omega_y] \rangle_{T_P} , \quad (6.26)$$

and analog for the lateral exchange flow (compare Burchard et al. (2011) equation (16))

$$M_{lc} = \frac{H}{2} \langle [\omega_x] \rangle_{T_P} . \quad (6.27)$$

Note that (6.26) has the opposite sign than  $[\omega_y]$ , so that positive values of  $M(u)$  corresponds to classical estuarine exchange flow, up-estuary in the lower and sea-wards in the upper water column.

Analog to equation (5.26) we use a curvature Simpson number in order to quantify the ratio of baroclinic pressure gradient and curvature forcing for the generation of lateral circulation

$$Si_r = \frac{\langle |[\omega_x]^b| \rangle_{T_P} |R_0| H_0 \kappa}{4\sqrt{C_d} u_A^2} . \quad (6.28)$$

$Si_r$  can be also thought as a non-dimensional average magnitude of the lateral buoyancy gradient,  $\langle |[\omega_x]^b| \rangle_{T_P}$ , since centrifugal forcing appears in (6.28) just as a combination of constant parameters.

Exp-ID	$R_0$ [km]	$\partial_x b$ [ $10^{-6}\text{s}^{-2}$ ]	shape	$\hat{R}$	Si
Sp_A_s*	-4	0.75	s	1.87	0.025
SS_bx1	-4	0.75	s	1.87	0.025
US_bx1	-4	0.75	u	1.87	0.025
US_bx2	-4	1.50	u	1.87	0.050
Si_R2	2	0 ... 4.2	u	0.94	0 ... 0.14
Si_R4	4	0 ... 4.2	u	1.87	0 ... 0.14
Si_R8	8	0 ... 4.2	u	3.74	0 ... 0.14

Table 6.2.: Overview of all model setups discussed in this chapter. In the first row \* marks the run that was done with  $f = 10^{-4} \text{ s}^{-1}$ , whereas all the other runs neglect Earth rotation. Note Sp\_A\_s\* and SS\_bx1 are the same with respect to all parameters except for Earth's rotation, which is ignored for SS\_bx1.

## 6.3. Model Validation

In this section we try to figure out how well the simple vorticity-model is able to capture the principle dynamics of the  $s$ -shaped tidal inlet of Spiekeroog. To this end we are going to compare the observations presented in chapter 5 with results of our idealized model.

### 6.3.1. Model setup

The model contains a number of parameters that all could be used to tune the results in such a way that they nicely fit the observations. In chapter 5 we concluded that the major part of the dynamics observed at the point of inflection of the  $S$ -shaped inlet of Spiekeroog can be explained by an interplay of curvature and buoyancy forcing.

In order to check that hypothesis we limit ourselves to a minimum set of parameters necessary to do so. Those parameters are (1) a typical radius of curvature that we choose to be  $R_0 = -4 \text{ km}$ , in agreement with the findings of chapter 5;<sup>3</sup> (2) a channel width of  $B = 300 \text{ m}$ ;<sup>4</sup> (3) a constant water-depth of  $H = 12 \text{ m}$ ;<sup>5</sup> (4) a drag coefficient of  $C_d = 3 \cdot 10^{-3}$ ; (5) a constant along-channel buoyancy gradient of  $\{\partial_x b\} = 7.5 \cdot 10^{-7} \text{ s}^{-2}$ ; (6) an amplitude of the tidal currents of  $u_A = 1.2 \text{ m s}^{-1}$ , which is modulated with a sin-wave of a frequency of  $\omega_{M_2} = 2\pi/44724 \text{ s}^{-1}$ ;<sup>6</sup> and (7) a Coriolis parameter of  $f = 10^{-4} \text{ s}^{-1}$

<sup>3</sup>Note that in order to simulate the  $S$ -shape channel of Spiekeroog the radius is changing sign from negative values during flood to positive values during ebb. Therefore the time series of the radius of curvature is realized by the radius-parameter,  $R_0$ , multiplied by the sign of the depth average velocity,  $R(t) = R_0 \text{sign}\{u\}$ , in contrast to  $u$ -shape setups, where we take  $R(t) = R_0$ .

<sup>4</sup>300 m approximately corresponds to the channel width found at the measurement site (see 5.1).

<sup>5</sup>For simplicity we choose a constant water depth here, which excludes the influence of changing water levels,  $H(t) = H_0$

<sup>6</sup>For simplicity we decide to model the tidal currents with an ordinary sin-wave with only one tidal component, corresponding to the  $M_2$  lunar tide. In a more realistic setup one could also include higher harmonics like  $M_4$  tides that are known to have a large influence on the dynamics in the Wadden Sea.

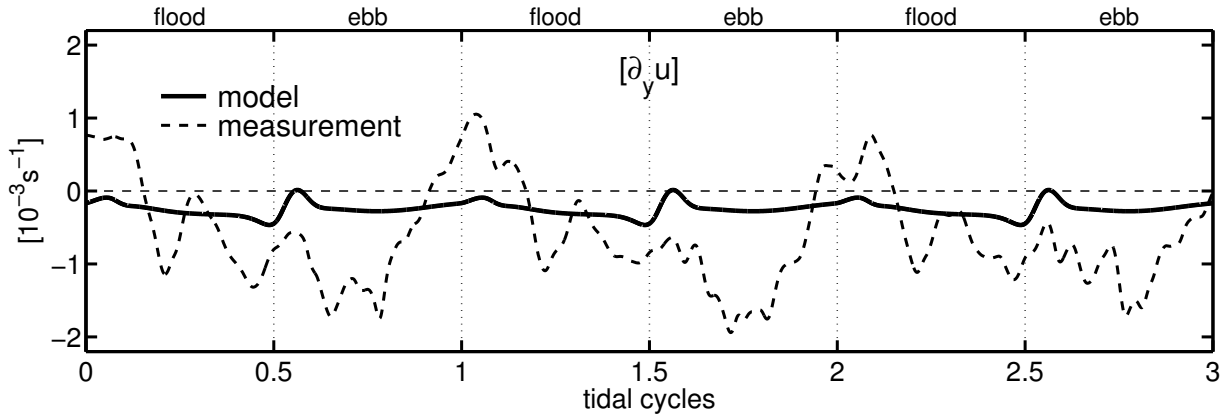


Figure 6.2.: Lateral shear of the along-channel velocity. The solid black line shows the model result for the lateral shear,  $[\partial_y u]$ , obtained by the *realistic* setup (see Sp\_A\_s\* in table 6.2), for three consecutive tidal cycles. The dashed line illustrates the lateral shear observed at the Spiekeroog inlet, calculated from the difference of the two anchored ADCP (compare figure 5.5)

that accounts for the effect of Earth’s rotation.<sup>7</sup> This choice of parameters is based on approximations or at least best guesses of the real situation in the Spiekeroog inlet. It is important to note that we have not done any parameter fine tuning in order to fit the model results to the observations.

We exclude the effect of lateral bathymetry variation here, which is known to be an important source of lateral dynamics in many estuaries (Nunes and Simpson, 1985; Lerczak and Geyer, 2004; Burchard et al., 2011). This is basically done for two reasons, on the one hand there is no straight forward estimate of  $\partial_y H$  for the Spiekeroog inlet and on the other hand the aim here is to check the hypothesis, if the interplay of curvature and buoyancy forcing alone is able to reproduce the dynamics described in chapter 5.

An overview on the choice of parameters can be found in table 6.1, which contains the parameters kept the same for all model setups discussed in this chapter, and table 6.2, showing those parameters that are specifically chosen for the *realistic* run, that is labeled with Sp\_A\_s\* (first row table 6.2), and used here to compare to the measurement data discussed in chapter 5.

## 6.3.2. Results

### Lateral shear

Figure 6.2 shows the simulated lateral gradient of the along channel velocity as a solid black line,  $[\partial_y u]$ , and in addition the estimate of the lateral shear for the Spiekeroog inlet (dashed line), based on the difference between the two anchored ADCPs (for details revisit section 5.4.3). The general tendency of negative values most of the time is reproduced nicely here. Negative values of  $[\partial_y u]$  correspond to larger currents during flood

<sup>7</sup>Although we found in chapter 5 that Earth’s rotation is rather of minor importance at the particular measurement site, it is still included here to make the setup more realistic.

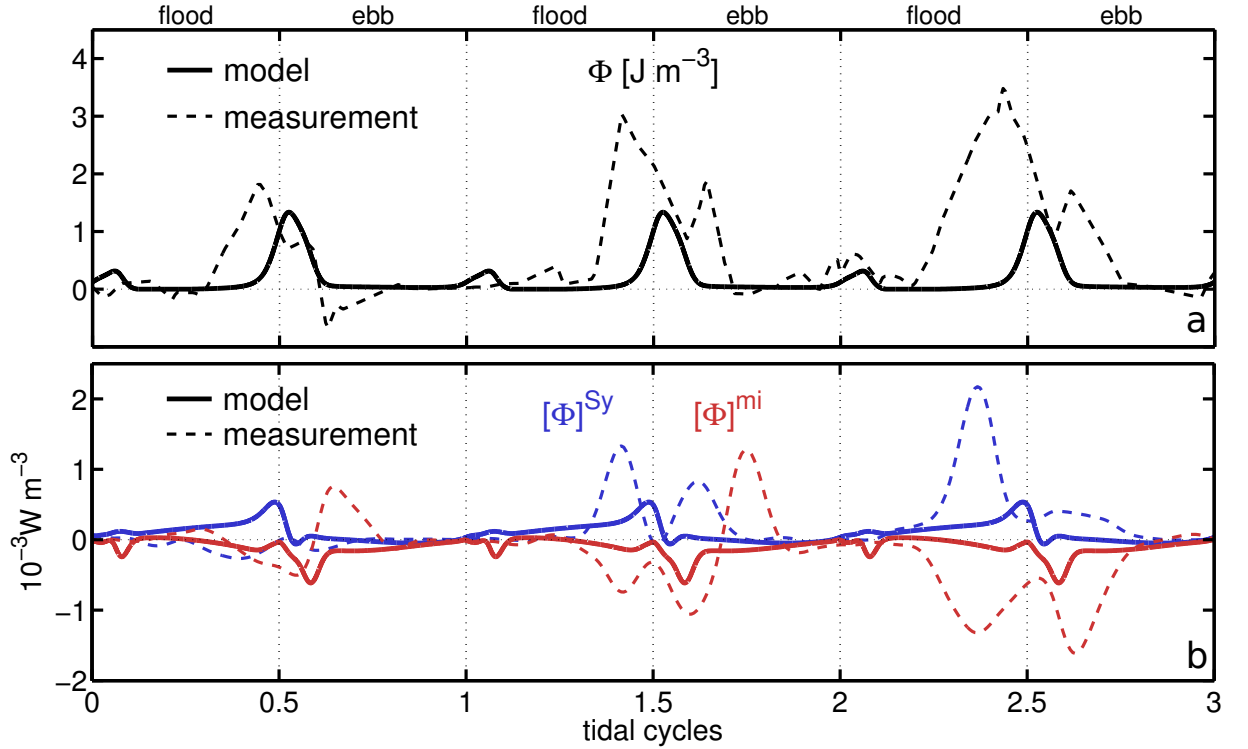


Figure 6.3.: Vertical Stratification. Panel (a) shows the time series of the potential energy anomaly and panel (b) the most important terms of its transport equation (compare (5.5) and (6.10)), namely lateral straining,  $[\Phi]^{Sy}$ , and vertical mixing,  $[\Phi]^{mi}$ . The solid lines represents data obtained by the model using setup Sp\_A.s\* and the dashed line the corresponding measurement data at station A in the Spiekeroog inlet (compare figure 5.6 and figure 5.7).

in the southern side of the channel and vice versa during ebb. As discussed earlier the phenomenon is due to the *S*-shape curvature of the channel, which is taken into account in the model.

In general, the model slightly underpredicts the lateral shear. Nevertheless, the average simulated lateral shear has approximately the same order of magnitude as the measured signal. Beside that, there can be found two major differences in the temporal behavior, first the positive values found in the observations around low water slack tide can not be reproduced by the model and second the negative peak values occurring during strong ebb in the measurement data are not found in the simulation results either.

### Vertical stratification

The potential energy anomaly, as a measure of vertical stratification, is a key parameter, since its time series at the northern station of the Sylt-Rømø inlet as well as in the main-channel of the Spiekeroog basin, provided the first contradiction to the theory of classical along-channel tidal straining as the most important baroclinic process in the Wadden Sea, which lead to a further investigation of lateral processes that are a major subject of this

thesis.

Figure 6.3a provides a comparison between model outcome (solid line) and observations (dashed line) for the time series of the potential energy anomaly,  $\Phi$ , at station  $A$  in the Spiekeroog inlet (see figure 5.1). The results of the idealized model fit the observation surprisingly well. The occurrence of a strong peak of vertical stratification at high water slack tide is nicely reproduced, although slightly underestimated in terms of its magnitude. A smaller low-water peak found in the model data can be also seen in the measurement data at least during the last observed cycle.

The major difference between both curves is the timing of the peak in stratification, which occurs in the observations earlier than in the model data, already in the second half of flood tide.

If we concentrate on the source of vertical stratification (see figure 6.3b), we find that in the observations as well as in the idealized model lateral straining (blue line) is the most important source of potential energy anomaly and interfacial mixing (red line) the major sink. The major features of the time series are nicely reproduced by the model, which are a strong peak short before and a smaller peak short after high water for  $[\Phi]^{Sy}$  and vice versa for the mixing term  $[\Phi]^{mi}$ , who's major peak is found after high water slack.

### Lateral circulation

The model with the setup Sp\_A\_s\* (see table 6.2) is able to capture most of the dynamics in terms of lateral circulation observed at measurement station  $A$  (see figure 6.4a), strong positive along-channel vorticity (red line figure 6.4a) during flood, peaking towards high water, and significantly reduced lateral circulation during ebb. The maximum strength of the along-channel velocity calculated by the model of approximately  $0.015 \text{ s}^{-1}$  is slightly smaller than the peak in the observations.

There are two major differences between model and observations. At first  $[\omega_x]$  peaks earlier already before slack tide in the observations (dashed red line figure 6.4a), whereas the model predicts maximum lateral circulation during high water (dashed red line figure 6.4a). Second the simulated data show a faster decrease of secondary circulation after high water, yielding even small negative values during ebb, in contrast to the observations, where  $[\omega_x]$  remains positive even during ebb tide.

If we now concentrate on the certain terms of equation (6.8), or in other words the driver for lateral circulation, predicted by the model and compare those to the estimates based on measurement data (see figure 6.4b), we find a striking agreement between simulation and observations, but also small differences.

The simulated across-channel buoyancy gradient  $[\omega_x]^b$  is all the time positive, larger during flood than during ebb, reaching its maximum magnitude during late flood (see solid blue line figure 6.4b). Both model and observations (dashed blue line figure 6.4b) agree nicely in overall strength, but there can be found also some disagreement. The strength of the lateral buoyancy gradient,  $[\omega_x]^b$ , is overpredicted by the model at low-water slack and generally underpredicted at the beginning of ebb.

The curvature forcing of lateral circulation,  $[\omega_x]^r$ , calculated by the model (solid red line) agrees to a large extend to the observation based estimates (dashed red line figure 6.4b). It is changing sign from positive values during flood to negative values during ebb, following a more or less sinusoidal shape, with a maximum amplitude of about  $1.5 \cdot 10^{-5} \text{ s}^{-2}$ .



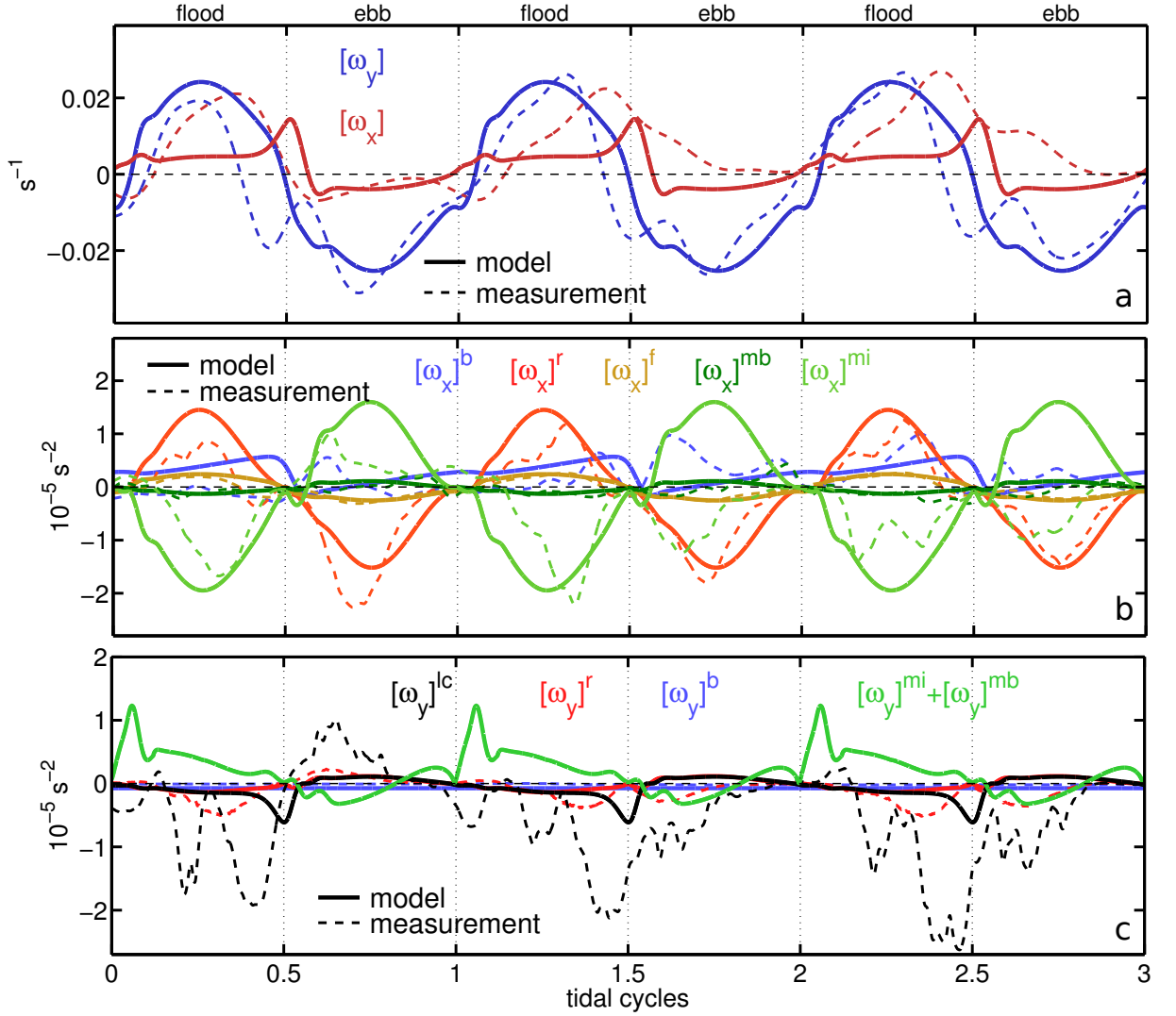


Figure 6.4.: Horizontal vorticity components. Panel (a) shows the along- (red) and across- (blue) channel component of the vorticity. The most important terms of the transport equation (6.8) of the along channel vorticity component (later circulation) are illustrated in panel (b). Correspondingly, panel (c) displays the most important terms of the  $\omega_y$ -equation (6.9). In each panel solid lines represent model data from setup Sp\_A.s\* and dashed lines the corresponding measurement data from station A (compare figure 5.8, 5.9, and 5.11). Note that the mixing term  $[\omega_y]^{mi} + [\omega_y]^{mb}$  appears in panel (c) only as a solid line, due to the fact that it is difficult to estimate from measurement data, as already discussed in section 5.5.3.

In contrast to the observations (dashed green line figure 6.4b), the simulated interfacial flux of lateral momentum (solid green line) is changing sign during the tidal cycle, simply mirroring the behavior of along-channel vorticity,  $[\omega_x]$  (solid red line figure 6.4a).

The remaining terms, Coriolis deflection (yellow lines figure 6.4b) and bottom friction (dark green lines figure 6.4b), are generally well reproduced by the model, but because of their minor dynamical impact, we do not discuss them further here.

### Longitudinal circulation

The along-channel circulation,  $[\omega_y]$  (blue lines figure 6.4a), is in principle well reproduced by the model. Given the fact that the amplitude of  $[\omega_y]$  is strongly determined by the along channel tidal currents, which are prescribed in the model as an external forcing agent, it is not surprising that the magnitude of the longitudinal circulation is captured well by the model. However, beside the amplitude some further common characteristics can be identified. The flood peak is rather short, since we find the zero crossing of  $[\omega_y]$  towards positive values significantly after low-water slack and back to negative values short before high water. This earlier zero crossing before high water slack happens in the model significantly later than in the observations. Nevertheless, we find for both model and observations a long and smeared out negative valley of longitudinal circulation during ebb.

The lateral circulation term,  $[\omega_y]^{lc}$ , in the equation for the along channel velocity (6.9), is smaller in magnitude in the simulated data than in the observation (black lines figure 6.4c). Nevertheless, it is still the most important term beside the two mixing terms.  $[\omega_y]^{lc}$  is small most of the time, peaking towards high water slack, together with lateral circulation (compare red lines figure 6.4a). All the other terms like buoyancy forcing,  $[\omega_y]^b$ , Coriolis forcing,  $[\omega_y]^f$ , and direct curvature forcing,  $[\omega_y]^r$  are small compared to mixing,  $[\omega_y]^{mi} + [\omega_y]^{mb}$ , and the lateral transport of along channel momentum,  $[\omega_y]^{lc}$ , and thus play only a minor role in the generation of estuarine circulation.

### 6.3.3. Discussion

The major conclusions made in chapter 5 that vertical stratification and estuarine circulation is mainly controlled by an interplay between curvature forcing and horizontal buoyancy gradients is confirmed by the model. As suggested during the discussion in chapter 5, asymmetric lateral circulation plays the major role in creating late flood stratification. Furthermore, it provides, due to  $[\omega_y]^{lc}$ , a key asymmetry in the along-channel circulation balance (6.9). It makes the across-channel vorticity,  $[\omega_y]$ , to change its sign already before high water slack, yielding a longer period with negative values of  $[\omega_y]$  (blue line figure 6.4a). Since a negative tidal average of  $[\omega_y]$  is identified with classical estuarine exchange flow, asymmetric lateral circulation appears to be a major source for estuarine circulation.

The model used here to reproduce the measurement data of chapter 5 is extremely simplified, nevertheless able to capture most of the major dynamics. This fact clearly confirms the hypothesis made in chapter 5 that curvature forcing and a constant along channel buoyancy gradient are able to generate most of the observed features.

The several mismatches mentioned above are on the one hand due to the limitations of the simple box-model and its basic configuration, excluding a lateral depth variation, a time dependent along channel buoyancy gradient, changing water levels, other tidal components than the  $M_2$ , and many other effects that likely influence a real world situation. On the other we should keep in mind that also the measurement based data provide only rough estimates that come along with many assumptions, for instance that the point measurements taken at station  $A$  are at least to some extent representative for the entire channel cross-section.<sup>8</sup>

If we look in detail on the disagreement between model and observations we find that the differences in lateral shear, are most likely due to complicated bathymetric features like the influence of a small gully joining the main channel during ebb (see figure 5.1), a different ebb and flood radius of curvature, and lateral depth variations. None of those effects is taken into account in the simple model setup, nevertheless its results are able to capture the major trend fairly well, given the fact that the *real-world* lateral shear is also just a rough estimate based on the difference of two point-measurements.<sup>9</sup> A consequence of the poorly reproduced lateral shear especially at the beginning of ebb (see figure 6.2), is a badly reproduced peak in the lateral buoyancy gradient also at the beginning of ebb (see blue line figure 6.4b). The resulting underestimated baroclinic pressure gradient is not able to balance curvature forcing as well as in reality, which finally yields the slight negative values of lateral circulation found during ebb in the modeled data in contrast to the observations (see red line figure 6.4a).

Another disagreement in lateral circulation, namely the circumstance that the peak of  $[\omega_x]$  appears significantly later in the simulation than in the observations (see red line figure 6.4a), seems to be due to the simple turbulence parametrization used for the model. The Munk and Anderson (1948) parametrization (see equations (6.20) and (6.21)) is known to underestimate the limiting effect of stratification on turbulence (see e.g. Dronkers (1996)). This explains the overestimate of vertical mixing during late flood (see green line figure 6.4b), which itself might explain the underestimate of lateral circulation in the second half of flood. The resulting delay in maximum lateral circulation yields a corresponding delay in vertical stratification (see figure 6.3a) and at the same time a delayed and underestimated peak in the lateral transport of along channel momentum,  $[\omega_y]^{lc}$ , for the  $[\omega_y]$ -balance (6.9) (see figure 6.4c).

If we take into account those complicated interdependencies, just briefly mentioned above, it is surprising how well this simple box-model is able to reproduce the dynamics in the Spiekeroog inlet. Especially given the fact that we have not done any parameter fine-tuning. From this astonishing ability of the model to capturing real world phenomena, we take some confidence that it could also be used to predict other situation associated with a different set of parameters.

<sup>8</sup>From figure 5.3e it becomes obvious that stratification at the northern station  $A$  occurs earlier and stronger than in the rest of the channel. Regarding this fact we can say that our findings represent the channel average quite well even in magnitude.

<sup>9</sup>Note that an overestimation of the lateral shear would also yield a corresponding overestimation of the lateral transport of along-channel momentum,  $[\omega_y]^{lc}$ .

## 6.4. Influence of channel shapes

The aim of this section is to clarify how the shape of a channel influences the dynamics. Based on a conceptual model we concluded in section 5.5.2 that the phenomenon of asymmetric lateral circulation is independent of the shape of the channel. To validate that hypothesis, which would make the findings above more relevant for all kind of curved channel, we perform an numerical experiment, where we change the shape from a  $S$ - to a  $U$ -shape curvature. Since all kind of channel shapes can be thought as a combination of  $U$ - and  $S$ -shape curves, the re-finding of asymmetric lateral circulation for  $U$ -shaped channels, would emphasise its possible relevance for many real world situations.

### 6.4.1. Model setups

In order to determine the influence of channel shapes we use three different setups. A setup SS\_bx1 representing a  $S$ -shaped channel. This setup is very similar to the validation setup Sp\_A\_s\*, used to compare to measurement data (see table 6.2). The only difference between both setups is in the neglecting of Earth's rotation. This further simplification is mainly done for tow reasons. First we want to reduce the number of free parameters, in order to make the setup more abstract, but thus also less specific, and second to eliminate a further tidal asymmetry associated with Earth's rotation, Thus the results are perfectly symmetric with respect to a change in sign of the radius of curvature,  $R_0$ .

The second setup US\_bx1 keeps all model parameters the same as SS\_bx1, except the shape of curvature, which is changed from  $S$ - to  $U$ -shape. As we are going to show in the following this change dramatically influences the dynamics of the system. Interestingly, if we increase at the same time the along-channel density gradient,  $\{\partial_x b\}$ , the results become more similar to the  $S$ -shaped channel again. This will be shown with the help of a third setup, US\_bx2, which is the same as US\_bx1, except for an increased longitudinal buoyancy gradient by a factor of two, yielding a Simpson number of,  $Si = 0.05$  (see table 6.2).

### 6.4.2. Results

#### Vertical stratification

Figure 6.5a illustrates the time evolution of the potential energy anomaly as a measure of vertical stratification for the three different model setups, each curve normalized by its particular maximum value,  $\Phi_{max}$  (see table 6.3).

The reference run SS\_bx1 with a  $S$ -shape curvature shows basically the same behavior like the *realistic* setup Sp\_A\_s\*, which is not surprising, given the fact that the only difference is in neglecting Earth's rotation (compare figure 6.3). We find peak stratification around high-water slack, with a maximum value of  $1 \text{ J m}^{-3}$ , and a smaller peak at low-water (see blue line figure 6.5a). Most of the tidal cycle the water column is well mixed.

If we now concentrate on the results of setup US\_bx1, with a  $U$ -shape curvature, we find substantial differences (see red line figure 6.5a). Maximum stratification is much smaller here, with about  $0.2 \text{ J m}^{-3}$  (see table 6.3), and occurs in contrast to SS\_bx1 at low-water slack. At High-water slack, we do not find any stratification at all. Furthermore, the

Exp-ID	$\Phi_{max}$ [J m <sup>-3</sup> ]	$\langle M_{SA} \rangle_{T_P}$	$Si_r$	$M_{lc}$ [cm s <sup>-1</sup> ]	$M_{ec}$ [cm s <sup>-1</sup> ]
SS_bx1	1.00	0.16	0.15	1.17	0.89
US_bx1	0.22	0.71	0.06	1.41	0.32
US_bx2	2.72	-0.18	0.50	1.69	1.78

Table 6.3.: Different parameters for comparing of  $U$ - and  $S$ -shaped channels.  $\Phi_{max}$  is the maximum potential energy anomaly reached in a tidal cycle.  $\langle M_{SA} \rangle_{T_P}$  denotes the tidal average of the straining anisotropy, where positive values indicate a dominating along-channel straining and negative values dominating lateral straining, respectively.  $Si_r$  is the curvature Simpson number, which is the average ratio of across-channel buoyancy gradient and curvature forcing in terms of production of lateral circulation.  $M_{lc}$  and  $M_{ec}$  are the measures for residual across- and along-channel circulation, respectively (see equations (6.27) and (6.27)).

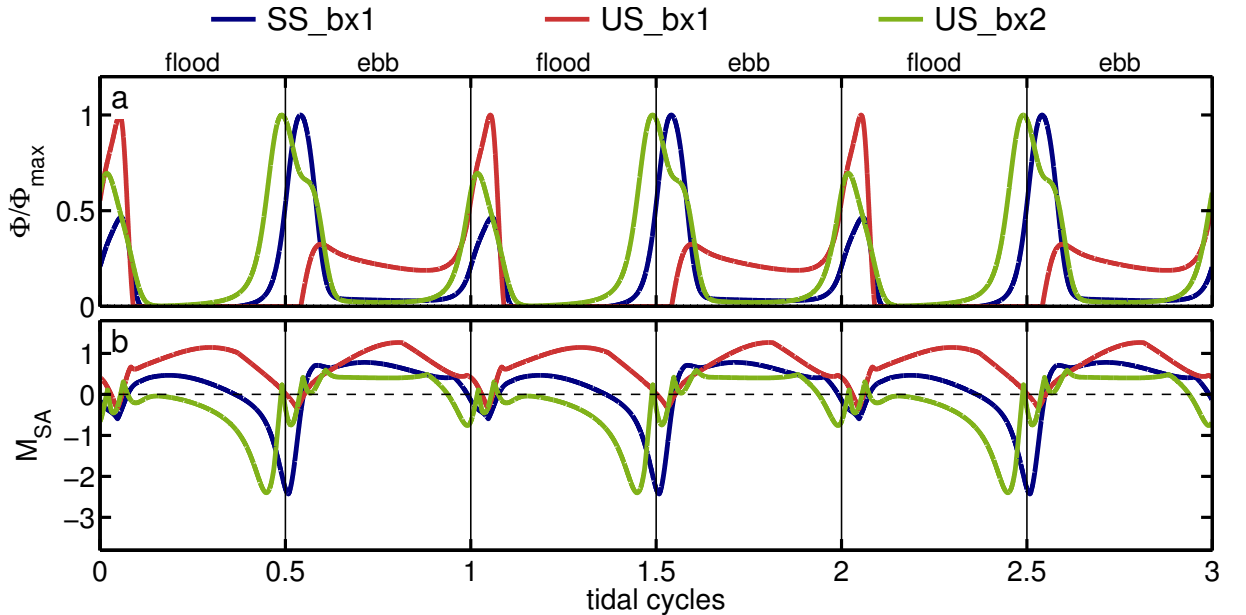


Figure 6.5.: Influence of channel shape on stratification. Panel (a) shows the normalized potential energy anomaly in time for three different model setups. The corresponding straining anisotropy,  $M_{SA}$  (see equation (6.24)), is illustrated in panel (b).

system keeps some small but constant stratification throughout the entire ebb-period. This behavior, of a well mixed flood and a slightly stratified ebb tide, is known to occur in association with classical along-channel tidal straining (Simpson et al., 1990).

Interestingly, if we increase the along-channel density gradient, which we do for setup US\_bx2, we find that the general behavior of the  $U$ -shape curve becomes more similar to that of the  $S$ -shape situation (compare blue and green line figure 6.5a). Peak stratification occurs around high-water slack, but this time substantially larger, with a maximum value of about  $2.7 \text{ J m}^{-3}$  (see table 6.3). Note that  $\Phi_{max}$  of setup US\_bx2 is more than ten times larger than for US\_bx1, although the along-channel density gradient is only increased by a factor of two. This clearly indicates a non-linear relation between along-channel and vertical gradient of the buoyancy.

We see from equation (6.10) that there are only two source terms of vertical stratification in the model, along-channel,  $[N^2]^{Sx}$ , and across-channel straining,  $[N^2]^{Sy}$ . The relative importance of both terms can be quantified by the straining anisotropy,  $M_{SA}$ , introduced in equation (6.24). The time evolution of  $M_{SA}$  is illustrated in figure 6.5b.

During ebb tide all setups show positive values of  $M_{SA}$ , indicating dominating along-channel straining. At this time the straining anisotropy is about twice as large for US\_bx1 as for the two other setups, which indicates that the small stratification observed at full ebb is likely caused by along-channel straining (compare figure 6.5a and b).

However, the major differences can be found at flood tide. The  $U$ -shape setup with the weak buoyancy gradient US\_bx1, is still governed by along-channel straining, whereas the two other setups shift towards a dominating lateral straining, indicated by the negative values of  $M_{SA}$  (see figure 6.5b). Both the  $S$ -shape case, SS\_bx1, as well as US\_bx2, show a strong negative peak of  $M_{SA}$  towards the end of flood, which are associated with a peak in vertical stratification, respectively (see figure 6.5). Thus, for the  $S$ -shape setup as well as for the  $U$ -shape setup with a stronger along-channel buoyancy gradient, US\_bx2, stratification is controlled by lateral straining, whereas the weak ebb-stratification occurring at setup US\_bx1 seems rather caused by along-channel straining.

Despite the large similarity of the time series of  $M_{SA}$  for SS\_bx1 and US\_bx2, there can be identified an important differences, the negative peak of  $M_{SA}$  appears for US\_bx2 significantly before slack tide, whereas  $M_{SA}$  reaches its minimum for SS\_bx1 not before high-water. Note that the low-water slack peak in potential energy anomaly coincides for all three cases with a lateral straining dominance (see figure 6.5b).

### Lateral circulation

As discussed in the previous section, for the  $S$ -shape channel (setup Ss\_bx1), lateral circulation,  $[\omega_x]$ , is positive throughout the entire flood tide, reaching its maximum towards high-water slack (see blue line figure 6.6a). During ebb tide  $[\omega_x]$  becomes slightly negative, nevertheless, we find significant asymmetric lateral circulation for setup SS\_bx1, yielding a residual lateral exchange flow of about  $M_{lc} = 1.2 \text{ cm s}^{-1}$  (see table 6.3).

Changing the channel shape, but keeping the longitudinal density gradient constant, yields a completely different picture (see red line figure 6.6a). Lateral circulation is small and positive most of the time except for low-water slack, where we find some negative lateral circulation for setup, US\_bx1. Interestingly, the small but persistent positive  $[\omega_x]$

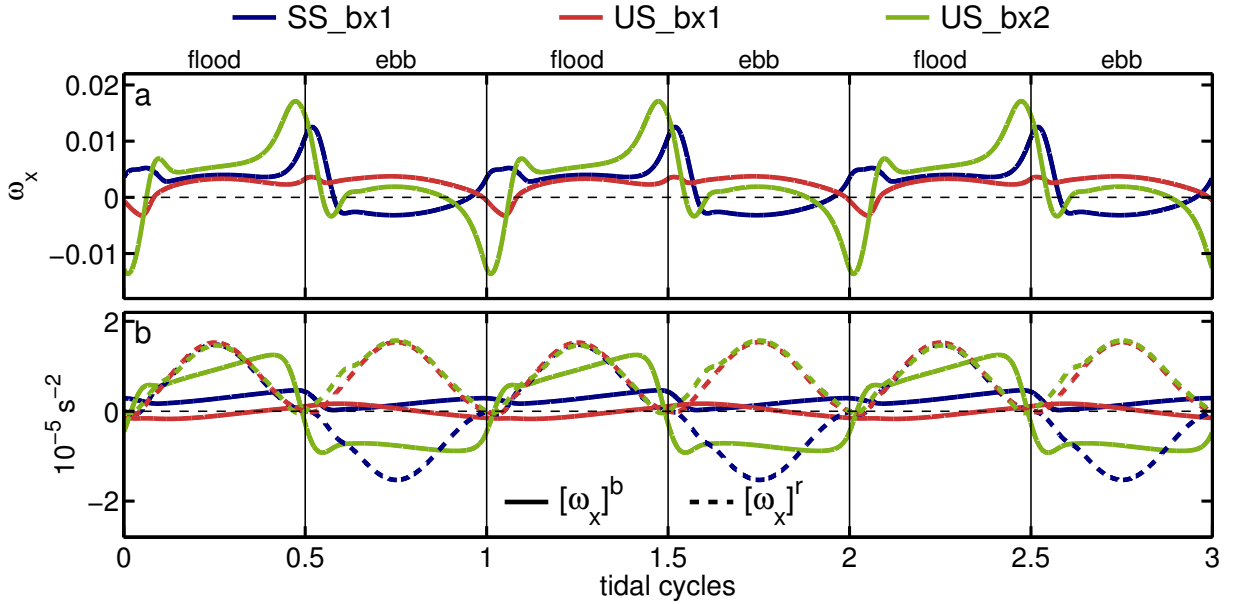


Figure 6.6.: Influence of channel shape on lateral circulation. Panel (a) shows the along channel vorticity  $[\omega_x]$  where the different colors correspond to the different model setups (see legend above). The two major creation terms of lateral circulation, namely baroclinic pressure forcing (solid lines),  $[\omega_x]^b$ , and curvature forcing (dashed lines),  $[\omega_x]^r$ , are displayed in panel (b), color-coded for each model run, respectively.

yields a net lateral exchange flow of  $M_{lc} \approx 1.4 \text{ cm s}^{-1}$  for US\_bx1, which is even slightly larger than for SS\_bx1 (see table 6.3).

Compared to US\_bx1, we find twice as large positive lateral circulation during flood for setup US\_bx2 (see green line figure 6.6a). Interestingly, the maximum of  $[\omega_x]$  is reached for US\_bx2 already before high-water. At slack tides  $[\omega_x]$  rapidly decrease to over shoot zero, yielding an oscillation like behavior. During most of the ebb tide  $[\omega_x]$  remains positive, only getting negative around low-water slack. US\_bx2 shows the largest asymmetry in  $[\omega_x]$  of all three setups, with an residual lateral circulation of  $M_{lc} = 1.7 \text{ cm s}^{-1}$  (see table 6.3).

Curvature forcing of lateral circulation,  $[\omega_x]^r$ , is basically the same for all three model setups (see dashed lines figure 6.6b), with the exception that it is mirrored to negative values during flood for the *S*-shaped channel (see blue dashed line figure 6.6b). The major difference in the lateral circulation forcing between the three setups is found in the behavior of buoyancy forcing,  $[\omega_x]^b$  (see solid lines figure 6.6b).

For US\_bx1, the *U*-shaped channel with the small along-channel buoyancy gradient,  $[\omega_x]^b$  remains small throughout the entire tidal cycle (see solid red line figure 6.6b). Therefore, the persistent positive  $[\omega_x]$  seem to be due to  $[\omega_x]^r$  only, which is not disturbed by the lateral buoyancy gradient.

In contrast to that, the *S*-shape setup delivers positive values of  $[\omega_x]^b$  for the entire cycle, significantly larger in magnitude than for US\_bx1 (compare red and blue solid lines in figure 6.6b).  $[\omega_x]^b$  increases for SS\_bx1 throughout the entire flood tide, to reach its maximum by the end of flood. After high-water slack  $[\omega_x]^b$  rapidly decreases to zero.

The lateral buoyancy gradient  $[\omega_x]^b$  for setup US\_bx2, shows a strong variability during

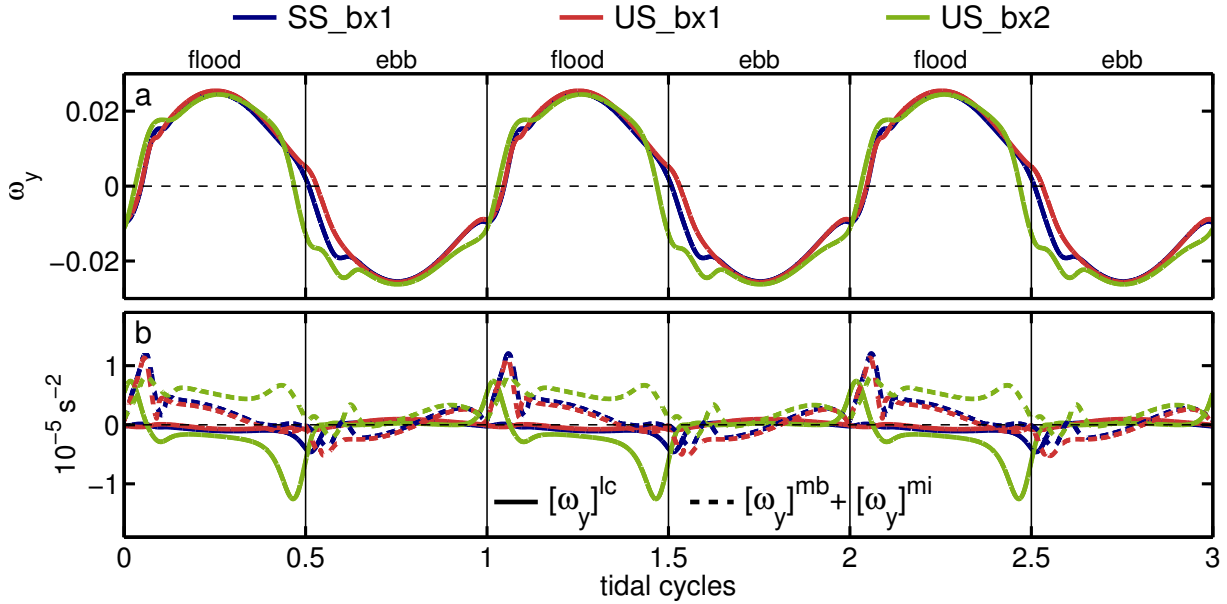


Figure 6.7.: Influence of channel-shape on longitudinal circulation. Panel (a) shows the time series of longitudinal circulation,  $[\omega_y]$ , for three different setups, respectively. The major driver of balance (6.9), for each setup respectively, are displayed in panel (b), namely lateral momentum transport,  $[\omega_y]^{lc}$ , interfacial mixing,  $[\omega_y]^{mi}$ , and bottom friction,  $[\omega_y]^{mb}$ . Taken independently,  $[\omega_y]^{mi}$  and  $[\omega_y]^{mb}$  would both be off-scale, but since they oppose each other most of the time, we show their sum here (dashed lines panel (b)).

a tidal cycle (see solid green line in figure 6.6b). Basically during the entire flood it is positive, increasing towards the end of flood to values above  $10^{-5} \text{ s}^{-2}$ . Thus, US\_bx2 is the only of the three setups, where the maximum  $[\omega_x]^b$  reaches a comparable magnitude as the maximum of curvature forcing,  $[\omega_x]^r$ . At high-water slack  $[\omega_x]^b$  rapidly decreases, over-shooting zero, to stabilize itself at a more or less constant negative level during ebb tide, which is in magnitude comparable to curvature forcing, but with a opposite sign. The over-shooting of  $[\omega_x]^b$  at slack tide, with a small rebound at the beginning of ebb, compares to the oscillatory behavior of  $[\omega_x]$ , where both curves seem to be phase shifted to each other by approximately  $\frac{1}{2}\pi$ .

### Longitudinal circulation

Figure 6.7a shows the across-channel vorticity, corresponding to longitudinal or along-channel circulation. In our definition  $[\omega_y]$  equals the vertical shear of the along-channel momentum, thus its signal is primarily caused by bottom friction acting on the along-channel tidal currents. Because of that  $[\omega_y]$  follows to a good approximation the sinusoidal behavior of  $\{u\}$  (see equation (6.23)). Since our main interest is in net across-channel vorticity, or in other words residual along-channel circulation, it rather makes sense to concentrate on the deviation from the general sinusoidal behavior of  $[\omega_y]$ , since a perfect sin-curve has no residual.



For the  $U$ -shaped case with a weak along-channel density gradient, US\_bx1 (see red line figure 6.7a), we do not find much asymmetry between ebb and flood. Although there is a small, phase-lack with respect to  $\{u\}$ ,<sup>10</sup> which per definition changes sign at slack, the negative phase of  $[\omega_y]$  is approximately as long as the positive phase, with comparable magnitudes, yielding only a tiny residual of  $M_{ec} = 0.32 \text{ cm s}^{-1}$  (see table 6.3). Since the lateral circulation driver,  $[\omega_y]^{lc}$ , is very small for US\_bx1 the entire cycle (solid red line figure 6.7b), and other drivers beside the interplay of bottom friction and interfacial mixing (dashed red line figure 6.7b) do not play a significant role,  $[\omega_y]$  can be thought as an undisturbed reference for the case US\_bx1 (see red line figure 6.7a).

If we look at the  $S$ -shape channel, SS\_bx1 (blue line figure 6.7a), we find a significant difference compared to US\_bx1.  $[\omega_y]$  is changing sign after flood much earlier for SS\_bx1 than for US\_bx1, not after but already at slack tide. This difference is clearly associated with the small peak in the lateral circulation driver,  $[\omega_y]^{lc}$ , at high-water slack for SS\_bx1 (solid blue line figure 6.7b). This earlier change in sign of  $[\omega_y]$  leads to a longer negative period, and thus to a significantly larger residual of approximately  $M_{ec} = 0.89 \text{ cm s}^{-1}$ , which is more than five times as much as for the  $U$ -shape run US\_bx1 (see table 6.3).

However, when we look at the green line in figure 6.7a, we see that significant asymmetry in  $[\omega_y]$  can also be found for a  $U$ -shape channel, simply by increasing the along-channel density gradient. For US\_bx2 the across-channel vorticity changes sign even earlier to negative values than for SS\_bx1, already significantly before slack tide. This sign change is associated with a strong negative peak in  $[\omega_y]^{lc}$ , too (solid green line figure 6.7b). For US\_bx2 the negative peak of  $[\omega_y]^{lc}$  is significantly larger and occurs earlier than for SS\_bx1 (compare solid blue and green line figure 6.7b). The negative period of  $[\omega_y]$  is therefore even longer for US\_bx2, yielding a residual along-channel exchange of  $M_{ec} = 1.78 \text{ cm s}^{-1}$  (see table 6.3).

Interestingly, we find that an increase of the along-channel density gradient by a factor of two for the  $U$ -shaped channel, yields an increase in net-exchange flow by a factor of five, indicating a strongly non-linear relation between estuarine circulation and along-channel buoyancy gradient (compare  $M_{ec}$  for US\_bx1 and US\_bx2 table 6.3).

### 6.4.3. Discussion

#### Interplay of curvature and buoyancy forcing

As discussed earlier for the  $S$ -shape case, SS\_bx1, we find a characteristic interplay of curvature forcing,  $[\omega_x]^r$ , and lateral buoyancy gradient,  $[\omega_x]^b$  (compare blue lines figure 6.6b). While  $[\omega_x]^r$  is changing sign from ebb to flood, together with the radius of curvature  $R$ ,  $[\omega_x]^b$  remains positive throughout the entire tidal cycle. Thus the opposite sign of both terms during ebb, yields only small lateral circulation. In contrast to that, the contribu-

<sup>10</sup>The phase-lack is likely due to the simple turbulence parametrization, which considers instantaneous bottom friction as the only source of turbulence. Since bottom friction is small at slack tide, there is not enough mixing in order to destroy the remaining vertical shear. A more sophisticated turbulence model including convective mixing and vertical shear as additional sources of turbulence as well as a proper differential equation for the turbulent kinetic energy, allowing for a smooth and not sudden decay of turbulence, as soon as the source terms go down, would properly lead to a different result. This might also explain the small bump in the curve of  $[\omega_y]$  at slack tides.

tions of both terms add up during flood, leading to significant lateral circulation, especially by the end of flood, when vertical mixing becomes small. Nevertheless, the small curvature Simpson number  $Si_r = 0.15$  (see table 6.3), indicates an overall dominating curvature forcing, which yields the slightly negative values of  $[\omega_x]$  during ebb.

For the  $U$ -shape curve with a small along-channel density gradient, US\_bx1, the situation appears different.  $[\omega_x]^b$  is much smaller than  $[\omega_x]^r$ . With a curvature Simpson number of about  $Si_r = 0.06$ ,  $[\omega_x]^r$  is completely dominating over the lateral buoyancy gradient. Since curvature forcing is always positive for the  $U$ -shape channel, we obtain the small but persistent positive lateral circulation for US\_bx1, yielding a residual lateral exchange that is even slightly larger than for SS\_bx1.

The circumstance that  $[\omega_x]^b$  is significantly smaller in magnitude for US\_bx1 compared to SS\_bx1, is likely caused by the fact that differential advection,  $[\partial_y b]^{da}$  (see equation (6.12)), changes sign from flood to ebb for the  $U$ -shape channel, whereas it acts the entire tidal cycle in the same direction for the  $S$ -shape channel. Therefore, we find that the small  $[\omega_x]^b$  build up during ebb, slightly decreases again during flood for US\_bx1, whereas it further increases during flood for setup SS\_bx1 (compare blue and red solid lines figure 6.6b)). Thus by the end of flood, we find a significant larger lateral buoyancy gradient  $[\omega_x]^b$  for the  $S$ -shape channel than for setup US\_bx1. In contrast to the  $U$ -shape channel the larger lateral baroclinic pressure gradient in setup SS\_bx1 is able to generate strong lateral circulation at high-water slack.

However, if we increase the along-channel buoyancy gradient (setup US\_bx2), and thus the differential advection term,  $[\partial_y b]^{da}$  (see equation (6.12)), the picture changes substantially for the  $U$ -shape channel. Both terms  $[\omega_x]^b$  and  $[\omega_x]^r$  are of comparable order of magnitude, with a curvature Simpson number of  $Si_r = 0.5$ . While  $[\omega_x]^r$  remains positive the entire tidal cycle,  $[\omega_x]^b$  is changing sign, yielding pronounced lateral circulation during flood and vanishing lateral circulation during ebb. However, at low-water slack  $[\omega_x]^b$  is still strong enough to generate, in the absence of vertical mixing, substantial lateral circulation. This lateral circulation rapidly decreases  $[\omega_x]^b$  at low water via  $[\partial_y b]^{N2}$  (see equation (6.12)) for setup US\_bx2), and yields even an over shooting of  $[\omega_x]^b$  towards positive values shortly after slack tide.

### Positive Feedback loop during flood

Starting already from a positive lateral buoyancy gradient,  $[\omega_x]^b$ , shortly after low water slack, the following flood tide with a different sign for the differential advection term  $[\partial_y b]^{da}$ , is able to rapidly generate a strong positive lateral buoyancy gradient for setup US\_bx2 (see green line figure 6.6b). Now,  $[\omega_x]^b$  and  $[\omega_x]^r$  point in the same direction with comparable magnitudes during flood. Together they are able to generate some significant lateral circulation already during full flood, although vertical mixing is still strong. This substantial lateral circulation during full flood on the other hand yields a further increase in lateral shear,  $[\partial_y u]$ , via  $[\partial_y u]^{lc}$  (see equation 6.13). This enhanced lateral shear leads now to enhanced differential advection,  $[\partial_y b]^{da}$ , which itself generates a stronger lateral buoyancy gradient,  $[\omega_x]^b$ . Thus we find a positive feedback loop here during flood for setup US\_bx2, that has several consequences.

The feedback loop generates a strong lateral buoyancy gradient already at full flood, which together with curvature forcing,  $[\omega_x]^r$ , yields large lateral circulation. This lateral

circulation comes along with strong lateral straining,  $[N^2]^{Sy}$ , which generates vertical stratification already before high-water slack. This stratification on the other hand leads now in combination with lateral circulation to a destruction of  $[\omega_x]^b$  via  $[\partial_y b]^{N^2}$ , which is why the lateral buoyancy gradient is rather small at high water slack for US\_bx2, in contrast too setup SS\_bx1.

Thus we find a positive feedback loop during flood between,  $[\omega_x]^b$ ,  $[\omega_x]$  and  $[\partial_y u]$ . This feedback loop comes to an end as soon as vertical stratification becomes large enough to shut-down the lateral buoyancy gradient, via  $[\partial_y b]^{N^2}$ , and thus the driving force for lateral circulation by the end of flood.<sup>11</sup>

### Lateral internal seiche at slack tide

The shut-down of the feedback loop around high-water slack, for setup US\_bx2, is so rapid that the lateral buoyancy gradient,  $[\omega_x]^b$ , over shoots zero to negative values, resulting in a oscillation like behavior of  $[\omega_x]$  and  $[\omega_x]^b$  at slack tide for US\_bx2.

The oscillatory behavior can be understood as an internal lateral seiche<sup>12</sup>, occurring around slack, where mixing due to the absence of tidal currents is weak, and vertical stratification is strongest. The large lateral buoyancy gradient build up during flood, drives strong lateral circulation, that relaxes  $[\partial_y b]$  via  $[\partial_y b]^{N^2}$ . After  $[\partial_y b]$  is completely destroyed,  $[\omega_x]$  is still not zero, thus  $[\partial_y b]^{N^2}$  acts now as a source of  $[\partial_y b]$ , but now in such a way that it decelerates  $[\omega_x]$ .

As soon as lateral circulation stops, the opposed lateral buoyancy gradient is able to again relax itself generating  $[\omega_x]$  in the opposite sense, which again changes the sign of  $[\partial_y b]$  and so on. This seiche-like phenomena comes to an end as soon as tidal currents become strong enough to destroy vertical stratification, suppress lateral circulation and thus finally make differential advection,  $[\partial_y b]^{N^2}$ , again dominate over lateral relaxation,  $[\partial_y b]^{N^2}$ , in terms of balance (6.12). (for details see discussion 6.5.3).

### Difference between *S*- and *U*-shape channels

A major difference between a *S*- and a *U*-shape channel can be found in the differential advection term,  $[\partial_y b]^{da}$  (see balance (6.12)), which changes sign from ebb to flood for a *U*-shape channel, in contrast to a *S*-shaped channel, where it basically keeps its orientation the entire tidal cycle. As a consequence the effective time provided to build up a decent lateral buoyancy gradient,  $[\partial_y b]$ , is longer for a *S*-shape channel than for a *U*-shape channel. Therefore, the resulting lateral buoyancy gradient for setup SS\_bx1 is significantly larger in magnitude than for setup US\_bx1 by the end of flood (see solid lines figure 6.6b). Thus for comparable along-channel density gradients, it is more likely to find significant lateral circulation by the end of flood for a *S*- compared to a *U*-shaped channel.

However, the general relation between curvature forcing,  $[\omega_x]^r$ , and lateral buoyancy gradient,  $[\omega_x]^b$ , is independent of the shape of the channel. In any case both terms oppose

<sup>11</sup>A detailed discussion of the feedback loop can be found in section 6.5.3.

<sup>12</sup>An internal seiche is a standing baroclinic wave, whose wave length corresponds to the geometry of the system. Such waves are a well known phenomenon in stratified basins like lakes for instance (e.g. Becherer and Umlauf (2011)).

each other during ebb and enhance each other during flood.<sup>13</sup> This is due to the fact that  $[\omega_x]^b$  changes sign from flood to ebb, whereas  $[\omega_x]^r$  keeps its orientation for a  $U$ -shape curve and vice versa for a  $S$ -shape curve (review discussion section 5.5.2).

Therefore, both  $S$ - and  $U$ -shape channels are able to activate the positive feedback loop, between differential advection and lateral circulation, which causes strong lateral circulation and vertical stratification during flood.

### Longitudinal circulation

Compared to the more or less undisturbed case US\_bx1, where mainly the interplay of vertical mixing and bottom friction determines the longitudinal circulation,  $[\omega_y]$ , we find a pronounced asymmetry in  $[\omega_y]$  between flood and ebb for SS\_bx1 and even more for US\_bx2. This asymmetry is clearly associated with a strong contribution of lateral circulation,  $[\omega_y]^{lc}$ , to the balance (6.9). The strong negative peak of  $[\omega_y]^{lc}$ , yields a significantly earlier zero-crossing of  $[\omega_y]$  by the end of flood and thus to a longer negative period. Since a negative tidal mean of the across-channel vorticity,  $[\omega_y]$ , corresponds to classical estuarine circulation, we find that lateral circulation by the end of flood is the major driver of estuarine circulation at least for setup SS\_bx1 and US\_bx2.

Setup US\_bx1 and US\_bx2 differ only by an increase of the along-channel buoyancy gradient by a factor of two, nevertheless, we find a five times larger along-channel exchange flow for setup US\_bx2 compared to setup US\_bx1. This indicates a non-linear relation between the along-channel density gradient and estuarine circulation. Our findings above show that the feedback loop at flood tide might be responsible for this large difference in estuarine exchange flow. For setup US\_bx1 the along-channel buoyancy gradient is too weak to activate the feedback loop in contrast to US\_bx2. This suggests that there is a critical threshold of  $\{\partial_x b\}$ , which needs to be exceeded in order to activate the positive feedback during flood tide. There seems to be also a connection to the seiche-like phenomenon at slack tide, yielding an oscillatory behavior of  $[\partial_y b]$ , proving different initial starting conditions for the differential advection of the along-channel gradient during flood and ebb tide respectively. Thus the criteria for activating the feedback loop during flood, might be related to a minimum stratification necessary at low water slack tide to activate the lateral seiche, which then yields the sign change of  $[\partial_y b]$ .

## 6.5. Parameter study

### 6.5.1. Model setup

In order to further investigate the parameter space for a  $u$ -shaped channel, we perform an additional experiment, where we are interested in the sensitivity of the model regarding the Simpson number,  $Si$ . To this end we vary  $Si$  from 0 to 0.14, simply by increasing the longitudinal buoyancy gradient,  $\{\partial_x b\}$ , in small steps while keeping the water depth,  $H_0$ , and the tidal velocity amplitude,  $u_a$ , constant. As a step size for the Simpson number we

---

<sup>13</sup>This is only true, if the along-channel density gradient is large enough. US\_bx1 is an example, where  $\{\partial_x b\}$  is too small to have a substantial dynamical impact.

use  $\Delta\text{Si} = 0.003$ , which guarantees a sufficient high resolution in order to resolve non-linear transitions.

Since the major focus of this study lies on the interplay of curvature and buoyancy forcing, another important parameter to look at, besides the longitudinal buoyancy gradient,  $\{\partial_x b\}$ , is the radius of curvature,  $R$ . Thus we performed three similar experiments with the same resolution in Si for three different radii of curvature, 2, 4, and 8 km (see Si\_R2, Si\_R4, and Si\_R8 table 6.2). Note that here in contrast to the former experiments the radius of curvature has a positive sign, corresponding to clock-wise flood currents. As mentioned above due to the neglecting of Earth's rotation, the results are perfectly symmetric.<sup>14</sup>

## 6.5.2. Results

### Vertical stratification

The stratification characteristics of the three setups Si\_R2, Si\_R4, and Si\_R8 are illustrated in the left column of figure 6.8. The maximum potential energy anomaly reached within a tidal cycle<sup>15</sup> provides a proper scale for the overall strength of vertical stratification for a given parameter set. For all three radii of curvature  $\Phi_{max}$  is very small at small Simpson numbers (figure 6.8a).  $\Phi_{max}$  stays below  $1 \text{ J m}^{-3}$  until it reaches a particular Simpson number,  $\text{Si}_c$ , where it suddenly jumps towards larger values of more than  $2 \text{ J m}^{-3}$ .

This sudden jump occurs for all three radii at different Simpson numbers. For  $R = 2 \text{ km}$  the critical Simpson number is  $\text{Si}_c = 0.027$ , for  $R = 4 \text{ km}$  it is  $\text{Si}_c = 0.037$ , and for  $R = 8 \text{ km}$  it is  $\text{Si}_c = 0.048$ , thus the critical Simpson number increases with an increasing radius of curvature (see colored vertical lines figure 6.8). Although the three scenarios (Si\_R2, Si\_R4, and Si\_R8) jump at different Si they all show comparable values of  $\Phi_{max}$  after the jump.

Besides, the magnitude of vertical stratification, its duration is an important quantity, in order to determine which fraction of each tidal cycle is under the influence of vertical stratification. The *well-mixed* parameter,  $P_{wm}$ , measures which percentage of each cycle is characterized by a gradient Richardson numbers below a quarter (see definition (6.25)), and thus assumingly unaffected by vertical stratification. We find for all three scenarios an entirely well-mixed tidal cycle for very small Simpson numbers, decreasing with increasing Si to about 90% well-mixed conditions short before the jump (figure 6.8b). At the critical Simpson number,  $\text{Si}_c$ ,  $P_{wm}$  suddenly decreases towards values significantly below 0.8. Thus  $\text{Si}_c$  marks a sudden shift from a well-mixed towards a partially stratified regime.

Associated with that sudden regime shift is a change in the relative importance of the source terms of vertical stratification, which can be seen from figure 6.8c. The straining anisotropy,  $M_{SA}$ , quantifies the relative importance of along- and across-channel straining for the production of vertical stratification (see (6.10) and (6.24)). Figure 6.8c displays the tidal mean of the straining anisotropy. Before the jump  $\langle M_{SA} \rangle_{T_p}$  is significantly positive for all three scenarios, indicating a clear dominance of along-channel straining. After the jump we observe negative values for Si\_R2 and Si\_R4 and values around zero for Si\_R8. Thus the

<sup>14</sup>Note that *symmetric* means an opposite sign for the stream-wise vorticity  $[\omega_x]$ .

<sup>15</sup>Every time, when we talk about a tidal cycle in this chapter it actually means the particular periodicity of the signal (visit appendix A.5 for more information)

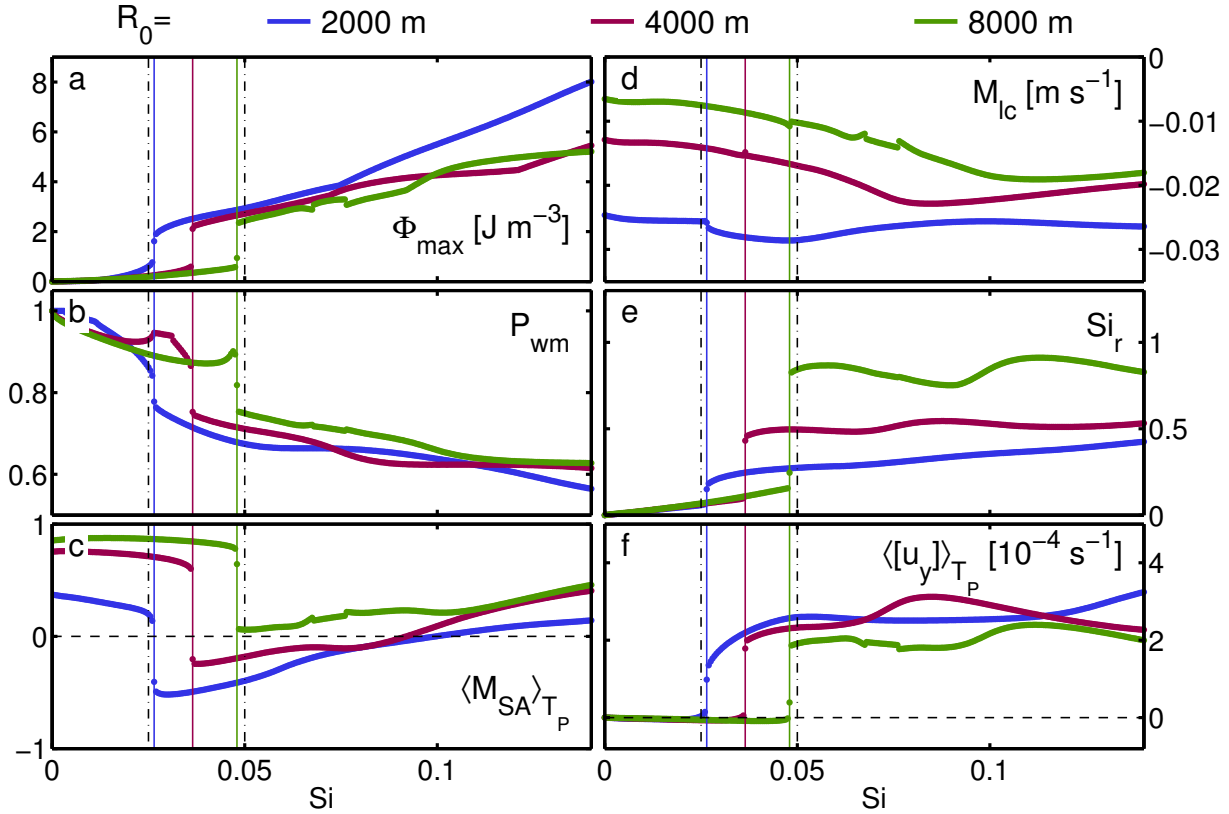


Figure 6.8.: Stratification and lateral circulation characteristics of the experiments Si\_R2 (blue), Si\_R4 (red), and Si\_R8 (green). Parameters associated with vertical stratification are displayed in the left column, where panel (a) shows the maximum potential energy anomaly,  $\Phi_{max}$ , reached during a period of the signal (usually a tidal cycle, see appendix A.5), panel (b) the *well-mixed* parameter  $P_{wm}$  (see (6.25)), and panel (c) the tidally averaged straining anisotropy  $\langle M_{SA} \rangle_{T_P}$  (see equation (6.24)). The right column displays parameters associated with lateral circulation, where panel (d) shows the lateral circulation measure,  $M_{lc}$ , according to equation (6.27), panel (e) the curvature Simpson number calculated according to (6.28), and panel (f) the tidally average lateral shear. The vertical dashed lines appearing in each panel correspond to the parameter position of setup US\_bx1 and US\_bx2, respectively. The colored vertical lines mark the sudden phase transition for each radius of curvature, respectively.

sudden regime shift from well-mixed to partially stratified conditions is associated with a shift from along-channel towards an across-channel straining dominance, at least for sufficient small radii of curvature. Although lateral straining is not entirely dominating vertical stratification after the jump for Si\_bx8, it is suddenly of equal importance as along-channel straining, indicated by  $\langle M_{SA} \rangle_{T_p} \approx 0$ .

### Lateral circulation

The circumstance that lateral straining after the jump is not as dominant for Si\_R8 as for Si\_R2 is not very surprising given fact that the underlying lateral circulation is to a large fraction due to curvature forcing, which increases with decreasing radius of curvature. Thus we find also substantially more residual lateral circulation for scenario Si\_R2 than for Si\_R8 (figure 6.8d).<sup>16</sup> For scenario Si\_R8  $M_{lc}$  decreases from  $-0.6 \text{ cm s}^{-1}$  at small Simpson numbers to about  $-2 \text{ cm s}^{-1}$  at  $\text{Si} = 0.14$ . Starting from slightly smaller values of  $-1.2 \text{ cm s}^{-1}$  at no-buoyancy conditions,  $M_{lc}$  decreases for Si\_R4 with increasing Simpson numbers to comparable values as for Si\_R8. In contrast to that we find already substantial negative residual lateral circulation in the absence of any buoyancy gradients ( $\text{Si} = 0$ ) of about  $M_{lc} \approx -2.5 \text{ cm s}^{-1}$  for scenario Si\_R2, staying more or less constant with increasing Si.

Interestingly, we do not find the strong discontinuity (jump) that we found for the other quantities in the average lateral circulation, but in fact the curves of  $M_{lc}$  rather smoothly pass the critical Simpson numbers ( $\text{Si}_c$  is marked by the colored vertical lines in figure 6.8e). This is a very surprising find given the fact that the relative importance of the major drivers for lateral circulation changes dramatically, which can be seen from the curvature Simpson number,  $\text{Si}_r$ .

According to its definition (6.28),  $\text{Si}_r$  measures on the one hand the relative importance of the lateral baroclinic pressure gradient and centrifugal forcing in terms of the generation of lateral circulation and on the other hand the tidally averaged magnitude of the lateral buoyancy gradient. We find that  $\text{Si}_r$  in fact does perform a significant jump at the critical Simpson number (figure 6.8e). The circumstance that the jump is actually stronger for Si\_R8 than for Si\_R2 is not surprising given the fact that  $\text{Si}_r$  is directly proportional to the radius of curvature.

Before the discontinuity we find  $\text{Si}_r$  to be very small for all three scenarios, indicating a purely curvature governed lateral circulation (figure 6.8e). However, as soon as the critical Simpson number is reached,  $\text{Si}_r$  performs a jump, reflecting a significantly larger influence of the lateral buoyancy gradient on the generation of lateral circulation. For the case of  $R = 8 \text{ km}$  we find curvature Simpson numbers of the order of unity after the discontinuity, indicating an equal importance of buoyancy and curvature forcing. For the case Si\_R4 we only find about  $\text{Si}_r = 0.5$  after the jump and for Si\_R2 even less, indicating a relatively smaller contribution of the lateral buoyancy gradient to the overall generation of lateral

<sup>16</sup>Note that the negative values of  $M_{lc}$  indicate a tidal asymmetry towards negative values of  $[\omega_x]$ . This is in contrast to the findings above, for instance for setup US\_bx2 (see table 6.3), where we found a positive residual for the lateral circulation. The reason is in the opposite sign of the radius of curvature here compared to setups US\_bx1 and US\_bx2 (see table 6.2), yielding an opposite directed lateral circulation, but perfectly the same results for along-channel circulation and vertical stratification, since we excluded all possible symmetry breaking forces, as e.g. Earth's rotation.

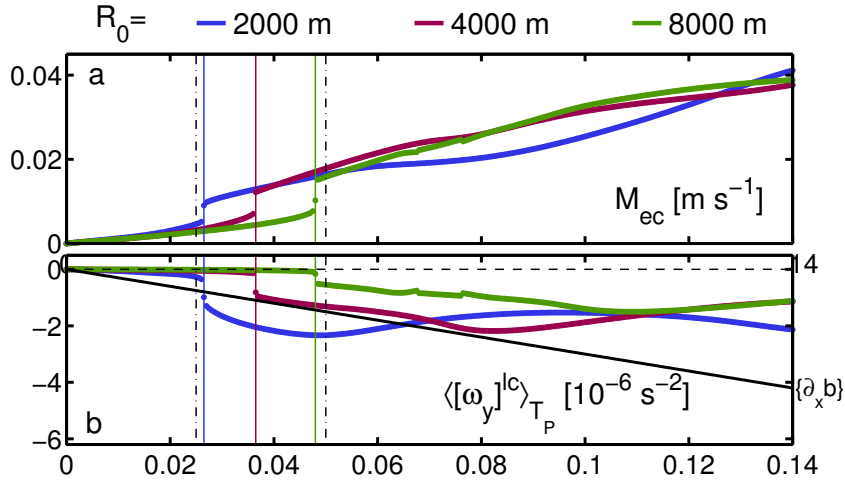


Figure 6.9.: Estuarine circulation characteristics of the experiments Si\_R2 (blue), Si\_R4 (red), and Si\_R8 (green). Similar like figure 6.8. Here panel (a) displays the estuarine circulation measure,  $M_{ec}$ , according to equation (6.26) and panel (b) the tidal average of the estuarine circulation driver associated with lateral circulation,  $\langle [\omega_y]^{lc} \rangle_{T_p}$ . In addition to  $\langle [\omega_y]^{lc} \rangle_{T_p}$  panel (b) shows the longitudinal buoyancy gradient  $\{\partial_x b\}$  in black.

circulation. Nevertheless,  $Si_r \approx 0.3$  after the jump for Si\_R2 correspond to an absolute larger average magnitude of the lateral buoyancy gradient than  $Si_r \approx 0.8$  for Si\_R8, given the fact that curvature forcing is about four times as large for Si\_R2 than for Si\_R8.

In association with the sudden jump of the relative importance of  $[\omega_x]^b$  compared to  $[\omega_x]^r$ , we find a dramatic increase in the tidal average of the lateral shear,  $\langle \partial_y u \rangle_{T_p}$  (figure 6.8f). Before the discontinuity  $\langle \partial_y u \rangle_{T_p}$  is neglectible, but then it suddenly jumps towards  $\langle \partial_y u \rangle_{T_p} \approx 2 \cdot 10^{-4} \text{ s}^{-1}$ , where it approximately stays for the rest of the displayed parameter range. Interestingly, the strength of the residual horizontal circulation ( $\langle [\omega_z] \rangle_{T_p} = \langle [\partial_y u] \rangle_{T_p}$ ) seems to be independent of the radius of curvature, since all three scenarios have a more or less constant net lateral shear after the jump of about  $2 \cdot 10^{-4} \text{ s}^{-1}$ .

### Longitudinal circulation

The magnitude of the residual along-channel estuarine circulation, here measured by  $M_{ec}$ , is fairly weak, less than  $0.5 \text{ cm s}^{-1}$ , before the discontinuity<sup>17</sup> for all of the three different curvatures (figure 6.9a). Afterwards it suddenly jumps to values greater than  $1 \text{ cm s}^{-1}$ , to linearly increase further with an increasing Simpson number.

Earlier we identified the lateral transport of along-channel momentum to be a major source of net estuarine circulation. The tidal mean of that quantity is displayed in figure 6.9b. Before the discontinuity, we find for all three scenarios no significant influence of lateral circulation on the estuarine exchange flow, since the magnitude of  $\langle [\omega_y]^{lc} \rangle_{T_p}$  is close to zero, but more importantly much smaller than the along-channel buoyancy gradient,

<sup>17</sup>Before the discontinuity means here and after at Simpson numbers below the critical Simpson number,  $Si_c$ , where the discontinuous jump occurs.



$\{\partial_x b\}$  (black line figure 6.9b).

After the jump  $\langle[\omega_y]^{lc}\rangle_{T_p}$  substantially increases, to become one of the most important drivers for residual estuarine circulation. In case of Si\_R2 it is in average about twice as large as  $\{\partial_x b\}$ , with values up to  $2.5 \cdot 10^{-6} \text{ s}^{-2}$ , whereas for Si\_R4  $\langle[\omega_y]^{lc}\rangle_{T_p}$  is of comparable magnitude as  $\{\partial_x b\}$ , and for Si\_R8 it is even substantially smaller. Interestingly, for Simpson numbers above 0.1 all three curves converge to values between 1 and  $2 \cdot 10^{-6} \text{ s}^{-2}$ . Nevertheless, it should be recalled that  $\{\partial_x b\}$  is per definition the same for the entire tidal cycle, whereas  $[\omega_y]^{lc}$  peaks around high water slack, where vertical mixing is small, and thus might have a more significant effect on  $M_{ec}$  than persistent longitudinal buoyancy forcing.

### 6.5.3. Discussion

#### Sudden phase transition

One of the most surprising results of the experiments Si\_R2, Si\_R4, and Si\_R8 is the sudden regime shift at the critical Simpson number,  $Si_c$ . The phase transition happens so rapidly that it appears as a discontinuity in the data shown above, although we used a fairly high resolution in the Si-space of  $\Delta Si = 0.003$ . Nevertheless, if we would further increase the resolution it would be possible to resolve the jump, such that we obtain a sudden, but smooth transition between the different regimes (not shown here).

When we look more in detail on the data, we actually find a number of discontinuities, especially for Si\_R8 (see for instance figure 6.8d), but none of those is associated with such a substantial change in most of the important parameters, as the one occurring at  $Si_c$ . In fact the change is so dramatic that we can easily call it a regime shift or a phase transition, in analogy to phase transitions occurring in thermodynamics, like the change from ice to liquid water, or from water to vapor. In our model results the discontinuity does not indicate a change in the molecular binding characteristics of a fluid, but it rather marks a dynamical regime transition in an estuary.

This regime shift effects a number of crucial parameters, like for instance vertical stratification. As we found out based on figure 6.8 the system is basically well-mixed before the jump and partially stratified afterwards. Therefore, one particular aspect of the phase jump is that it marks a sudden regime shift from a well-mixed to a partially stratified estuary. A better understanding of the quick transition might provide some new insights into the common distinction between those two types of estuaries.

Another aspect of the regime shift is the change from dominating longitudinal to lateral dynamics, as can be seen for instance from the tidal mean of the straining anisotropy,  $\langle M_{SA} \rangle_{T_p}$ , which suddenly changes from positive to negative, indicating dominating lateral straining after the discontinuity (figure 6.8c).

Interestingly, we do not find a sudden increase in the average lateral circulation, which passes the critical Simpson number rather smoothly. This is a very surprising result, given the fact that every thing related to lateral circulation changes dramatically except its average value. One of its source terms  $[\omega_x]^b$  increases strongly in magnitude, becoming one of the major drivers, which is mirrored in the sudden increase of  $Si_r$ . Before the discontinuity,  $[\omega_x]$  is entirely governed by centrifugal force, whereas afterwards it is influenced to a large extent by the lateral buoyancy gradient.

In the previous section, we have seen that this shift in the relative importance of the drivers is also associated with a substantially different temporal evolution of  $[\omega_x]$  (compare green and red line figure 6.6a). Before the jump (US\_bx1)  $[\omega_x]$  is small but oriented in the same direction the entire tidal cycle. Conversely, after the jump (US\_bx2),  $[\omega_x]$  is large during flood and small at ebb tide.

Associated with the regime shift in the generation processes of lateral circulation is a shift in its consequences. We find a sudden increase in vertical stratification due to lateral straining, a dramatic increase in residual lateral shear<sup>18</sup>, and most importantly a substantial increase in residual estuarine circulation caused by lateral circulation. The later is due to the fact that the persistent but small lateral circulation before the jump, which is simply caused by centrifugal forces, does not generate a residual lateral shear (see discussion in chapter 3). Since lateral and vertical circulation ( $[\partial_y u]$ ) need to be oriented in the same direction in order to generate residual estuarine circulation (see  $[\omega_y]^{lc}$  equation (6.9)), the centrifugal force dominated situation before the jump is not able to generate substantial residual along-channel circulation. After the discontinuity on the other hand, the lateral buoyancy gradient provides an additional symmetry breaking of  $[\partial_y u]^{lc}$ , necessary to orient  $[\partial_y u]$  and  $[\omega_x]$  is the same direction at ebb and flood, respectively.

Considering all those facts, it appears like a miracle that the tidal mean of  $[\omega_x]$  is not changing dramatically at the discontinuity. It seems as if, the more the asymmetric interplay of lateral buoyancy gradient and centrifugal forcing amplifies lateral circulation during flood the more it reduces lateral circulation during ebb. Thus residual lateral circulation does not provide a proper indicator, for its asymmetric interaction with the other vorticity components.

The fact that the regime transition occurs that quickly and dramatically, might originate in a particular characteristic of the asymmetrical interplay of curvature and buoyancy forcing. As we mentioned earlier, we can identify a positive feedback loop between buoyancy forcing and lateral circulation in our model equations, which can be activated at flood tide.<sup>19</sup>

### Positive feedback loop

Figure 6.10 provides a conceptual sketch of the feedback loop. At the beginning of flood tide we find a negative across-channel vorticity,  $[\omega_y]$ , simply due to bottom friction acting on the mean tidal current. In combination with a curved channel that across-channel vorticity is transformed, via centrifugal forcing,  $[\omega_x]^r$ , into stream-wise vorticity,  $[\omega_x]$ . The interaction of the along-channel with the across-channel vorticity,  $[\partial_y u]^{lc}$ , then yields vertical vorticity, or in other words lateral shear of the along-channel velocity,  $[\partial_y u]$ .<sup>20</sup> This lateral shear finally leads to a differential advection of the along-channel buoyancy gradient,  $\{\partial_x b\}$ , which leads to a lateral baroclinic pressure gradient,  $[\partial_y b]$ , which itself

<sup>18</sup>Note that according to equation (6.13) lateral circulation is the only source term for lateral shear in the model.

<sup>19</sup>The occurrence of the positive feedback loop at flood tide is associated with the positive along-channel buoyancy gradient,  $\{\partial_x b\}$ . For an opposed gradient, corresponding to an inverse estuary, we would find a similar loop at ebb-tide.

<sup>20</sup>In case of a vanishing along-channel gradient of the lateral velocity component,  $\partial_x v = 0$ , the vertical vorticity component corresponds to the lateral shear of the along-channel velocity,  $\omega_z = -\partial_y u$ .

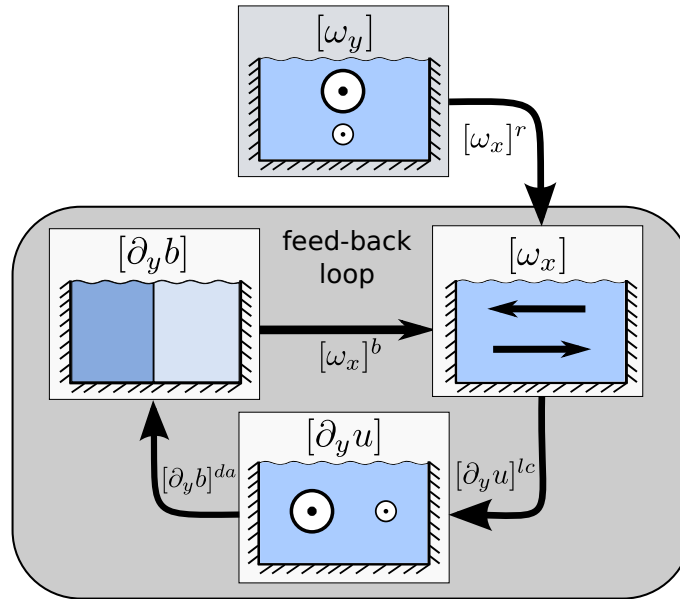


Figure 6.10.: Schematic of the positive feedback loop between lateral circulation and the across-channel buoyancy gradient at flood tide

now is able to support one of its origins, namely the stream-wise vorticity,  $[\omega_x]$ . Thus we find a self-amplifying system here during flood, that is able to generate strong lateral circulation and density stratification.

The reason for the sudden regime shift from longitudinal to lateral dynamics, might therefore originate in a critical threshold of the longitudinal buoyancy gradient and curvature forcing necessary to activate the feedback loop during flood, which then generates the substantial difference between the two regimes before and after  $Si_c$ .

The fact that the discontinuity occurs for the three different scenarios at different Simpson numbers clearly indicates a strong dependence of the critical Simpson-number on the radius of curvature. It is not straight-forward to explain, how this dependence looks like in detail and how  $Si_c$  is depending on other crucial parameters like for instance the channel width. Those questions remain unanswered in this study, but should be subject of future investigation, since a proper prediction of  $Si_c$  might deliver an important key in understanding the dynamics of many estuaries.

### Implication for residual estuarine circulation

As described above, the sudden phase transition does have substantial impact on the residual along-channel estuarine circulation. Its sudden increase at the discontinuity is mainly due to the increase of lateral transport of along-channel momentum at late flood, which is indicated by the strong increase in  $\langle[\omega_y]^{lc}\rangle_{T_p}$  (figure 6.9b). Before the discontinuity  $\langle[\omega_y]^{lc}\rangle_{T_p}$  is rather small, but afterwards it appears to be one of the most important, if not the most important driver for estuarine circulation.

The relative importance of  $[\omega_y]^{lc}$  increases with decreasing radius of curvature, thus we find  $\langle[\omega_y]^{lc}\rangle_{T_p}$  to be twice as large as  $\{\partial_x b\}$  for  $Si_{R2}$ , whereas we find approximately the

opposite ratio for Si\_R8, with  $\{\partial_x b\}$  being twice as large as  $\langle [\omega_y]^{lc} \rangle_{T_p}$ . However, comparing only the tidal mean of the along-channel buoyancy gradient and  $[\omega_y]^{lc}$ , might be misleading in terms of estimating their relative influence on estuarine circulation.

For well-mixed estuaries at full tidal currents vertical mixing is completely dominating over possible drivers for estuarine circulation, like the along-channel buoyancy gradient or lateral circulation. Thus a major fraction of residual estuarine circulation, which is basically an tidal asymmetry in the across-channel vorticity balance, will be generated around slack tides when tidal mixing is weak and therefore not able to instantaneously wipe out other effects.

In our model the along-channel buoyancy gradient  $\{\partial_x b\}$  is constant per definition, whereas  $[\omega_y]^{lc}$  is small most of the tidal cycle except around slack tide where it shows its maximum magnitudes. The fact that the periods close to slack tides might be especially crucial in terms of the generation of estuarine circulation, suggests that  $[\omega_y]^{lc}$  is a more important driver for estuarine exchange flow than  $\{\partial_x b\}$  in well-mixed estuaries, although their tidal averages are of comparable magnitudes.

The dramatic increase of the importance of lateral circulation in terms of the generation of along-channel exchange flow at the discontinuity, points to another aspect of the phase transition. Besides the transition between well-mixed and partially stratified conditions the jump can also be understood as a shift from a longitudinal tidal straining dominated regime to an regime where lateral transport does not only govern vertical stratification, but also residual estuarine circulation.

Burchard et al. (2011) calculated, based on a different idealized model, residual velocities for a comparable parameter range, but for a straight channel, thus neglecting the influence of curvature forcing. They found a continuous increase in  $M_{ec}$  corresponding in magnitude fairly nicely to our findings. This agreement is encouraging given the fact that their model was far more sophisticated, although they ignored channel curvature, but instead they introduced lateral dynamics due to a cross-channel varying water-depth.

### **Lateral Seiche at slack tide**

Besides the feedback loop at flood tide there seems to occur another interesting mechanism that might have a large dynamical influence. As mentioned earlier it is possible to observe a seiche-like (internal wave) phenomenon in the model output, for instance at setup US\_bx2. Especially during high-water slack tide, we find an oscillatory behavior of the lateral buoyancy gradient (solid green line figure 6.6b), and of the along-channel vorticity (green line figure 6.6a). A closer look at figure 6.6 indicates, that both curves ( $[\omega_x]^b$  and  $[\omega_x]$ ) are phase shifted by approximately  $\pi/2$  with respect to each other.

At slack tide, in the absence of along-channel tidal currents and thus turbulent mixing,

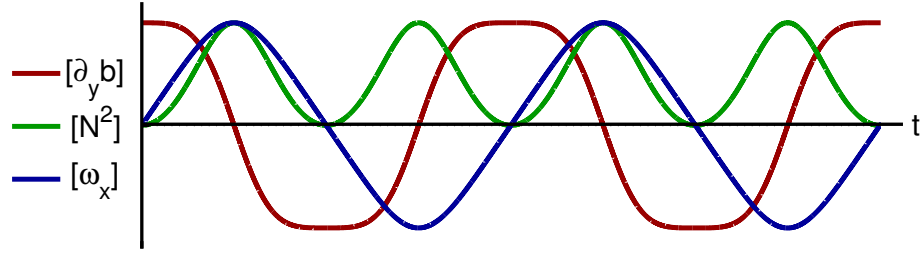


Figure 6.11.: Normalized solutions of the set of equations (6.29).

the set of model equations described in section 6.2 reduces to,

$$\begin{aligned}
 \partial_t[\omega_x] &\approx \overbrace{[\partial_y b]}^{[\omega_x]^b} \\
 \partial_t[N^2] &\approx \overbrace{[\partial_y b][\omega_x]}^{[N^2]^{Sy}} \\
 \partial_t[\partial_y b] &\approx -\overbrace{\frac{H^2}{B^2}[\omega_x][N^2]}^{[\partial_y b]^{N^2}} .
 \end{aligned} \tag{6.29}$$

The only remaining term responsible for a change in the along-channel vorticity is the lateral buoyancy gradient,  $[\partial_y b]$ , vertical stratification is just governed by lateral straining,  $[N^2]^{Sy}$ , and the lateral buoyancy gradient by the stratification term,  $[\partial_y b]^{N^2}$ . Thus we obtain a fairly simple set of differential equations, whose possible solutions are sketched in figure 6.11.

Starting with some initial value of  $[\partial_y b]$  and zero for  $[N^2]$  and  $[\omega_x]$ , respectively, the normalized solutions of (6.29) describe a characteristic oscillation. The lateral buoyancy gradient as well as the along-channel vorticity both follow a sin-like wave, where both are phase shifted by  $\pi/2$  towards each other (compare red and blue line figure 6.11). In contrast to  $[\omega_x]$  the curve for the lateral buoyancy gradient does not have a perfectly sinusoidal shape. The rather rapid transitions from positive to negative values and vice versa are followed by fairly long periods of maximum and minimum values, respectively.

$[N^2]$  also describes a sin-wave, but with a twice as large frequency than the two other curves. Furthermore,  $[N^2]$  does not become negative, but is oscillating around its average value. If we would start with some initial value of  $[N^2]$  we would find an oscillation on top of that initial value, thus  $[N^2]$  would not even become zero. Another interesting consequence of an initial  $[N^2]$  would be a large frequency of the oscillation.

The model simplification (6.29) is of course only valid as long as the along-channel tidal currents are small. Thus the seiche like phenomenon is only able to survive within a small time window around slack tides, embedded in the full dynamics of the entire tidal cycle that are most of the time dominated by bottom friction of the tidal currents. The turbulence coming along with the tidal currents is able to fully wipe out the seichal behavior for the largest fraction of the tidal cycle.

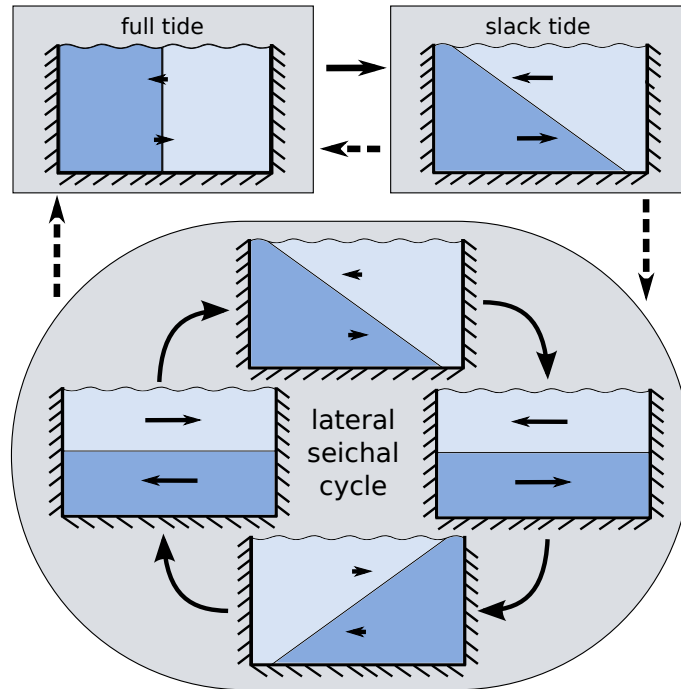


Figure 6.12.: Sketch of the lateral seichal cycle at slack tide.

Figure 6.12 shows a schematical diagram, how the lateral buoyancy gradient and lateral circulation do interact within a tidal cycle. During full tide (strong tidal currents) the production of  $[\partial_y b]$  is entirely dominated by differential advection,  $[\partial_y b]^{da}$ , which slowly builds up a lateral buoyancy gradient. As soon as tidal mixing becomes weaker close to slack tide, this lateral buoyancy gradient starts to generate vertical stratification via lateral straining. At this point the system enters the seichal cycle, where  $[\partial_y b]$  relaxes towards vertical stratification, via  $[\partial_y b]^{N^2}$ . The associated lateral circulation keeps on moving even when  $[\partial_y b]$  is already entirely transformed into  $[N^2]$ , but now it starts to generate an opposed lateral buoyancy gradient that itself begins to decelerate the lateral circulation. As soon as lateral circulation stops, the remaining lateral buoyancy gradient is able to drive now opposed lateral circulation, which re-transforms  $[\partial_y b]$  into  $[N^2]$  and so on.

This seichal cycle comes to an end when the tidal currents become stronger. The associated turbulence destroys the vertical stratification and thus wipes out the lateral seiche, at the same time  $[\partial_y b]^{da}$  again becomes the dominating term of the  $[\partial_y b]$ -balance.

The point at which the system leaves the seichal cycle, might be crucial in determining the consecutive tidal cycle, because even when turbulence is able to fully destroy vertical stratification and lateral circulation in the following strong current period there will still be a potentially different initial condition in terms of the lateral buoyancy gradient. Thus it might also have an impact on the sudden phase transition. Once the initial lateral buoyancy gradient short before low-water slack is strong enough to activate the seiche, such that it is able to perform half a cycle before the tidal currents kick in again, we have a situation, where the consecutive flood starts already with a  $[\partial_y b]$  that is in favor to drive

the feedback loop. Such a situation can be seen at setup US\_bx2 in figure 6.6.

## 6.6. Conclusions

In this study, we developed a simple zero-dimensional model in order to abstractly simulate lateral dynamics in estuaries and their impact on vertical stratification and residual along-channel estuarine circulation.

Despite the simplicity of the model and a rather coarse parameter tuning, it was possible to reproduce measurement data taken in a real curved tidal inlet (detail description in chapter 5), surprisingly well. With the help of the model it was possible to support the findings of chapter 5 that a major part of the dynamics in the tidal inlet of Spiekeroog is caused by a characteristic interplay of curvature forcing and horizontal buoyancy gradient yielding asymmetric lateral circulation, which finally controls vertical stratification and along-channel estuarine circulation.

Based on the model we showed that the results found for the rather special case of a  $S$ -shaped channel can be generalized to all kind of channel shapes. No matter if we have a  $S$ - or a  $U$ -shaped channel, there will be characteristic asymmetric lateral circulation, having substantial influence on vertical stratification and residual estuarine circulation. Just for very small along-channel buoyancy gradients,  $S$ -shaped channels seem to generate a stronger asymmetric lateral dynamics than  $U$ -shaped kinds.

The simple model allowed for a further exploration of the parameter space of well-mixed ( $Si = 0 \dots 0.14$ ) curved ( $R = 2, 4, 8$  km) estuaries. The results show a very interesting discontinuity associated with a sudden dynamical regime. Occurring at a particular critical Simpson number,  $Si_c$ , the discontinuity marks a phase transition from well-mixed along-channel tidal straining dominated dynamics towards laterally controlled partially stratified conditions, coming along with a substantial increase in residual estuarine circulation. Therefore, a further examination of this sudden regime shift might provide a whole new perspective on the difference between well-mixed and partially stratified estuaries as well as on their residual dynamics in general.

We were able to identify a positive feedback loop at flood tide, between lateral circulation and the across-channel buoyancy gradient that might be a key mechanism in understanding the sudden phase transition. The activation of the feedback loop at  $Si_c$ , yields a sudden self-amplification of asymmetric lateral circulation that entirely changes the dynamical state of the estuary.

Another possibly important mechanism in controlling the sudden regime shift might be a seiche-like phenomenon occurring at slack tide. Under certain circumstances this seiche is able to generate different initial conditions of the lateral buoyancy gradient for the consecutive full-current phase, and thus might play a crucial role in the sudden activation of the feedback loop.

The critical Simpson number does depend on the radius of curvature, since we found the discontinuity at larger Simpson numbers for a larger radius of curvature. However, we were not able to fully clarify how and on which parameters  $Si_c$  depends. Answer this question should be one of the major aims of future studies.

In general we can say, that the core of our model is a set of non-linear differential equation (6.8)–(6.13) that describe a deterministic chaos with potentially a number of

attractor points. Therefore it is not surprising that the model produces sudden jumps and discontinuities. An interesting question for future studies would be, if it is possible to find based on measurement data indications of such a chaotic behavior in real estuaries, or if this is rather a mathematical artefact due to the idealized system description.



## 7. Summary and Conclusions

In this thesis we investigated processes generating residual estuarine exchange flow and vertical stratification in well-mixed tidal inlets, with the help of two measurement campaigns carried out in the German Wadden Sea and an idealized model.

Based on the data of the first campaign it was possible to show for the first time direct evidence of tidal straining in the Wadden Sea, a process that is suspect to be responsible for a large fraction of estuarine circulation in this system and thus might provide an important source of sediment transport. Despite, these finding supporting the hypothesis of former studies that tidal straining might be a crucial mechanism in driving sediment transport from the open North Sea into the Wadden Sea, we also observed a strong lateral (across-channel) variability of vertical stratification yielding some first contradiction to this *classical* picture. While the data of a rather shallow measurement station at the southern site of the *Lister Deep* tidal inlet, do nicely fit to the expectations associated with tidal straining, of a well-mixed flood and a slightly more stratified ebb tide, observations from a deeper station located further north draw a different picture. Here, we find significant stratification occurring already at full flood, which puts a question mark over the theory of tidal straining as the most important driver of the estuarine dynamics in the inlet.

A second refined campaign at a different study site, in the tidal inlet between the islands of *Langeroog* and *Spiekeroog*, showed a similar phenomenology. At the southern slightly shallower part of the channel the observation agree fairly well with the theory of classical tidal straining. In contradiction to that, we found strong periodic late flood stratification at the northern slightly deeper part of the inlet. In contrast to the first campaign, the larger dataset of the second campaign allowed for the identification of the underlying mechanisms. The late flood stratification is found to be due to lateral circulation and the associated relaxation of an across-channel density gradient. By applying a consistent framework, associating longitudinal and lateral circulation to the across- and along-channel component of the vorticity, respectively, it was possible to show that the asymmetric lateral circulation, which is responsible for late flood stratification, is generated by a systematic interplay of centrifugal forcing and the horizontal density gradients. This newly discovered process, yielding strong lateral circulation during flood and significantly reduced lateral circulation during ebb, was further found to have substantial impact on the residual estuarine exchange flow, which we identified with the tidal mean of the across-channel vorticity component,  $\langle \omega_y \rangle_{M_2}$ .

Based on the same vorticity framework used to analyze the data, we developed a simple zero-dimensional numerical model, in order to test the general relevance of the systematic interplay of curvature and buoyancy forcing for other systems. Despite, the simplicity of the model, it was possible to nicely reproduce the data observed in the *Spiekeroog* tidal inlet, and thus to support the hypothesis that the systematic interplay of centrifugal

forcing and buoyancy gradients is primarily responsible for the occurrence of late flood stratification and even more importantly controls a major fraction of the residual estuarine exchange flow.

Furthermore, the model revealed that our findings for the special *S*-shaped channel of the *Spiekeroog* inlet can be generalized to all kind of channel shapes, emphasizing the relevance of our results for other weakly stratified curved tidal inlets. A further exploration of the parameter space of well-mixed systems, varying the Simpson number from zero to 0.14 for three different radii of curvature, 2, 4, and 8 km, provided a very surprising result. The model shows a sudden phase transition at a critical Simpson number,  $Si_c$ , from a well-mixed tidal straining dominated state to partially stratified lateral circulation dominated conditions. This phase transition happens rather fast<sup>1</sup> and does dramatically change the dynamical state of the system, yielding dominating flood tide stratification, asymmetric lateral circulation and a significantly larger residual estuarine exchange flow, which is mainly controlled by lateral redistribution of along-channel momentum. A possible explanation of the sudden phase transition is found in a seiche-like phenomenon occurring at slack tide, strongly effecting the initial lateral buoyancy gradient of the consecutive high current period. If the initial lateral buoyancy gradient of the flood phase has the right orientation it is able to drive a self-amplifying feedback loop yielding strong asymmetric lateral circulation. Thus  $Si_c$  might mark the critical threshold at which the lateral seiche at slack tide is in resonance with the self-amplifying feedback loop at flood tide. A better understanding of this critical threshold may provide a whole new perspective on the transitions from well-mixed to partial stratified estuaries.

Both systems analysed by the measurement campaigns do actually sit close to the critical Simpson number in parameter space, which leads to a possible explanation of the apparent contradiction in the data, where a well mixed tidal straining dominated shallow southern side of the channel contrasts a lateral circulation dominated norther part with substantial flood-tide stratification. A real system can never just be described by a single point in parameter space, but in fact it will always cover a particular range. Therefore, it might be that the shallow parts of the channel, which are stronger influenced by friction, are still part of a well-mixed tidal straining dominated regime, whereas the deeper parts of the inlet need to be already regarded as a laterally governed partially stratified system.

In conclusion we can say that although we have found a new process, which seems to be responsible for a major fraction of estuarine circulation and stratification in the studied inlet-systems, the dynamical interdependencies in real world estuaries are by far to complicated to be associated with just one particular mechanism.

---

<sup>1</sup>Fast in terms of  $Si$ -space

## 8. Future perspectives

There are many interesting questions and consequences that arise from our investigations, which could be or partly even need to be addressed by future studies.

One of those questions arises from our finding of the sudden dynamical regime shift, observed in our idealized model: Is the sudden phase transition a *real* physical phenomenon that can be observed in nature or at least in realistic three-dimensional simulation, or is it rather a numerical artefact, which is a consequence of the degree of abstraction of our idealized model?

A possible way to address this question from the measurement side is to study long-term observations, for instance of permanently anchored pole stations, measuring CTD and velocity data simultaneously. For the tidal inlets of the Wadden Sea there are a number of data from permanently anchored stations, which should be ideal to observe such sudden regime transition, since the predicted critical Simpson numbers do assumingly lie in the typical parameter range of those stations. If these dramatic transitions do exist in those system, they should appear for instance in the time record of  $N^2$ , where the average vertical stratification changes significantly from one tidal cycle to another, without a equally strong change in the external forcing conditions. But as we pointed out above, real systems correspond rather to a volume in parameter space than to a single point, which is why such a sudden transition might be rather smeared out in reality.

Another interesting phenomenon that appears in the model that could be further studied via measurements is the lateral seiche occurring at slack tide. Our transect measurements discussed in chapter 5 actually show some indications of such a seiche like-phenomenon. To study this phenomenon further one could think of a constellation of three or even more vertically resolving CTD-moorings distributed over a particular cross-section of a tidal inlet, to figure out if we can find the characteristic phase-relation of vertical and lateral stratification described in chapter 6.5.3.

A major motivation for this study was to identify possible mechanisms that are able to drive sediment transport into the Wadden Sea. Making reliable quantitative statements on, which process transports how much sediment in which tidal basin of the Wadden Sea, definitely requires realistic three dimensional modeling. However, our investigation showed that lateral processes control to a large extend the estuarine dynamics in the tidal inlets. Therefore, making realistic predictions of sediment transport into the Wadden Sea does require a proper horizontal and vertical resolution of the model in order to resolve the lateral dynamics of the tidal channels.

From a theoretical point of view it would definitely be interesting to further study the discontinuity, since it appears as some kind of switch, activating significant stratification and residual circulations within the system. A major question in this context is: How and on which parameters does the critical Simpson number depends on? We have already seen that the transition shifts towards larger Simpson numbers when we increase the radius

of curvature. It should be tested, if the discontinuity actually disappears as soon as we approach the limit of an infinite radius of curvature, which should be the case in order to be consistent with former idealized studies dealing with straight channels. But there are also other parameters on which  $Si_r$  might depend on, like for instance the lateral aspect ratio  $H/B$ , which seems to be a crucial parameter since it scales on the one hand the production of  $[\partial_y u]$  and on the other hand the destruction of  $[\partial_y b]$  (see (6.12) and (6.13)).

The model might also be used in order to study the relative importance of mixing asymmetries. The strong lateral circulation by the end of flood does generate residual estuarine exchange flow due to the lateral redistribution of along-channel momentum, but it also generates vertical stratification which may yield a significant mixing asymmetry. A mixing asymmetry associated with a stronger stratification during flood than ebb tide would rather oppose classical estuarine circulation (Stacey et al., 2008). Thus, there might exist a compensating interdependency of lateral momentum rectification and asymmetric tidal mixing that should be further investigated. To this end it seems necessary to substitute the rather simple Munk-Anderson parametrization by a more sophisticated turbulence model.

A feature of the model that was not extensively discussed in this thesis, since it did not effect the results, is its aperiodic behavior at particular areas of parameter space. Especially for larger radii of curvature we find that the model jumps from a single periodic to a higher periodic state, where the results do not repeat them selves each tidal cycle but every second third or even larger numbers of tidal cycles. This rather complex periodicities might be explained with the seiche-like phenomenon occurring at slack tide, that under certain circumstances is able to generate different initial conditions of the lateral buoyancy gradient for each tidal cycle.

In general we can say, that the model do consists of differential equations that show many characteristics of a deterministic chaos, thus it might be interesting to see if their are more attractor points to which the model might suddenly shift when reaching a particular position in parameter space.

# A. Vorticity-Model

## A.1. Basic relations

### A.1.1. Along-channel vorticity

The bulk along-channel vorticity is defined as

$$[\omega_x] = -\frac{2}{H} (v_s - v_b) , \quad (\text{A.1})$$

where here and after subscribed  $s$  and  $b$  denote the surface and bottom layer respectively. The rigid lid condition requires that,

$$\langle v \rangle_z = \frac{1}{2} (v_s + v_b) = 0 . \quad (\text{A.2})$$

From (A.1) and (A.2) follows that

$$v_s = -v_b , \quad (\text{A.3})$$

and thus

$$[\omega_x] = -\frac{4v_s}{H} = \frac{4v_b}{H} . \quad (\text{A.4})$$

### A.1.2. Across-channel vorticity

The bulk across-channel vorticity is defined as

$$[\omega_y] = \frac{2}{H} (u_s - u_b) . \quad (\text{A.5})$$

Furthermore the depth averaged along channel velocity, which is prescribed by the model as an external time dependent forcing parameter, is

$$\{u\} = \langle u \rangle_z = \frac{1}{2} (u_s + u_b) . \quad (\text{A.6})$$

Combining (A.5) and (A.6) yields

$$u_s = \{u\} + \frac{H}{4} [\omega_y] , \quad (\text{A.7})$$

and

$$u_b = \{u\} - \frac{H}{4} [\omega_y] . \quad (\text{A.8})$$

Note that the box-model is based on solving transport equations for gradients, but (A.4), (A.7), and (A.8) provide a direct link in order to calculate velocities from those gradients.

### A.1.3. Continuity equation

Due to the two-dimensionality of the model the continuity equation (2.3) reduces to,

$$\partial_y v = -\partial_z w . \quad (\text{A.9})$$

If we further take the rigid lid assumption into account, which demands that the volume flux from quadrant I to II must equal the flux from II to III (see Figure 6.1), we obtain

$$Q_{I,II}^V = Q_{II,III}^V \quad (\text{A.10})$$

$$\frac{1}{2} H v_s = -\frac{1}{2} B w_r ,$$

and analog

$$Q_{III,IV}^V = Q_{IV,I}^V \quad (\text{A.11})$$

$$-\frac{1}{2} H v_b = \frac{1}{2} B w_l ,$$

Combining (A.10) and (A.11) and making use of (A.3) and (A.4), yields

$$[\partial_y w] = \frac{2}{B} (w_r - w_l) = [\omega_x] \frac{H^2}{B^2} , \quad (\text{A.12})$$

where  $w_l$  and  $w_r$  denote the vertical velocity of the left- and the right-hand-side of the model domain, respectively (see figure 6.1).

## A.2. Derivation of model equations

### A.2.1. $[\omega_x]$

To derive a transport equation for the along-channel component of the vorticity we start with equation (2.2), and study its derivative with respect to  $z$  at the interface,  $z = -H/2$ ,

$$\begin{aligned} \partial_t (\partial_z v) \Big|_{-\frac{H}{2}} &= \left\{ -\partial_z u \partial_x v^0 - u \partial_z \partial_x v^0 - \partial_z v \partial_y v^0 - v \partial_z \partial_y v^0 \right. \\ &\quad - \partial_z w \partial_z v^0 - w \partial_z^2 v^0 - f \partial_z u + \frac{2}{R} \{u\} \partial_z u \\ &\quad \left. - g \partial_y \partial_z \eta^0 - [\partial_y b] - \partial_{zz}^2 \langle v'w' \rangle \right\}_{-\frac{H}{2}} , \end{aligned} \quad (\text{A.13})$$

where we made use of the assumptions (6.1)-(6.4).

The last term in equation (A.13) represents turbulent mixing and bottom friction, which we model with a two-layer approach,

$$\begin{aligned} \partial_{zz}^2 \langle v'w' \rangle \Big|_{-\frac{H}{2}} &= \frac{2}{H} \left( \frac{2}{H} \int_{-\frac{H}{2}}^0 \partial_z \langle v'w' \rangle dz - \frac{2}{H} \int_{-H}^{-\frac{H}{2}} \partial_z \langle v'w' \rangle dz \right) \\ &= \frac{4}{H^2} \left( -2 \langle v'w' \rangle \Big|_{-\frac{H}{2}} + \langle v'w' \rangle \Big|_{-H} \right) , \end{aligned} \quad (\text{A.14})$$

where we make use of the no surface flux condition (6.6). Inserting (A.14) in (A.13) and multiplying it by  $-1$ , finally yields (6.8), if we take  $[\omega_x] = -\partial_z v \Big|_{-\frac{H}{2}}$  into account.

### A.2.2. $[\omega_y]$

Similar to equation (A.13) we derive the transport equation of the across-channel component of the vorticity. Therefore we start with equation (2.1), study its derivative with respect to  $z$  at the interface,  $z = -H/2$ , and make use of the assumptions (6.1)-(6.4),

$$\begin{aligned} \partial_t(\partial_z u) \Big|_{-\frac{H}{2}} = & \left\{ -\partial_z u \overrightarrow{\partial_x u}^0 - u \overrightarrow{\partial_z \partial_x u}^0 - \partial_z v \partial_y u - \overrightarrow{v \partial_z \partial_y u}^0 \right. \\ & - \overrightarrow{\partial_z w \partial_z u}^0 - w \overrightarrow{\partial_{zz}^2 u}^0 + f \partial_z v - \frac{1}{R} \overrightarrow{v \partial_z u}^0 - \frac{1}{R} \{u\} \partial_z v \\ & \left. - g \overrightarrow{\partial_x \partial_z \eta}^0 - \{\partial_x b\} - \partial_{zz}^2 \langle u'w' \rangle \right\}_{-\frac{H}{2}}. \end{aligned} \quad (\text{A.15})$$

Analog to (A.14) we can write the friction term as,

$$\partial_{zz}^2 \langle u'w' \rangle \Big|_{-\frac{H}{2}} = -\frac{8}{H^2} \langle u'w' \rangle \Big|_{-\frac{H}{2}} + \frac{4}{H^2} \langle u'w' \rangle \Big|_{-H}, \quad (\text{A.16})$$

which yields (6.9), when we consider  $[\omega_y] = \partial_z u \Big|_{-\frac{H}{2}}$ .

### A.2.3. $[N^2]$

In order to derive the model equation for the vertical stratification (6.10), we use an analog procedure as for (A.13) and (A.15), starting from the transport equation of the buoyancy (2.5), we study its vertical derivation at  $z = -H/2$ ,

$$\begin{aligned} \partial_t(\partial_z b) \Big|_{-\frac{H}{2}} = & \left\{ -\partial_z u \{\partial_x b\} - u \overrightarrow{\partial_z \partial_x b}^0 - \partial_z v \partial_y b - \overrightarrow{v \partial_z \partial_y b}^0 \right. \\ & \left. - \overrightarrow{\partial_z w \partial_z b}^0 - w \overrightarrow{\partial_{zz}^2 b}^0 - \partial_{zz}^2 \langle w'b' \rangle \right\}_{-\frac{H}{2}}, \end{aligned} \quad (\text{A.17})$$

where we again made use of the assumption (6.1)-(6.4).

Applying a similar procedure as for (A.14), the turbulent flux term becomes,

$$\partial_{zz}^2 \langle w'b' \rangle \Big|_{-\frac{H}{2}} = -\frac{8}{H^2} \langle w'b' \rangle \Big|_{-\frac{H}{2}}, \quad (\text{A.18})$$

where we made use of the fact that the buoyancy flux at the surface and at the bottom vanishes. Finally considering,  $[N^2] = \partial_z b \Big|_{-\frac{H}{2}}$  yields (6.10).

### A.2.4. $[\partial_y b]$

To derive a transport equation for the lateral buoyancy gradient we take the  $y$ -derivative of the depth-mean of (2.5) and evaluate it at  $y = B/2$

$$\begin{aligned} \partial_t(\langle \partial_y b \rangle_z) \Big|_{y=\frac{B}{2}} = & \left\{ -\langle \partial_y u \rangle_z \{\partial_x b\} - \{u\} \overrightarrow{\partial_x (\partial_y b)}^0 - \overrightarrow{\partial_y (v)_z \partial_y b}^0 - \langle v \rangle_z \overrightarrow{\partial_{yy}^2 b}^0 \right. \\ & \left. - \langle \partial_y w \rangle_z \partial_z b - \langle w \overrightarrow{\partial_z (\partial_y b)} \rangle_z^0 - \partial_y \langle \partial_z \langle w'b' \rangle \rangle_z \right\}_{y=\frac{B}{2}}, \end{aligned} \quad (\text{A.19})$$

where we made use of the assumption (6.1)–(6.4). If we further consider (A.12) and

$$\partial_y \langle \partial_z \langle w'b' \rangle \rangle_z = \partial_y \frac{1}{H} \langle w'b' \rangle \Big|_{-H}^0 = 0 , \quad (\text{A.20})$$

(A.19) becomes

$$\partial_t [\partial_y b] = -[\partial_y u] \{ \partial_x b \} - \frac{H^2}{B^2} [\omega_x] [N^2] , \quad (\text{A.21})$$

which corresponds to the model equation (6.12).

### A.2.5. $[\partial_y u]$

In order to derive the transport equation for the lateral shear, we start with equation (2.1) and proceed similar as for  $[\partial_y b]$ ,

$$\begin{aligned} \partial_t (\langle \partial_y u \rangle_z) \Big|_{y=\frac{B}{2}} &= \left\{ -\cancel{\partial_y \langle u \partial_x u \rangle_z} \Big|_{y=\frac{B}{2}}^0 - \cancel{\partial_y \langle v \partial_y u \rangle_z} \Big|_{y=\frac{B}{2}}^0 - \partial_y \langle w \partial_z u \rangle_z + f \cancel{\partial_y \langle v \rangle_z} \Big|_{y=\frac{B}{2}}^0 \right. \\ &\quad \left. - \frac{1}{R} \left[ \cancel{\langle v \partial_y u \rangle_z} \Big|_{y=\frac{B}{2}}^0 + \cancel{\langle u \partial_y v \rangle_z} \Big|_{y=\frac{B}{2}}^0 \right] - \{ \partial_x b \} \cancel{\partial_y \langle \int_{-H}^0 dz \rangle_z} + \partial_y \langle \partial_z \langle u'w' \rangle \rangle_z \Big|_{y=\frac{B}{2}} \right\} . \end{aligned} \quad (\text{A.22})$$

After applying the assumption (6.1)–(6.4), there are tow terms left that need to be taken into account, the vertical advection term, which, considering (A.12), becomes

$$\begin{aligned} \langle \partial_y (w \partial_z u) \rangle_z \Big|_{y=B/2} &\approx \partial_y (\langle w \rangle_z [\omega_y]) \Big|_{y=B/2} \\ &= \left( \cancel{\langle w \rangle_z} \Big|_{y=B/2}^0 \partial_y [\omega_y] \right) \Big|_{y=B/2} + ([\omega_y] \partial_y \langle w \rangle_z) \Big|_{y=B/2} \\ &= \frac{H^2}{B^2} [\omega_x] [\omega_y] , \end{aligned} \quad (\text{A.23})$$



and the friction term, which can be approximated by

$$\begin{aligned}
-\partial_y \langle \langle u'w' \rangle \rangle_z &= \frac{1}{H} \partial_y \langle u'w' \rangle \Big|_{-H} \\
&= -\frac{1}{H} \partial_y (u_*^x u_*) \\
&= -\frac{1}{H} (u_* \partial_y u_*^x + u_*^x \partial_y u_*) \\
&\approx -\frac{1}{H} \left( u_* \partial_y u_*^x + \frac{(u_*^x)^2}{u_*} \partial_y u_*^x \right) \\
&= -\frac{1}{H} u_* \partial_y u_*^x \left( 1 + \frac{(u_*^x)^2}{(u_*)^2} \right) \\
&\approx -\frac{2}{H} u_* \partial_y u_*^x \tag{A.24} \\
&= -\frac{2\sqrt{C_d}}{H} u_* \partial_y \langle u \rangle_{BL} \\
&= -\frac{2\sqrt{C_d}}{H} u_* \partial_y \left( \langle u \rangle_z - \frac{H}{4} [\omega_y] \right) \\
&\approx -\frac{2\sqrt{C_d}}{H} u_* \partial_y \left( \langle u \rangle_z - \frac{H}{4} \frac{2u_*^x}{\kappa H} \right) \\
&= -\frac{2\sqrt{C_d}}{H} u_* \partial_y \left( \langle u \rangle_z - \frac{\sqrt{C_d}}{2\kappa} \left( \langle u \rangle_z - \frac{\sqrt{C_d}}{2\kappa} (\dots) \right) \right) \\
&\approx -\frac{2\sqrt{C_d}}{H} u_* [\partial_y u] ,
\end{aligned}$$

where we made use of the scaling (5.25). Thus the model equation for the lateral shear may look like,

$$\partial_t [\partial_y u] = -\frac{H^2}{B^2} [\omega_x] [\omega_y] - \frac{2\sqrt{C_d}}{H} u_* [\partial_y u] . \tag{A.25}$$

### A.3. $[\Phi]$

The potential energy anomaly is defined as

$$\Phi = \frac{g}{H} \int_{-H}^0 (\langle \rho \rangle_z - \rho) z dz' , \tag{A.26}$$

with  $z'$  being a integration variable. In a two layer fluid this can be rewritten as,

$$\begin{aligned}
[\Phi] &= \frac{g}{H} \left[ \int_{-\frac{H}{2}}^0 \left( \frac{\rho_s + \rho_b}{2} - \rho_s \right) z dz' + \int_{-H}^{-\frac{H}{2}} \left( \frac{\rho_s + \rho_b}{2} - \rho_b \right) z dz' \right] \\
&\quad \frac{g}{H} \frac{\rho_s - \rho_b}{2} \left[ - \int_{-\frac{H}{2}}^0 z dz' + \int_{-H}^{-\frac{H}{2}} z dz' \right] \\
&\quad \frac{g}{8} [\partial_z \rho] \left[ -z^2 \Big|_{-\frac{H}{2}}^0 + z^2 \Big|_{-H}^{-\frac{H}{2}} \right] \\
&\quad - \frac{gH^2}{16} [\partial_z \rho] .
\end{aligned} \tag{A.27}$$

If we further consider

$$[N^2] = - \frac{g}{\rho_0} [\partial_z \rho] , \tag{A.28}$$

we obtain

$$[\Phi] = \frac{\rho_0 H^2}{16} [N^2] . \tag{A.29}$$

## A.4. Turbulence closure

For well mixed flows it is common to use a parabolic profile for the turbulent viscosity (see e.g. Burchard and Hofmeister (2008)),

$$\nu_t^p = u_* \kappa \frac{-z}{H} (z + H) . \tag{A.30}$$

As a value for the viscosity at the interface between surface and bottom layer we use,

$$\nu_0 = \nu_t^p \Big|_{-\frac{1}{2}H} = u_* \kappa \frac{H}{4} . \tag{A.31}$$

In order to take the limiting effect of stratification into account we use the Munk and Anderson (1948) parameterization,

$$[\nu_t] = \nu_0 (1 + 10[\text{Ri}_g])^{-\frac{1}{2}} , \tag{A.32}$$

for the turbulent viscosity at the interface, and

$$[\nu_t^b] = \nu_0 \left( 1 + \frac{10}{3} [\text{Ri}_g \text{Ri}_g \text{Ri}_g \text{Ri}_g]^{-\frac{3}{2}} \right) , \tag{A.33}$$

for the turbulent diffusivity of bouyancy. (A.32) and (A.33) correspond to (6.20) and (6.21).

## A.5. Periodicity of a signal

In order to perform a proper time averaging, where the results are independent of the starting point of the average window, it is necessary to find a decent window length.

This window length should match the periodicity,  $P$ , of the time series produced by the model. In most cases the periodic time interval,  $T_P$ , corresponds to one tidal cycle, but the periodicity of some model runs is larger, meaning that they are periodic with respect to two, three or even larger numbers of tidal cycles.

To determine the window-length or periodicity, we pick a representative time series. Here we use  $N^2$ , but it would also be possible to choose any other indicator. The output time series of  $N^2$ , which we choose to be 20 cycles long, is divided into individual tidal cycles. Thus we obtain 20 one period long time serieses.

Those 20 cycles are then correlated to each other, which gives a 20 by 20 correlation matrix. This matrix is now duplicated and added to itself, which provides a 40 by 20 matrix,  $C_{i,j}$ . This matrix has now 20 diagonals, each 20 elements long. The first diagonal contains the elements,  $C_{i,i}$ , which are one per definition, simply indicating that each tidal cycle is perfectly correlated to itself. The second diagonal contains the elements,  $C_{i,i+1}$ , that are only one if the original signal is perfectly period with respect to each cycle.

Finding the periodicity,  $P$ , of a signal corresponds now to the task of finding the right diagonal, whos elements are close enough to one. The minimum requirement for a diagonal to be taken into account is that all its values are larger than 0.9, corresponding to a correlation of at least 90% for each cycle. Then we take the trace of those diagonals that are left,  $Tr\{C_{i,i+P}\}$ , and pick the  $P$  whos diagonal has the largest trace as the periodicity of the signal. In case of several diagonals having the same trace, we pick the one with the smallest  $P$ . As a last quality filter, we require that the average of the diagonal elements,  $\langle C_{i,i+P} \rangle$ , have to be at least 0.95 corresponding to a minimum overall correlation of 95%. In the case that one of the requirments is not full filled, we say that the signal is not periodic.



# Bibliography

- Alaee, M. J., G. Ivey, and C. Pattiaratchi, 2004: Secondary circulation induced by flow curvature and coriolis effects around headlands and islands. *Ocean Dynamics*, **54**, 27–38.
- Aubrey, D. and P. Speer, 1985: A study of non-linear tidal propagation in shallow inlet/estuarine systems Part I: Observations. *Estuarine, Coastal and Shelf Science*, **21**, 185–205.
- Becherer, J., H. Burchard, G. Flöser, V. Mohrholz, and L. Umlauf, 2011: Evidence of tidal straining in well-mixed channel flow from micro-structure observations. *Geophys. Res. Lett.*, **38**.
- Becherer, J., M. T. Stacey, L. Umlauf, and H. Burchard, submitted: Asymmetric lateral circulation in a well-mixed tidal inlet: Mechanisms and implications. *J. Phys. Oceanogr.*.
- Becherer, J. and L. Umlauf, 2011: Boundary mixing in lakes. 1. Modeling the effect of shear-induced convection. *J. Geophys. Res.*, **116**, C10017.
- Boon, J. D. and R. J. Byrne, 1981: On basin hypsometry and the morphodynamic response of coastal inlet systems. *Marine Geology*, **40**, 27–48.
- Buijsman, M. and H. Ridderinkhof, 2008: Variability of secondary currents in a weakly stratified tidal inlet with low curvature. *Cont. Shelf Res.*, **28**, 1711–1723.
- Burchard, H., 2009: Combined effects of wind, tide and horizontal density gradients on stratification in estuaries and coastal seas. *J. Phys. Oceanogr.*, **39**, 2117–2136.
- Burchard, H. and H. Baumert, 1998: The formation of estuarine turbidity maxima due to density effects in the salt wedge. A hydrodynamic process study. *J. Phys. Oceanogr.*, **28**, 309–321.
- Burchard, H., G. Flöser, J. V. Staneva, R. Riethmüller, and T. Badewien, 2008: Impact of density gradients on net sediment transport into the Wadden Sea. *J. Phys. Oceanogr.*, **38**, 566–587.
- Burchard, H., R. Hetland, E. Schulz, and H. Schuttelaars, 2011: Drivers of residual estuarine circulation in tidally energetic estuaries: Straight and irrotational channels with parabolic cross section. *J. Phys. Oceanogr.*, **41**, 548–570.
- Burchard, H. and R. D. Hetland, 2010: Quantifying the contributions of tidal straining and gravitational circulation to residual circulation in periodically stratified tidal estuaries. *J. Phys. Oceanogr.*, **40**, 1243–1262.

- Burchard, H. and R. Hofmeister, 2008: A dynamic equation for the potential energy anomaly for analysing mixing and stratification in estuaries and coastal seas. *Estuarine, Coastal and Shelf Science*, **77**, 679–687.
- Burchard, H. and H. M. Schuttelaars, 2012: Analysis of tidal straining as driver for estuarine circulation in well-mixed estuaries. *J. Phys. Oceanogr.*, **42**, 261–271.
- Chant, R. J., 2002: Secondary circulation in a region of flow curvature: Relationship with tidal forcing and river discharge. *J. Geophys. Res.*, **107**, 3131.
- Chant, R. J. and R. E. Wilson, 1997: Secondary circulation in a highly stratified estuary. *J. Geophys. Res.*, **102**, 23207–23.
- Cheng, P., R. E. Wilson, R. J. Chant, D. C. Fugate, and R. D. Flood, 2009: Modeling influence of stratification on lateral circulation in a stratified estuary. *J. Phys. Oceanogr.*, **39**, 2324–2337.
- Collignon, A. and M. Stacey, 2012: Intratidal dynamics of fronts and lateral circulation at the shoal-channel interface in a partially stratified estuary. *J. Phys. Oceanogr.*, **42**, 869–883.
- De Boer, G. J., J. D. Pietrzak, and J. C. Winterwerp, 2008: Using the potential energy anomaly equation to investigate tidal straining and advection of stratification in a region of freshwater influence. *Ocean Modelling*, **22**, 1–11.
- Dillon, T. M., 1982: Vertical overturns: A comparison of Thorpe and Ozmidov length scales. *J. Geophys. Res.*, **87**, 9601–9613.
- Dronkers, J., 1996: The influence of buoyancy on transverse circulation and on estuarine dynamics. *Buoyancy Effects on Coastal and Estuarine Dynamics*, 341–356.
- Dyer, K., 1989: Estuarine flow interaction with topography lateral and longitudinal effects. *Estuarine Circulation*, Springer, 39–59.
- Fer, I., 2006: Scaling turbulent dissipation in an Arctic fjord. *Deep-Sea Res. II*, **53**, 77–95.
- Fischer, H., 1972: Mass transport mechanisms in partially stratified estuaries. *J. Fluid Mech.*, **53**, 671–687.
- Flöser, G., H. Burchard, and R. Riethmüller, 2011: Observational evidence for estuarine circulation in the German Wadden Sea. *Cont. Shelf Res.*, **31**, 1633–1639.
- Friedrichs, C. T. and D. G. Aubrey, 1988: Non-linear tidal distortion in shallow well-mixed estuaries: a synthesis. *Estuarine, Coastal and Shelf Science*, **27**, 521–545.
- Geyer, W. R., 1993: Three-dimensional tidal flow around headlands. *J. Geophys. Res.*, **98**, 955–966.
- Geyer, W. R. and P. MacCready, 2013: The estuarine circulation. *Annual Review of Marine Science*, doi:10.1146/annurev-fluid-010313-141302.

- Geyer, W. R., J. H. Trowbridge, and M. M. Bowen, 2000: The dynamics of a partially mixed estuary. *J. Phys. Oceanogr.*, **30**, 2035–2048.
- Hansen, D. V. and M. Rattray, 1965: Gravitational circulation in straits and estuaries. *J. Mar. Res.*, **23**, 104–122.
- Hofmeister, R., H. Burchard, and K. Bolding, 2009: A three-dimensional model study on processes of stratification and de-stratification in the Limfjord. *Cont. Shelf Res.*, **29**, 1515–1524.
- Huijts, K., H. Schuttelaars, H. De Swart, and C. Friedrichs, 2009: Analytical study of the transverse distribution of along-channel and transverse residual flows in tidal estuaries. *Cont. Shelf Res.*, **29**, 89–100.
- Jay, D. and J. Musiak, 1994: Particle trapping in estuarine tidal flows. *J. Geophys. Res.*, **99**, 20445–20461.
- 1996: Internal tidal asymmetry in channel flows: Origins and consequences. *Mixing in estuaries and coastal seas*, 211–249.
- Kalkwijk, J. P. T. and R. Booij, 1986: Adaptation of secondary flow in nearly-horizontal flow. *Journal of Hydraulic Research*, **24**, 19–37.
- Kim, Y. H. and G. Voulgaris, 2008: Lateral circulation and suspended sediment transport in a curved estuarine channel: Winyah Bay, SC, USA. *J. Geophys. Res.*, **113**.
- Lacy, J., M. Stacey, J. Burau, and S. Monismith, 2003: Interaction of lateral baroclinic forcing and turbulence in an estuary. *J. Geophys. Res.*, **108**, 3089.
- Lacy, J. R. and S. G. Monismith, 2001: Secondary currents in a curved, stratified, estuarine channel. *J. Geophys. Res.*, **106**, 31283–31302.
- Lerczak, J. and W. Geyer, 2004: Modeling the lateral circulation in straight, stratified estuaries. *J. Phys. Oceanogr.*, **34**, 1410–1428.
- Lorrai, C., L. Umlauf, J. Becherer, A. Lorke, and A. Wüest, 2011: Boundary mixing in lakes. 2. Combined effects of shear-induced and convective turbulence on basin-scale mixing. *J. Geophys. Res.*, **116**, C10018.
- MacCready, P. and W. R. Geyer, 2010: Advances in estuarine physics. *Annu. Rev. Marine. Sci.*, **2**, 35–58.
- Moum, J. N., M. C. Gregg, R.-C. Lien, and M. E. Carr, 1995: Comparison of turbulent kinetic energy dissipation rate estimates from two ocean microstructure profilers. *J. Atmos. Ocean. Tech.*, **12**, 346–366.
- Munk, W. H. and E. R. Anderson, 1948: Notes on the theory of the thermocline. *J. Mar. Res.*, **3**, 276–295.
- Nidziko, N. J., J. L. Hench, and S. G. Monismith, 2009: Lateral circulation in well-mixed and stratified estuarine flows with curvature. *J. Phys. Oceanogr.*, **39**, 831–851.

- Nunes, R. and J. Simpson, 1985: Axial convergence in a well-mixed estuary. *Estuarine, Coastal and Shelf Science*, **20**, 637–649.
- Pritchard, D. W., 1952: Salinity distribution and circulation in the Chesapeake Bay estuarine system. *J. Mar. Res.*, **11**, 106–123.
- 1954: A study of the salt balance in a coastal plain estuary. *J. Mar. Res.*, **13**, 133–144.
- 1956: The dynamic structure of a coastal plain estuary. *J. Mar. Res.*, **15**, 33–42.
- Rippeth, T. P., N. Fisher, and J. H. Simpson, 2001: The semi-diurnal cycle of turbulent dissipation in the presence of tidal straining. *J. Phys. Oceanogr.*, **31**, 2458–2471.
- Scully, M. and W. Geyer, 2012: The role of advection, straining and mixing on the tidal variability of estuarine stratification. *J. Phys. Oceanogr.*, **42**, 855–868.
- Scully, M. E., W. R. Geyer, and J. A. Lerczak, 2009: The influence of lateral advection on the residual estuarine circulation: A numerical modeling study of the Hudson River estuary. *J. Phys. Oceanogr.*, **39**, 107–124.
- Scully, M. E., W. R. Geyer, and J. H. Trowbridge, 2011: The influence of stratification and nonlocal turbulent production on estuarine turbulence: An assessment of turbulence closure with field observations. *J. Phys. Oceanogr.*, **41**, 166–185.
- Seim, H. E. and M. C. Gregg, 1997: The importance of aspiration and channel curvature in producing strong vertical mixing over a sill. *J. Geophys. Res.*, **102**, 3451–3472.
- Sharples, J. and J. H. Simpson, 1995: Semi-diurnal and longer period stability cycles in the Liverpool Bay region of freshwater influence. *Cont. Shelf Res.*, **15**, 295–313.
- Simpson, J., 1981: The Shelf-Sea Fronts: Implications of their Existence and Behaviour. *Royal Society of London Philosophical Transactions Series A*, **302**, 531–543.
- Simpson, J. and J. Hunter, 1974: Fronts in the Irish Sea. *Nature*, **250**, 404–406.
- Simpson, J. H., J. Brown, J. Matthews, and G. Allen, 1990: Tidal straining, density currents, and stirring in the control of estuarine stratification. *Estuaries and Coasts*, **13**, 125–132.
- Simpson, J. H., H. Burchard, N. R. Fisher, and T. P. Rippeth, 2002: The semi-diurnal cycle of dissipation in a ROFI: model-measurement comparisons. *Cont. Shelf Res.*, **22**, 1615–1628.
- Simpson, J. H., E. Williams, L. H. Brasseur, and J. M. Brubaker, 2005: The impact of tidal straining on the cycle of turbulence in a partially stratified estuary. *Cont. Shelf Res.*, **25**, 51–64.
- Speer, P. and D. Aubrey, 1985: A study of non-linear tidal propagation in shallow inlet/estuarine systems part ii: Theory. *Estuarine, Coastal and Shelf Science*, **21**, 207–224.



- 
- Stacey, M. T., 1996: *Turbulent mixing and residual circulation in a partially stratified estuary*. Ph.D. thesis, Stanford University.
- Stacey, M. T., J. R. Burau, and S. G. Monismith, 2001: Creation of residual flows in a partially stratified estuary. *J. Geophys. Res.*, **106**, 17013–17037.
- Stacey, M. T., J. P. Fram, and F. K. Chow, 2008: Role of tidally periodic density stratification in the creation of estuarine subtidal circulation. *J. Geophys. Res.*, **113**, C08016.
- Stanev, E., G. Flöser, and J. Wolff, 2003: First-and higher-order dynamical controls on water exchanges between tidal basins and the open ocean. A case study for the East Frisian Wadden Sea. *Ocean Dynamics*, **53**, 146–165.
- Umlauf, L. and H. Burchard, 2003: A generic length-scale equation for geophysical turbulence models. *Journal of Marine Research*, **61**, 235–265.
- 2005: Second-order turbulence closure models for geophysical boundary layers. A review of recent work. *Cont. Shelf Res.*, **25**, 795–827.
- Valle-Levinson, A., W. Boicourt, and M. Roman, 2003: On the linkages among density, flow, and bathymetry gradients at the entrance to the Chesapeake Bay. *Estuaries and Coasts*, **26**, 1437–1449.
- Valle-Levinson, A., K.-C. Wong, and K. Lwiza, 2000: Fortnightly variability in the transverse dynamics of a coastal plain estuary. *J. Geophys. Res.*, **105**, 3413–3424.
- van Aken, H. M., 1986: The onset of stratification in shelf seas due to differential advection in the presence of a salinity gradient. *Cont. Shelf Res.*, **5**, 475–485.
- van der Lee, E. M. and L. Umlauf, 2011: Internal-wave mixing in the Baltic Sea: Near-inertial waves in the absence of tides. *J. Geophys. Res.*, **116**, C10016.
- Verspecht, F. I., H. Burchard, T. P. Rippeth, M. J. Howarth, and J. H. Simpson, 2009: Processes impacting on stratification in a region of freshwater influence: Application to Liverpool Bay. *J. Geophys. Res.*, **114**, 11022.
- Waterhouse, A. F. and A. Valle-Levinson, 2010: Transverse structure of subtidal flow in a weakly stratified subtropical tidal inlet. *Cont. Shelf Res.*, **30**, 281–292.



# Eidesstattliche Versicherung

Hiermit versichere ich an Eides statt, dass ich die vorliegende Arbeit selbständig und ohne Benutzung anderer als der angegebenen Hilfsmittel angefertigt habe. Die aus anderen Quellen oder indirekt übernommenen Daten und Konzepte sind unter Angabe der Quelle gekennzeichnet. Die Arbeit wurde bisher weder im In- noch im Ausland in gleicher oder ähnlicher Form in einem Verfahren zur Erlangung eines akademischen Grades vorgelegt.

---

Ort, Datum

Johannes Becherer